

ABSTRACT

Title of dissertation: INVESTIGATION OF COUPLED
ROTOR-DRIVETRAIN-AIRFRAME-ENGINE
VIBRATIONS USING DYNAMIC
SUBSTRUCTURING

Stacy Sidle, Doctor of Philosophy, 2020

Dissertation directed by: Professor Inderjit Chopra
Department of Aerospace Engineering

Excessive vibrations continue to be a problem that rotorcraft designers are unable to address until flight testing. Accurate prediction of vibrations throughout the aircraft is hindered by the complexity of the models required. This dissertation focuses on utilizing frequency based modeling and substructuring methods to enable full coupling between the comprehensive analysis modeling of the rotor aeromechanics and finite element models of the drivetrain, airframe, and engines.

A substructuring methodology is developed to analyze the coupled structural dynamic response of an elastic airframe and engines of a helicopter in response to main rotor and tail rotor hub loads. Transfer functions of individual components (airframe, engine, mount struts and torque tube) are coupled together using a sub-structuring approach to obtain consistent coupled solutions of the entire system. Using this approach, a twin-engine, four-bladed helicopter is analyzed using NASTRAN-based models of the airframe and engines. This ultra-efficient substructuring approach is validated against the fully coupled NASTRAN model using forced

response studies. Characteristics of the mount properties, i.e., the torque tube stiffness, and aft mount stiffness and damping are systematically varied to study their effect on the engine vibration response. The fore and aft mount element properties for minimizing the 8P engine response are identified without increasing 4P response. A compromise between 4P and 8P response is also identified from parametric studies of rear mount properties, using just 3 parameters to represent the design space. Using the sub-structuring approach presented here, future studies can be performed to rapidly match airframe characteristics with available engines at approximately 1000 times the speed of running a detailed finite element model (millions of degrees of freedom), without any reduction in accuracy.

Comprehensive vibration analysis of a rotor-airframe-engine-drivetrain system using a time-domain modal coupling approach was conducted. Pair-wise couplings of components were performed to isolate the contribution of each component to the complete coupled system, and the effect of each component (airframe and drivetrain/engine) on rotor loads and hub loads was studied. The drivetrain model was a 6-dof model consisting of inertia and torsional spring elements, while the airframe model used was a NASTRAN superelement of a detailed finite element airframe model. Although drivetrain coupling resulted in elastic twist of the shaft by less than 0.02 degrees, there were noticeable reductions in the 4/rev chordwise blade bending moments as well the 4/rev vertical hub force. The airframe coupling produced very small hub motions, less than 1×10^{-4} inches, and showed almost identical trends in both the blade loads and hub loads. 8/rev hub forces and moments were significantly affected by both the airframe and drivetrain coupling.

INVESTIGATION OF COUPLED
ROTOR-DRIVETRAIN-AIRFRAME-ENGINE
VIBRATIONS USING DYNAMIC
SUBSTRUCTURING

by

Stacy Marie Sidle

Dissertation submitted to the Faculty of the Graduate School of the
University of Maryland, College Park in partial fulfillment
of the requirements for the degree of
Doctor of Philosophy
2020

Advisory Committee:
Professor Inderjit Chopra, Chair/Advisor
Professor Anubhav Datta
Professor Olivier Bauchau
Professor James Baeder
Professor Amr Baz

© Copyright by
Stacy Marie Sidle
2020

Dedication

This work is dedicated to my dad, William Malcolm Sidle IV. I never got to talk helicopters with him, but I have felt his influence in everything I've done in this field.

This work is also dedicated to my new son, Malcolm. His arrival definitely threw a wrench in things, but I am proud that I can serve as an example to him of perseverance and finishing what you start.

Acknowledgments

Although every word of this dissertation was typed by me, there are countless people who have made this work possible. I have benefitted greatly from several mentors, not the least of whom is Dr. Inder Chopra, my thesis advisor. I know I was not always an easy student to advise, and a lesser advisor might have given up on me, but Dr. Chopra was persistent in encouraging me to finish, even when obstacles and distractions kept cropping up. VT Nagaraj has also been someone whom I could always count on to encourage me. Finally, Dr. Ananth Sridharan always impressed and baffled me with his brilliant mind. Although at times frustrating to work with, he was always there to answer questions and definitely made my work better.

As a highly social person, I make friends wherever I go, and the University of Maryland has been no exception. From those who were here when I started and showed me the ropes from day one — I continue to be grateful for the friendship and of Joe Schmaus, Elizabeth Ward, Will Staruk, Ben Berry, and Graham Bowen-Davies. I'm also grateful for the my contemporaries and the newer crop of students who allowed me to occasionally impart wisdom and (more often) interrupt their own productivity when I needed to slack off. A non-exhaustive list of those people includes: Field Manar, Andrew Lind, Peter Mancini, Andre Bauknecht, Tom Pillsbury, Steve Sherman, Caitlin King, James Lankford, Dave Mayo, Fred Tsai, Brandy Phillips, Ravi Lumba, Emily Fesler, Seyhan Gul, Dan Escobar, Tyler Sinotte, Bharath Govindarajan, Vera Klimchenko, Thomas Herrmann, Ali LeMoine, and plenty of others. Looking back, the number of people I have included here is prob-

ably one of the reasons it has taken me so long to finish, but I really wouldn't have it any other way. I truly hope our paths will cross again, but if they don't, know that you have made an impression in my life.

Finally, and most importantly, I'd like to thank my husband, Alex. We were not married when I applied and was accepted to the program, but he did not hesitate in telling me to accept the offer, even though it meant moving away from our beloved Austin, TX. I'm so grateful to have had him with me on this journey, and I truly could not have done it without him.

Table of Contents

List of Figures	viii
List of Tables	xii
Abbreviations	xiii
1 Introduction	1
1.1 Background	2
1.2 Motivation	3
1.3 Literature Review	6
1.3.1 Rotor Vibratory Loads	7
1.3.2 Airframe Structural Dynamics Modeling	8
1.3.3 Rotor-Airframe Coupling	11
1.3.4 Drivetrain and Engine Studies	16
1.3.4.1 Rotor-Drivetrain Coupling	16
1.3.4.2 Engine-Airframe Coupling	18
1.3.5 Substructuring Methods	19
1.3.5.1 Component mode synthesis	22
1.3.5.2 Frequency-based substructuring	25
1.4 Scope of Current Work	27
1.4.1 Overview of Dissertation	28
2 Methodology	33
2.1 Comprehensive Analysis: PRASADUM	33
2.1.1 Overview of Solution Method	34
2.1.2 Coordinate Systems	35
2.1.2.1 Time derivatives of rotation matrices	37
2.1.2.2 Coordinate system definitions	38
2.1.3 Rigid Body Dynamics	42
2.1.4 Aerodynamics Model	45
2.1.4.1 Rotor Inflow Models	46
Dynamic inflow model	46
Free-vortex wake model	47

2.1.4.2	Fuselage and empennage aerodynamics	48
2.1.4.3	Tail rotor aerodynamics	50
2.1.5	Flexible Beam Dynamics	50
2.1.6	Hub Loads	52
2.1.6.1	Vibratory hub loads	52
2.1.7	Rotor-Airframe Coupling	53
2.1.7.1	Rotor Blade Boundary Condition	54
2.1.7.2	Hub Response	56
2.1.8	Trim	57
2.1.8.1	Basic Trim Equations	58
2.1.8.2	Trim with Free Wake	60
2.1.8.3	Trim with Flexible Hub	60
2.2	Engine-Airframe Coupling	63
2.2.1	Mathematics of Dynamical Systems	63
2.2.2	Iterative Harmonic Balance Solution	65
2.2.2.1	Subcomponents	65
2.2.2.2	Interaction elements	66
2.2.2.3	Solution procedure	67
2.2.3	General Formulation of Frequency Based Substructuring	71
2.2.3.1	Rigid Interface	72
2.2.3.2	Flexible Interface	74
2.2.3.3	Rigid and flexible interfaces	75
2.2.3.4	Damping	76
2.2.4	Validation: Simple Test Case	77
3	Modeling Details	82
3.1	Baseline Helicopter Rotor Model	82
3.2	Drivetrain Model	83
3.3	Airframe Model	84
3.4	Engine Model	85
3.5	Airframe-Engine Interface	86
3.5.1	Fore mount	87
3.5.2	Aft mount	87
3.5.2.1	Strut geometry and stiffness matrices	88
3.6	Airframe-Engine Coupling Validation	90
4	Engine Mount Parametric Study	115
4.1	Baseline Results	115
4.2	Torque Tube Stiffness Sweep	119
4.3	Symmetric Strut Stiffness Sweep	120
4.3.1	Uniform strut stiffness effects	121
4.3.2	Damping effects	122
4.3.3	Individual strut stiffness effects	122
4.4	Asymmetric Strut Stiffness Sweep	123
4.5	Minimizing Engine Response	124

4.5.1	Minimizing individual mount response	125
4.5.2	Minimizing maximum mount response	126
4.5.3	Minimizing mount response at pairs of points	127
4.5.4	Minimizing total response	128
4.5.5	Symmetric strut design	129
4.5.6	Asymmetric strut design	130
4.6	Summary	130
5	Coupled Rotor-Airframe-Drivetrain Analysis	160
5.1	Baseline Coupling Results (Prescribed Airloads)	160
5.2	Rotor-Airframe-Drivetrain Coupling	162
5.2.1	Hub motion	162
5.2.2	Blade loads	163
5.2.3	Hubloads	165
5.2.4	Airframe Vibrations	166
5.3	Engine modeling	167
6	Summary and Conclusions	201
6.1	Summary	201
6.2	Key Conclusions	203
6.2.1	Engine-Airframe Coupling	203
6.2.2	Rotor-Drivetrain-Airframe-Engine Coupling	204
6.3	Recommendations for Future Work	206
	Bibliography	209

List of Figures

1.1	Frequencies of vibration throughout aircraft [77]	29
1.2	Vibration levels as a function of forward flight speed [78]	30
1.3	Impact of vibrations on helicopter development [11]	31
1.4	Representation of system dynamics in three domains [59]	32
2.1	PRASADUM non-rotating coordinate systems (adapted from [79]) . .	41
2.2	PRASADUM blade coordinate systems [79]	43
2.3	Weissinger-L lifting surface model for rotor blade	49
2.4	Free-vortex wake model of rotor	49
2.5	Overview of substructuring components	70
2.6	Simple spring-mass system with two substructure components	73
2.7	Schematic of 8-DOF mass-spring-damper system $m_1 = m_3 = m_7 =$ $m_8 = 1, m_2 = m_6 = 2, m_4 = m_5 = 4 k_i = 1, c_i = 0.01, i = 1, 2, \dots, 9$. .	79
2.8	Comparison of NASTRAN and substructuring results for validation test case without any damping	80
2.9	Comparison of NASTRAN and substructuring results for validation test case with different damping types	81
3.1	Blade mass distribution	92
3.2	Blade flap bending distribution	93
3.3	Blade lag bending distribution	94
3.4	Blade torsional stiffness distribution	95
3.5	Rotor blade natural frequencies	96
3.6	RSRA drivetrain model (Ref. [85])	101
3.7	Mode shapes of drivetrain model with free-free boundary condition .	103
3.8	Mode shapes of drivetrain model with fixed engines	104
3.9	NASTRAN FE model of airframe	105
3.10	NASTRAN FE model of GE CT7-8 engine	108
3.11	Overview of Helicopter/Engine/Airframe interfaces, mounts and forc- ing node	111
3.12	Schematic of engine mount structures	112
3.13	Geometry of axial stiffness element	113

3.14	Comparison of substructuring and NASTRAN results for coupled airframe-engine model: lateral and vertical translation response magnitude and phase of left engine aft mount point to unit amplitude forcing at main rotor hub	114
4.1	Hub load amplitudes ($C_W/\sigma=0.082$)	133
4.2	Breakdown of 4P engine mount response from individual hub load component contributions ($C_W/\sigma=0.082, \mu=0.233$)	134
4.3	Breakdown of 8P engine mount response from individual hub load component contributions ($C_W/\sigma=0.082, \mu=0.233$)	135
4.4	Total transverse response with forward speed ($C_W/\sigma=0.082$)	136
4.5	4P transverse response of engine mount points for various torque tube stiffnesses	137
4.6	Schematic of engine mount structure	138
4.7	Transverse response of engine mount points for variations in all 6 strut stiffness matrices.	139
4.8	Transverse 4P response at engine mounts for variations in stiffness and damping of all 6 struts.	140
4.9	Transverse 8P response at engine mounts for variations in stiffness and damping of all 6 struts.	141
4.10	Transverse 4P response of engine mount points for left/right symmetric variations in each individual strut holding all others at baseline values.	142
4.11	Transverse 8P response of engine mount points for left/right symmetric variations in each individual strut holding all others at baseline values.	143
4.12	Effects of changes in left or right strut stiffness on 4P engine response	144
4.13	Effects of changes in left or right strut stiffness on 8P engine response	145
4.14	Effect of minimizing response at individual engine mount point on response at other points: change in amplitude with respect to vibration for baseline strut design	146
4.15	Effect of minimizing response at individual engine mount point on response at other points: change in amplitude with respect to vibration for baseline strut design	147
4.16	Effect of minimizing response of both fore or aft mount points: change in amplitude with respect to vibration for baseline strut design	148
4.17	Effect of minimizing response of left or right engine mount points on response at other points: change in amplitude with respect to vibration for baseline strut design	149
4.18	Effect of minimizing engine total engine response: change in amplitude with respect to vibration for baseline strut design	150
4.19	Effect of stiffer struts and stiffer torque tube on 4P and 8P engine mount response	151

5.1	Effects of coupling on flap bending moments for UH-60A using measured airloads (C8534)	169
5.2	Effects of coupling on flap bending moment peak-to-peak amplitude and harmonics for UH-60A using measured airloads (C8534)	170
5.3	Effects of coupling on flap bending moment higher harmonics for UH-60A using measured airloads (C8534)	171
5.4	Effects of coupling on chordwise bending moments for UH-60A using measured airloads (C8534)	172
5.5	Effects of coupling on chordwise bending moment peak-to-peak amplitude and harmonics for UH-60A using measured airloads (C8534)	173
5.6	Effects of coupling on chordwise bending moment higher harmonics for UH-60A using measured airloads (C8534)	174
5.7	Effects of single degree of freedom 4P hub motion on mid-span flap bending moment	175
5.8	Effects of single degree of freedom 4P hub motion on mid-span chordwise bending moment	176
5.9	Effects of single degree of freedom 4P hub motion on mid-span torsion moment	177
5.10	Effects of single degree of freedom 8P hub motion on mid-span flap bending moment	178
5.11	Effects of single degree of freedom 8P hub motion on mid-span chordwise bending moment	179
5.12	Effects of single degree of freedom 4P hub motion on mid-span torsion moment	180
5.13	1/2 Peak-to-peak hub translation resulting from coupling with airframe and drivetrain	181
5.14	1/2 Peak-to-peak hub roll and pitch rotation resulting from coupling with airframe and drivetrain	182
5.15	1/2 Peak-to-peak hub yaw rotation resulting from coupling with airframe and drivetrain	183
5.16	Effects of coupling on mid-span blade loads	184
5.17	Effects of coupling on vibratory flap bending	185
5.18	Effects of coupling on vibratory flap bending higher harmonics	186
5.19	Effects of coupling on vibratory lag bending	187
5.20	Effects of coupling on vibratory lag bending higher harmonics	188
5.21	Effects of coupling on vibratory torsion moment	189
5.22	Effects of coupling on vibratory torsion moment higher harmonics	190
5.23	Effects of coupling on 4P hub loads	191
5.24	Effects of coupling on 8P hub loads	192
5.25	Effects of coupling on 4P pilot/co-pilot seat vibrations	193
5.26	Effects of coupling on 8P pilot/co-pilot seat vibrations	194
5.27	Effects of engine modeling on 4P hub loads	195
5.28	Effects of engine modeling on 8P hub loads	196
5.29	Effects of engine modeling on 4P pilot/co-pilot seat vibrations	197
5.30	Effects of engine modeling on 8P pilot/co-pilot seat vibrations	198

5.31 Effects of engine modeling on 4P engine vibrations 199
5.32 Effects of engine modeling on 8P engine vibrations 200

List of Tables

3.1	Main rotor properties	91
3.2	Main Rotor Blade Frequencies	97
3.3	Airframe properties	98
3.4	Tail rotor geometry	99
3.5	Rotor blade discretization parameters	100
3.6	Wake discretization parameters	100
3.7	Inertia and stiffness properties of RSRA drivetrain model (Ref. [85]) .	102
3.8	Speed ratios of drivetrain components	102
3.9	Natural frequencies of drivetrain model with free-free boundary condition	103
3.10	Natural frequencies of drivetrain model with fixed engines	104
3.11	Grid point ID numbers for NASTRAN airframe model	106
3.12	Natural frequencies for baseline airframe model	107
3.13	Grid point ID numbers for NASTRAN engine model	109
3.14	Natural frequencies for engine model	110
3.15	Coordinates for aft engine struts	113
4.1	Amplitude of 4P engine mount point displacement response (in) to unit hub force (lb) or moment (ft-lb)	152
4.2	Amplitude of 8P engine mount point displacement response (in) to unit hub force (lb) or moment (ft-lb)	153
4.3	Baseline vibration levels at engine mount points at 100 knots	154
4.4	Strut stiffness factors required to achieve minimum 4P or 8P response at each engine mount	155
4.5	Largest possible reduction from baseline in 4P and 8P transverse for each mount point for symmetric and asymmetric strut stiffness values	156
4.6	Strut stiffness factors that produce minimum response for different targets	157
4.7	Summary of parametric studies performed	158
4.8	Strut stiffness factors that produce minimum response for different targets	159

Abbreviations

a_{yz}	Transverse acceleration, $a_{yz} = \sqrt{a_y^2 + a_z^2}$
C	Damping matrix
K	Stiffness matrix
M	Mass matrix
M_x	Roll moment
M_y	Pitching moment
NP	N per rev
ψ	Azimuth angle
Y	Admittance matrix
Z	Impedance matrix
ϵ	ODE residual
ω	Natural frequency
CBM	Chordwise bending moment
CFD	Computational fluid dynamics
CMS	Component mode synthesis
CSD	Computational structural dynamics
DAMVIBS	Design Analysis Methods for Vibrations
DOF	Degree of freedom
FBM	Flap bending moment
FBS	Frequency based substructuring
FE	Finite element
FEM	Finite element model
FRF	Frequency response function
NASTRAN	NASA Structural Analysis
PRASADUM	Parallelized Rotorcraft Analysis for Simulation and Design, UMD
TM	Torsion moment

1 Introduction

Vibrations have been acknowledged as a problem in helicopters even preceding their inception, in the early days of the autogiro. Though the mechanisms responsible for helicopter vibrations are complex and have not been completely understood by designers, the existence of helicopter vibration is likely unmistakable to anyone who has ever heard a helicopter fly overhead. One must surely assume that the characteristic “whop-whop-whop” sound is accompanied by some significant vibrations. Vibrations are understood to arise from periodic motion, so the cyclic nature of the helicopter rotor motion, unsurprisingly, gives rise to vibrations. Furthermore, the need to reduce helicopter vibrations is not difficult to understand for anyone who has driven a car down a bumpy road. Indeed, continued exposure to high levels of vibrations is, at the very least, uncomfortable, if not dangerous to helicopter passengers and crew. Not only that, but the vibrations felt by the human occupants of the helicopter are transmitted throughout the entire aircraft, leading to fatigue and eventual failure of structural components. Finally, it appears that vibrations can affect the performance of the engines once installed in the vehicle.

Despite the large negative effects of vibrations in helicopters, actual vibration levels inside the airframe are difficult to predict precisely, and are usually not

known until flight testing of prototype designs. At this post-production stage, a full redesign is unlikely, so the problems are addressed with add-on fixes such as absorbers or isolators. Because these additional components were not necessarily included in the vehicle design, they carry penalties in terms of cost, weight, and performance. Although these penalties will always exist for vibration reduction solutions, if vibration prediction capabilities are improved, appropriate trade studies could be conducted during design to mitigate them.

All of these factors highlight the importance of modeling how the rotor, airframe, drivetrain, and engines interact to develop the most complete understanding of the total vibration story. This understanding will enable designers of future helicopter concepts to better anticipate possible vibration issues and include solutions in the design process. The present research addresses the helicopter vibration problem by using a few different analysis techniques to examine the ways in which components of the coupled rotor-airframe-drivetrain-engine system interact with each other. This chapter serves to introduce the thesis by way of explaining the background and motivation for the analysis, examining the relevant existing work in the field and outlining the contributions of the dissertation.

1.1 Background

Vibrations in helicopters stem from a variety of sources, including the main and tail rotors, engine, and transmission as well the interaction between the complex rotor wake and the airframe. Figure 1.1 illustrates which characteristic frequencies

dominate the vibrations at various points in the aircraft. As seen in the figure, the main source of vibrations in helicopters is the main rotor, that is, the frequencies present in the vibrations are integer multiples of the blade passage frequency, N_b/rev , where N_b is the number of blades on the main rotor. Frequencies associated with the tail rotor and drivetrain are also present, though in smaller, more isolated regions of the airframe.

To understand the mechanisms that contribute to the vibrations from the main rotor, it is helpful to consider the trend of vibration level in helicopters as a function of airspeed, shown in Fig. 1.2. The two regions of relatively higher vibrations point to the leading cause of main rotor vibrations. First, at the low-speed transition region between hover and forward flight, $\mu = 0.1$, the rotor is operating largely in its own wake and experiences blade-vortex interactions, where the trailed vortices from each preceding blade are impinging on the subsequent passing blades. At moderate increased speeds, a reduction in vibration is seen as the rotor wake is swept behind the rotor. Finally, at higher speeds, $\mu > 0.3$, compressibility effects are introduced due to the transonic speeds at the blade tips, leading to further increases in the vibration levels. As such, even if a helicopter might be capable of achieving higher speeds, vibrations could limit the forward flight speeds a helicopter could achieve.

1.2 Motivation

As previously noted, helicopter vibrations have a number of negative impacts for human occupants, structural components, and engine performance. As a result,

a variety of approaches have been developed over the years to alleviate the problem of vibration in helicopters. The methods used to address vibration differ in their categorization as either active or passive methods, as well as where in the sequence of transmission from the rotor to the fuselage the method is addressing the problem, which Loewy categorizes as “source alleviators”, “force attenuators”, or “amplitude reducers” [1]. The source alleviators are methods that address the problem of vibrations at the source by attempting to reduce the level of vibration produced by the rotor. Methods that fall into this category are passive devices such as pendulum [2] or bifilar absorbers [3], or active methods like higher harmonic control (HHC) [4], individual blade control (IBC) [5], or active trailing edge flaps [6]. Force attenuators operate between the source of the vibration, namely the main rotor, and the airframe. They do nothing to reduce the vibrations produced by the rotor, but instead reduce the level of vibration that is transmitted to the airframe. These methods typically utilize flexible mount structures connecting the rotor or gear box to the airframe [7]. Amplitude reducers are used in specific points in the airframe to counterbalance the vibrations. This typically takes the form of vibration isolators for specific components in the vehicle, such as seats, fuel tanks, or other equipment where a low vibration environment is highly desirable. Additionally, dynamic absorbers can be placed at different points in the airframe to effectively mitigate vibrations. These might utilize components such as batteries as the mass in the absorber. A number of papers exist that review the details and relative merits and drawbacks of the various methods, the most widely cited being by Reichert [8] and Loewy [1]. Although both papers are more than 30 years old, they represent a com-

prehensive view of the primary methods of vibration reduction still being used and investigated today. Friedmann and Millott and Kessler also provide more recent reviews of active control strategies [9, 10].

Despite the demonstrated effectiveness of these vibration reduction strategies, they have generally been utilized to address vibration issues in existing helicopters when flight tests made the existence of such issues apparent. Even for helicopters that are not yet in production, at the point of flight testing, only small changes to the overall design are economically feasible. In 1988, Kvaternik estimated that the weight penalty associated with with vibration reduction devices could be as much 2.5% of the gross weight, resulting in a 10-15% reduction in mission payload [11]. Further, Kvaternik illustrated the additional cost associated with vibration, reproduced in Fig. 1.3. From these observations, it is clear that adequately accounting for vibrations at an early stage of the design process will be essential for efficiently achieving close to “jet-smooth” flight in the next generation of rotorcraft.

Accurate prediction of vibrations requires careful consideration of the three main components involved in computing vibration levels throughout the aircraft: (1) the vibratory forcing exerted on the aircraft, primarily by the main rotor, (2) the vibratory response of the elastic airframe, and (3) the coupling between the main rotor and airframe. Further, if vibration effects on the engine are to be examined, as in this work, detailed modeling of the engines as well as the coupling between the engines and airframe are required.

One of the difficulties associated with predicting the vibrations of the engine due to main rotor forcing lies in the fact that the finite element models associated

with the engine and airframe are produced by separate entities. Due to various restrictions, detailed finite element models of either sub-system, or models refined by system identification techniques based on shake test data are not readily available. Consistent coupling of the two models requires significant disclosure of proprietary information and often necessitates modifications to one or both mathematical models. Additionally, due to the degree of complexity of the airframe finite element (FE) models required for accurate prediction of loads, parametric studies or optimization sweeps are computationally intensive. To resolve these practical difficulties and circumvent logistical and legal restrictions, dynamic substructuring can be used to easily couple models together without sharing the proprietary FE models of the constituent components.

The present research is focused on fully integrating a comprehensive rotor analysis with a flexible drivetrain as well as coupling finite element models of the airframe and engine. Due to the difficulty in acquiring access to full proprietary models of the airframe or engine from the respective manufacturers, a frequency-based substructuring method was used to facilitate the coupling between the airframe and engine models.

1.3 Literature Review

Accurate vibration prediction in helicopters is a multi-faceted and not completely resolved problem. It requires accurate vibratory loads from the rotor, detailed structural dynamics models of the airframe and other sub-components, and

full accounting of the coupling between the rotor, airframe, and all connected components. Prior research associated with these various facets are discussed in this section. While not all of these aspects are directly addressed in this research, the existing research provides necessary context. The research discussed includes the state-of-the-art in rotor vibratory loads prediction and airframe structural modeling, rotor-airframe and rotor-drivetrain coupling, and the substructuring methods that are the basis for the engine-airframe coupling examined in this work.

1.3.1 Rotor Vibratory Loads

Because the primary source of vibrations in helicopters is the main rotor, the ability to accurately predict airframe and engine vibratory loads requires a reliable aeromechanics model of the rotor. Great strides have been made in the past decade at significantly improving the prediction of rotor loads. A summary of these improvements and the current state-of-the-art in rotor loads predictions is given by Datta, Nixon, and Chopra [12].

Periodic examination of the state-of-the-art in rotor loads prediction has been done over the past 45 years through workshop-type settings, in which specialists from government, industry, and academia have compared independent results for a common problem, in an effort to share experience. Ormiston provided one of the first attempts at assessing the state-of-the-art in rotor loads prediction [13]. For this study, airloads, bending moments, vibratory hub shears and other results for a hypothetical, idealized rotor model were compared among ten different participants.

Disagreements among the results were attributed to differences in numerical solution methods as well as structural dynamics and aerodynamics modeling.

In the 1990s, another multi-agency study was conducted, this time comparing vibratory hub load predictions among eight advanced aeroelastic codes with test data for the Westland Lynx helicopter [14]. High speed flight was found to represent a particular deficiency in vibratory loads calculations. Free wake modeling was found to be particularly important in improving predictions at both low and high speed, however further enhancements to the aerodynamic modeling such as fuselage upwash and unsteady aerodynamics provided only moderate enhancements, and most codes differed from flight test results by around 50% at the high speed flight condition.

More recent studies have focused on the inclusion of computational fluid dynamics (CFD) methods in rotorcraft analysis. The use of CFD drastically improves the prediction of aerodynamic loads on the rotor, leading to significant improvements in rotor loads prediction capabilities. A review article by Datta, Nixon, and Chopra [12] provides a summary of the more recent improvements made in rotor loads predictions, specifically due to the increased use of CFD.

1.3.2 Airframe Structural Dynamics Modeling

One way the industry sought to decrease the reliance on add-on vibration reduction devices was through improved modeling of the airframe structural dynamics. In the 1980s, NASA, together with the four major helicopter manufacturers carried out the DAMVIBS program (Design Analysis Methods for Vibrations) with a goal

to improve the capabilities of airframe finite element models for predicting vibratory loads throughout the airframe [15]. Bell, Boeing, Sikorsky, and McDonnell-Douglas all participated in the program, and their individual efforts are summarized in References [16], [17], [18], and [19].

The efforts of the program focused on four major technology areas: (1) finite element modeling, (2) difficult components studies, (3) coupled rotor-airframe vibrations, and (4) airframe structural optimization. The bulk of work by the industry partners was focused on the first two of these, while the final two were meant to include contributions from government and academia subsequent to completion of the efforts in the first two.

The goals of the finite element modeling portion of the program were not only to develop detailed finite element models, but also to gain a better understanding of the importance of including various components in the models. As part of this effort, finite element models were developed for the metal airframes of the AH-64A [20], UH-60A [21], and Model 360 [22], as well as two composite airframes (part of the Advanced Composite Airframe Program (ACAP) of the Army) D292 [23] and S-75 [24]. The models were correlated against vibration test data, and in all instances, satisfactory agreement between test and analysis was found only up to about 10 Hz, with generally poor agreement above 20 Hz. It was also found that the effects of testing boundary conditions were important and that better modeling of damping was needed in the finite element analyses.

The DAMVIBS difficult components studies [25,26] aimed to determine which of the secondary structures of the aircraft have the most significant effects on the

prediction of the airframe natural frequencies. These structures include components such as landing gear, canopy glass, tail rotor drive shaft, main rotor pylon/transmission, and engine and fuel, are difficult to model and as such, were typically represented as lumped masses in the finite element model. Components were systematically removed from the airframe, and ground vibration tests were performed after each removal. Test results were compared with analysis for the corresponding model. Overall, it was found that detailed modeling of secondary structure panels and canopy glass as well as the tail boom was required for satisfactory agreement between test and analysis, while simplified lumped mass or elastic line representations were adequate for components such as the tail rotor drive shaft, engines, fuel, main rotor pylon, transmission, and soft mounted black boxes. For this work, it is worth noting that although the lumped mass engine model was deemed adequate for predicting the overall airframe natural frequencies, a detailed engine model would clearly be required for vibration studies on the engine itself.

Finally, each of the participating companies used their own in-house prediction codes to conduct coupled rotor-airframe analysis of the same AH-1G airframe and rotor models and compared results with existing vibration test data. The predicted 2/rev vibrations for this 2-bladed helicopter did not agree well with the test data for any of the participants. Although some secondary studies suggested that aerodynamic interactions between the rotor wake and airframe, particularly the tail boom, could be as important as the mechanical coupling between the rotor and airframe, this portion of the program largely ended with the conclusion that existing comprehensive analysis codes were not good enough for reliable vibrations prediction

during design. Though specific improvements to coupled rotor-airframe vibrations prediction were not made under the DAMVIBS program, the results of those initial studies led the way for industry and academia to perform focused research in this area in the ensuing years. This work will be discussed in the next section.

1.3.3 Rotor-Airframe Coupling

As indicated previously, vibration analysis in helicopters has historically been carried out by applying hub loads from a separate rotor analysis as a forcing function on the airframe model in order to determine vibration levels at various points throughout the airframe. In this situation, the hub loads are computed with the assumption that the hub is fixed. Any interaction between the rotor and airframe is accounted for only by the addition of an “equivalent” rotor mass in the airframe model. However, this level of analysis does not adequately account for the coupling between the rotor and the airframe, that is the effect that the flexibility of the airframe might have on the rotor hub loads that are being applied. This section will provide an overview of the ways in which this coupling has been modeled.

Rotor-body coupling, a general term used to describe the act of coupling the motion of the rotor hub to some other body, whether flexible or not, has been accomplished in a variety of ways. The earliest methods of coupling rotor and fuselage dynamics employed impedance matching techniques. The rotor or airframe impedance is the mathematical relationship between the vibratory forces and displacements at the hub. An impedance matching technique seeks a solution to the individual rotor

and airframe problems in which the impedance is the same between the two parts – that is, the solution for the coupled rotor-airframe should converge to the same forces and displacements at the hub. Gerstenberger and Wood [27] were the first to describe a general analytical method for helicopter analysis in which the flexible blade dynamics were coupled to the dynamics of the fuselage through impedance matching. Staley and Sciarra [28] utilized an explicit impedance matching technique in which the rotor hub loads were assumed to be composed of those calculated with a fixed hub condition in conjunction with a correction due to small vibratory hub motions. The airframe dynamics was represented by a mobility matrix relating the vibratory hub motion to applied unit vibratory hub forces. Similar impedance matching techniques have also been used in studies by Hohenemser and Yin [29], Hsu and Peters [30], and Gabel and Sankewitsch [31]. These studies utilized very simplified rotor models and aerodynamics, but were useful in understanding some basic phenomena and providing support for the notion that rotor-body coupling has a significant impact on vibratory loads and should be accounted for if accurate vibration predictions are desired.

Other researchers have developed fully coupled analyses in which the fuselage equations of motion are coupled to the rotor equations of motion. Many of these analyses utilize only linear terms in the rotor analysis and again use highly simplified aerodynamic and/or fuselage modeling. Analysis by Kunz [32] included only flapping motion in the rotor, rigid pylon and rigid fuselage with hub-fixed as well as flexibility in pitch allowed. Rutkowski [33] only considered vertical bending of rotor. Again, although the numerical results of these simplified studies are of limited use, the

demonstration of the effects of coupling are very valuable in understanding the fundamentals of those interactions and spurring further research.

Stephens and Peters [34] did not present any numerical results, but performed a comparison of an iterative method to fully coupled rotor-body equations. Although the iterative method has some disadvantages with respect to implementation and convergence, it was demonstrated that both methods were equally rigorous, despite implications that the iterative method was more approximate.

Given the importance of nonlinear forces in calculating rotor vibratory loads, a coupled analysis in which the flap, lag, and torsion dynamics of the rotor blades are fully accounted for is necessary. Warmbrodt and Friedmann [35] derived equations representing consistent structural coupling between an elastic rotor and six rigid body modes of the fuselage. Bir and Chopra [36] similarly developed analysis in which an elastic rotor was coupled to a fuselage with rigid body degrees of freedom at the hub. The analysis was developed specifically for investigating the response of a rotor due to a three-dimensional gust, though some vibration results were also noted.

Fledel [37] developed a coupled rotor-body formulation that accounted for dynamic coupling between rotor and body as well as the interactional effect of body upwash on the rotor. The body could undergo vertical bending and pitching/plunging rigid body motions. Several parameters were investigated for effects on vibratory hub loads and body vibrations. These included blade stiffness, hub location, fuselage stiffness and rotor/body clearance. The rotor and fuselage stiffness as well as rotor/body clearance were found to have a large effect on vibratory hub loads.

Works by Juggins [38] and Hansford [39] detail the development of Coupled Rotor Fuselage Model (CRFM) at Westland Helicopter. This is a comprehensive rotor analysis code using fully coupled non-linear aeroelastic equations with hub motion. Early results showed that hub load predictions were significantly improved with the addition of hub motion. Hansford also noted that a high fidelity NASTRAN fuselage model would be required for accurate prediction of hub motion and airframe vibration response.

Vellaichamy and Chopra [40, 41] performed a coupled rotor-body vibration analysis in which a flexible stick model of an airframe was coupled to a rotor with flexible blades undergoing elastic flap, lag, torsion, and axial deflection. The coupling was accomplished through an iterative procedure. These studies emphasized the role of blade structural nonlinearities and rotor-body coupling in the prediction of vibration magnitudes.

Chiu and Friedmann [42] developed a coupled rotor-fuselage aeroelastic model that incorporated active control of structural response (ACSR) in the fuselage. Their results showed again that nonlinear couplings and fuselage motion is important for vibration prediction, however the trim and blade elastic response were shown to be insensitive to fuselage motion.

A study conducted by Yeo and Chopra investigated the effects of rotor-fuselage coupling on vibration analysis [43–47]. For this analysis, a coupled rotor/fuselage vibration model was developed that incorporated consistent structural, aerodynamic, and inertial coupling effects. Initial studies utilized an elastic line model representing an AH-1G helicopter coupled with both a 4-bladed hingeless rotor [43] and

the 2-bladed teetering rotor associated with the AH-1G model [46]. These studies demonstrated that the flexible fuselage could have a pronounced effect on the predicted fuselage vibrations.

A subsequent study examined the effects of refined models of the fuselage [47] with results compared to available flight test data. Three fuselage models were compared: an elastic line model, a 3D NASTRAN model, and a refined 3D model that included difficult components. It was determined that the refined fuselage model was essential in predicting high frequency modes. Their results showed good agreement in the prediction of 2/rev magnitude and phase of pilot seat vibration, while the 4/rev predictions were fair only in magnitude. The main rotor pylon flexibility was shown to have significant impact on the 2/rev vibration prediction and refined aerodynamics, especially a free wake model, were also necessary for improved vibration prediction.

Yang and Chopra also performed a coupled rotor-fuselage vibration study for an articulated rotor helicopter - the SH-60B, including the bifilar [48, 49]. The analysis incorporated consistent structural, aerodynamic and inertial couplings and was based on finite element methods in space and time. The coupled rotor, absorbers and fuselage equations were transformed into the modal space and solved in the fixed coordinate system. The work showed acceptable trends for magnitude and phase with flight-test data and demonstrated the importance of modeling the bifilar for correctly predicting fuselage vibrations. They also investigated the sensitivity of vibration prediction to various system faults such as blade dissimilarity due to asymmetric track/balance masses.

1.3.4 Drivetrain and Engine Studies

As highlighted in the previous section, inclusion of an airframe model has been recognized as an important factor in understanding helicopter vibrations, however, the same is not true of the drivetrain or engines. While there have been some studies that include helicopter engines and other elements of the drive system such as gear boxes, those studies have largely been focused on issues of stability and handling qualities in flight dynamics. Recently, some vibration studies have begun to include drivetrain models in the analysis. Additionally, helicopter manufacturers have long recognized that certain vibration issues arise as a result of coupling between the engines and airframes. This section will highlight the key findings in the area of rotor-drivetrain coupling as well the known issues associated with engine-airframe coupling.

1.3.4.1 Rotor-Drivetrain Coupling

As mentioned previously, the fixed hub condition often used in rotor analysis does not adequately account for the motion of the hub due to coupling with the rest of the aircraft. The previous section examined the coupling of the rotor with a flexible airframe model, however, that is not the only source of motion transmitted to the rotor. Power from the helicopter engine is transmitted to the rotor via the drivetrain, which consists of a series of flexible rotating shafts connected through gears. In the prediction of rotor vibratory loads, discrepancies have continued to exist between analysis and flight test for the chordwise bending loads. It has been

suggested that coupling between the rotor and drivetrain could influence the lag bending modes of the rotor, and so exclusion of a flexible drivetrain could be contributing to these deficiencies. Despite this, few studies exist that investigate the coupled rotor-drivetrain system with regard to vibratory loads.

Yeo and Potsdam recently examined coupled CFD-CSD analysis of rotor loads in which both a simple 1-dof drivetrain model as well as a more complicated model were included in the analysis [50, 51]. When a 1-dof drivetrain model was used, its stiffness and inertia properties were tuned to match either the drivetrain first or second torsion frequency typically found in rotorcraft. It was found that the first torsion frequency affected the phase of the structural loads, while the second torsion frequency increased both the peak-to-peak and 4/rev components of the chord bending moment, improving the overall correlation with test data. Inclusion of a more detailed drivetrain model resulted in very small improvements in the correlation of the 4/rev and 5/rev harmonics of the chord bending moment.

Similar work done by Min, et. al. [52] incorporated a simplified drivetrain model into the analysis of structural loads. It was found that the drivetrain model did not appreciably alter the natural frequencies of the rotor, though the chordwise and flatwise components of the mode shape for the collective lag bending mode and first torsion mode were significantly altered. Further, the 4-6th harmonics of the blade edgewise bending moments were significantly increased from the fixed hub condition, resulting in improved correlation with flight test data for 4P and 6P, although the 5P correlation was noticeably worse.

The lack of available studies into the effects of drivetrain modeling on rotor

vibrations points to a need for further study into this area.

1.3.4.2 Engine-Airframe Coupling

Understanding the engine response to vibratory hub loads is of particular importance given the tight tolerances in the turbomachinery. Additionally, excessive vibrations in the engine could have an adverse impact on engine performance during flight. To date, there have been very few studies in the literature looking at how main rotor hub vibrations are transmitted to the engines. The DAMVIBS program concluded that lumped mass models of the engines were adequate for predicting natural frequencies of the fuselage up to 20 Hz. However, a more detailed structural model of the engine and its coupling to the airframe is clearly required for evaluating the transmission of vibratory loads into the engine itself.

In 1970, Balke [53] reviewed the existing vibration criteria that had been established by the various engine manufacturers. He highlighted the lack of standardization of vibration criteria, not only in terms of the vibration limits themselves, but also in how those vibration levels are even defined. He stressed the need for research into determining typical vibration environments present in VTOL aircraft, as well as improved communication among the various engine manufacturers and between engine and airframe manufacturers to establish improved and standardized design and test procedures throughout the industry.

Reports from 1978 by Sikorsky, Bell and Hughes, Kaman, and Boeing [54–56] outlined each company’s experiences with problems related to the structural dynamic interactions between the rotor, airframe, engine, and drivetrain. Sikorsky

documented a total of 18 problems encountered over 25 years of development of their various platforms [54]. Of these 18 issues, 6 were related to forced vibrations of the installed engine due to main rotor aerodynamic excitations at nP for the specific helicopter. Among the problems identified by Bell [55] was vibrations on the installed engine in excess of the engine vibration limits. In addition to deficiencies in ground test methodology, they specifically pointed to the inability to predict dynamic loads from the main rotor to the engine mounts as a key shortcoming contributing to this issue. The Kaman report [57] concluded that the types of compatibility issues documented in their report would not be eliminated through improved analytical methods and instead recommended that future research focus on improved dynamic testing methods for more efficient identification of the nature of such problems once encountered.

Though each of the manufacturers stressed the need for further research into these areas, limited information has been put forth in the literature since. Some work has been done to include engine dynamics in academic modeling efforts; however, these efforts typically utilize highly simplified engine models and focus on issues related to flight dynamics, such as handling qualities and stability, without addressing vibrations [58].

1.3.5 Substructuring Methods

As computing resources have become increasingly powerful and efficient over time, the finite element structural models developed by civil, mechanical, and aerospace

engineers have become more detailed and complex; helicopter airframe models are no exception. Despite their improved availability, powerful computing resources are still at a premium, so techniques that can effectively reduce the size of these large models while still providing accurate results are necessary. Dynamic substructuring is a means of modeling and analyzing a complicated mechanical system by way of its individual subcomponents and has been a powerful tool for analysis, especially of large structures.

Substructuring is easily understood conceptually as a strategy of “divide and conquer”, that is breaking a large, complicated problem into smaller sub-problems. The solution of each of the sub-problems can then be utilized to achieve a solution to the larger original problem. de Klerk, Rixen, and Voormeeren [59] provide an overview of the historical development of formal substructuring methods from initial work in the field of domain decomposition in 1890 and the component mode synthesis methods of the 1960s that are most associated with the concept of substructuring. A variety of techniques have been developed since that time, but they all involve the same basic steps:

1. Division of the structure into subcomponents
2. Definition of connections between subcomponents
3. Analysis of individual subcomponents
4. Assembly of subcomponent analyses into the complete structure

Although the various methods that have been developed over the years differ in the

details of the individual steps, primarily steps 3 and 4, they all offer some shared advantages. First, they allow more efficient use of computing resources. Analysis of the subcomponents typically involves a reduction in the number of degrees of freedom, hence a reduction in total computational time. Further, unless changes are made in the modeling of a particular subcomponent, the individual analyses need only be done once. Substructuring also facilitates easier ability to share models between separate entities. Often the modeling of large structures is divided among different individuals or groups within an organization or even between different organizations entirely. Due to the proprietary nature of these models, sharing of modeling details can be difficult. In the substructuring process, engineers can focus the analysis on the details necessary to other partners and avoid sharing details that could be deemed proprietary.

As described by de Klerk, Rixen and Voormeeren, substructuring techniques can be classified by whether the subcomponent analysis is done in the physical, modal, or frequency domain, as well as whether the interface displacements or forces are treated as unknowns (primal or dual assembly). This is illustrated in Fig. 1.4. Substructuring techniques that analyze the subcomponents in the modal domain, that is, through a transformation from physical degrees of freedom to modal degrees of freedom, are classified as component mode synthesis (CMS) methods. Techniques that analyze subcomponents in the frequency domain through Fourier transforms or frequency response functions (FRFs), are classified as frequency based substructuring (FBS) methods. These two methods will be described in the following sections.

At this point, it is helpful to briefly define some mathematical relationships.

Typically, subcomponent models exist in the physical domain and are characterized by the mass, stiffness, damping matrices, \mathbf{M} , \mathbf{K} , and \mathbf{C} associated with a set of physical degrees of freedom, \mathbf{u} , related the equation

$$\mathbf{M}\ddot{\mathbf{u}}(t) + \mathbf{C}\dot{\mathbf{u}}(t) + \mathbf{K}\mathbf{u}(t) = \mathbf{f}(t) \quad (1.1)$$

In the frequency domain, the equation of motion can be expressed as

$$[-\omega^2\mathbf{M} + i\omega\mathbf{C} + \mathbf{K}]\mathbf{U}(i\omega) = \mathbf{F}(i\omega) \quad (1.2)$$

or, more compactly,

$$\mathbf{Z}\mathbf{U} = \mathbf{F} \quad (1.3)$$

This equation can be solved for the nodal displacements and rewritten as

$$\mathbf{U} = \mathbf{Y}\mathbf{F} \quad (1.4)$$

In equation (1.3), \mathbf{Z} is commonly referred to as the structure's impedance matrix, while \mathbf{Y} in equation (1.4) is called the admittance matrix. It is straightforward to observe that the impedance and admittance matrices are inverses of each other.

1.3.5.1 Component mode synthesis

For the most part, the term dynamic substructuring has referred to the class of techniques called component mode synthesis (CMS). In CMS methods, the physical displacement coordinates are represented by a set of generalized coordinates related to a set of normalized displacement modes, or component modes. A coordinate transformation utilizing a matrix of mode shapes, or basis vectors, converts between the physical and generalized coordinates. A variety of methods that fall into the

CMS category have been developed and refined over the years, and they differ, in part, in the variety of definitions for sets of component modes. A general overview of the methods is given here, however, a more thorough overview including some mathematical details and examples is presented in Reference [60].

In general, the mode sets utilized in CMS methods fall into one of four categories: normal modes, constraint modes, rigid body modes, and attachment modes. These sets are defined as:

- (i) Normal modes are the eigenvectors of the system and are classified according to the boundary condition imposed on the component. The boundary conditions can be free, fixed, or loaded interface, or a combination among the boundary nodes.
- (ii) Constraint modes represent the deformation of the structure that occurs when one of the specified number of constraint coordinates is given a unit displacement, while holding the remaining constraint coordinates fixed.
- (iii) Rigid-body modes represent the undeformed motion of the component.
- (iv) Attachment modes represent the deformation of the structure due to a unit force applied to a single node.

The earliest version of a CMS method was developed in the 1960s by Hurty [61, 62]. Hurty's method utilized fixed-interface normal modes, constraint modes, and rigid-body modes. In Hurty's method, a subset of boundary nodes was selected to yield a set of statically determinate constraints, from which the rigid-body modes

were computed. The remaining boundary nodes were designated as redundant constraints, from which the constraint modes were computed. Craig and Bampton built on and generalized Hurty's work [63]. The Craig-Bampton method represents the motion of a subcomponent with fixed-interface normal modes and constraint modes, demonstrating that the use of rigid body modes is unnecessary if all boundary nodes are treated in the same manner as Hurty's redundant constraints. This modification simplified the overall formulation and programming, likely leading the Craig-Bampton method to become essentially synonymous with component mode synthesis.

Following the development of the Craig-Bampton method, CMS methods received continued attention as more researchers contributed their own modifications to the existing formulations. Methods developed by Goldman [64] and Hou [65] were formulated using only free-interface normal modes without any static modes. Benfield and Hruda [66] introduced the concept of branch modes, in which free-free boundary conditions were used on the identified primary structure and the branch modes were calculated for the remaining structures with a fixed boundary condition at the structure interface. Guyan reduction [67] was also used to determine interface loading from the attached substructures.

MacNeal [68] developed a hybrid method which utilized both fixed and free interface modes. He also suggested the inclusion of statically determined deflection influence coefficients. The addition of these coefficients, termed "residual flexibility", offers improved accuracy by accounting for the static effects of the neglected modes. Rubin [69] extended this idea adding residual inertial and dissipative effects

to further improve accuracy. Craig and Chang [70, 71] generalized the methods of MacNeal and Rubin as well as developed a new method employing residual attachment modes, which produced results comparable to or better than those obtained by other methods.

1.3.5.2 Frequency-based substructuring

The component mode synthesis techniques for substructure analysis of the prior section are formulated for use in the time domain; however, as stated previously, vibrations in helicopters exist primarily at only a few frequencies, namely integer multiples of the blade passage frequency, pN_b per rev, where N_b is the number of blades. Therefore, studies of helicopter vibrations are ideally suited to methods formulated in the frequency domain, so-called frequency-based substructuring (FBS) methods.

As illustrated in Fig. 1.4, the frequency domain representation of a subcomponent can be generated through a Fourier transform of the physical model or through frequency response functions (FRFs) obtained either analytically from the full model or the modal reduction or experimentally. Unless a modal representation is all that is available, FBS methods offer the distinct advantage that all elements of the system dynamics are embedded in the FRFs.

The classical method of frequency-based substructuring (FBS) was developed in 1988 by Jetmundsen, Bielawa, and Flannelly [72] which utilized partitioned impedance matrices for the substructure components that were then connected using graph theory. The method was originally conceived to analyze the effects of

structural changes in helicopter airframes, specifically utilizing experimentally derived mobilities [73]. Gordis, Bielawa, and Flannelly [74] generalized the Jetmundsen formulation and Ren and Beards [75] proposed a similar formulation. Another modification to the method includes reformulation such that the coupling of structures is done in a “dual” manner, in contrast to the “primal” assembly that is typically utilized. The essential difference between these two assembly methods is that the primal assembly is a coupling through interface displacements, while the dual assembly is a coupling through interface forces. What arises from the dual assembly is a method known as Lagrange multiplier frequency-based substructuring (LM FBS), formalized by de Klerk, Rixen, and de Jong [76]. This method has the advantage of utilizing the admittance matrices of the system directly. The admittance matrices consist of the frequency response relationships of the structure, and so are more easily acquired through experimental testing. For the purposes of the present work, even though the structural models used are based on the full finite element models of the structures, the proprietary nature of the data made transfer of frequency response information the most viable option for acquiring model information. Therefore, the LM FBS method of Ref. [76] forms the basis of the substructuring methodology used in this work, the mathematical details of which will be explained in Chapter 2.

Though not explored in this work, it is worth noting that a key advantage of FBS methods lies in the ease with which the methods can be applied using experimental data. More recent work in the field of dynamic substructuring has focused on improving the accuracy of the methods, both CMS and FBS, when

applied to experimental data. Some of the difficulties associated with applying substructuring analysis to experimental data include difficulty in modeling rotational degrees of freedom, truncation and experimental errors, the continuity of interfaces in contrast to the discrete nature of measurements, measurement of rigid body modes, and nonlinear effects arising from friction in joints. These issues are discussed further in Reference [59].

1.4 Scope of Current Work

The prediction of vibrations in helicopters is a multi-faceted problem. The goals of the present research are to examine the various dynamic interactions that exist within the helicopter in order to better understand the nature of those interactions and their impact on vibrations throughout the helicopter. To that end, the technical approach of the research is separated into two primary tasks:

1. **Engine-airframe coupling using dynamic substructuring.** Analysis was developed to allow coupling of airframe and engine finite element models developed by different entities. The analysis utilizes frequency-based dynamic substructuring techniques to produce an accurate coupled model while requiring only limited levels of information exchange for each of the models. This analysis produces results commensurate with those generated using NASTRAN on the full models in a fraction of the computing time, allowing for parametric studies of engine mount properties to be carried out.

2. Rotor coupling to fixed-frame components within comprehensive analysis. Existing comprehensive analysis capabilities were expanded to account for a flexible hub condition, allowing the rotor to be coupled to a flexible drivetrain and/or airframe model. The effects of these couplings on the rotor blade structural loads, fixed frame hub loads, pilot seat and engine vibrations were examined across a range of forward flight speeds.

1.4.1 Overview of Dissertation

The remainder of the dissertation consists of five chapters. Chapter 2 describes the methodology that was used for this work. This includes the existing comprehensive analysis and modifications made for rotor-airframe and rotor-drivetrain coupling as well as the substructuring framework utilized for the coupled airframe-engine analysis. Chapter 3 describes the modeling details of the rotor, airframe, engine, and engine mount structures. Chapter 4 presents the results of a parametric study performed on the properties of the engine mount structures for reduced vibrations. Chapter 5 examines the coupled rotor-airframe-drivetrain system. Finally, Chapter 6 serves to summarize the major conclusions of the current work as well as suggest directions for future study.

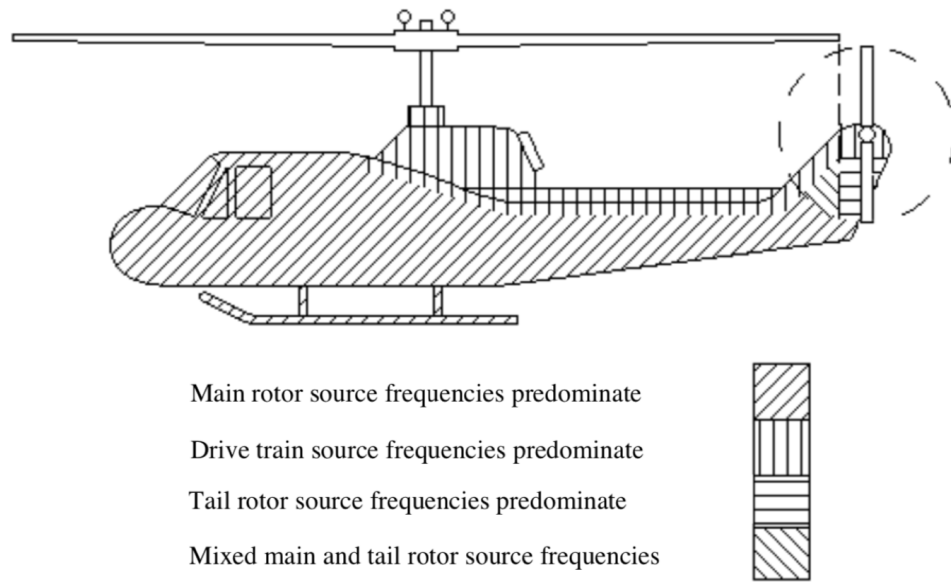


Figure 1.1: Frequencies of vibration throughout aircraft [77]

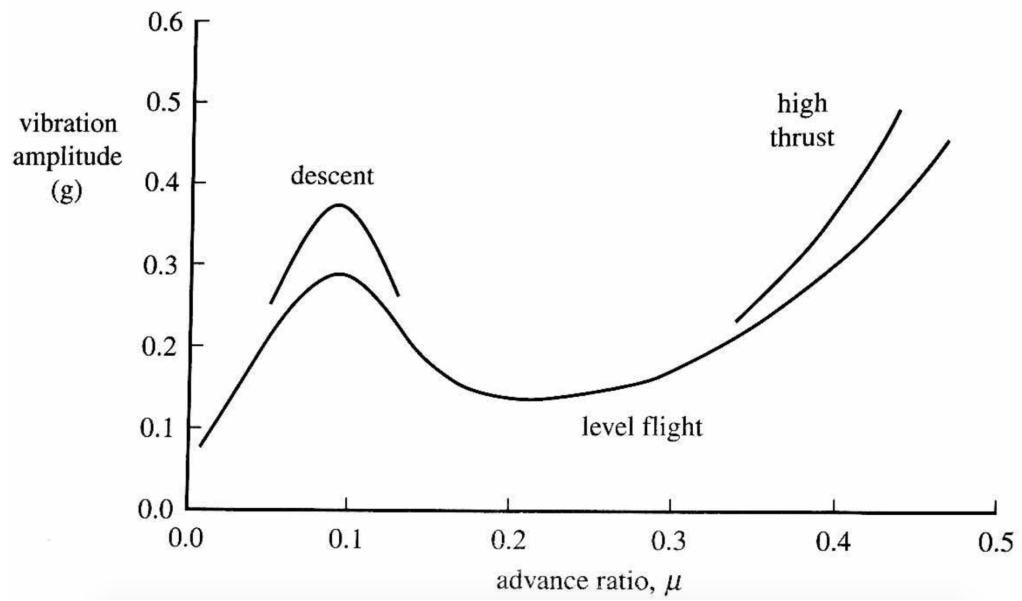


Figure 1.2: Vibration levels as a function of forward flight speed [78]

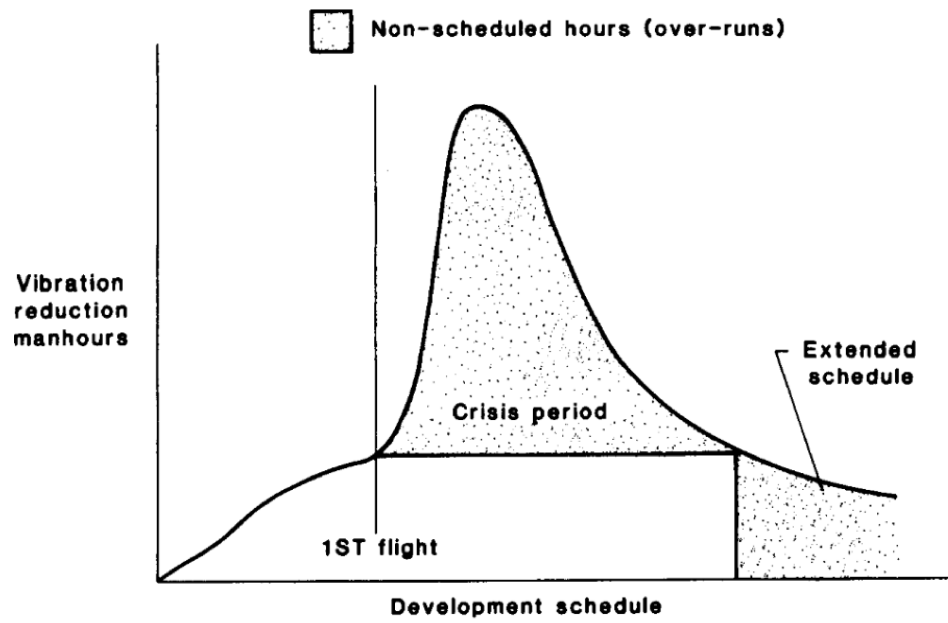


Figure 1.3: Impact of vibrations on helicopter development [11]

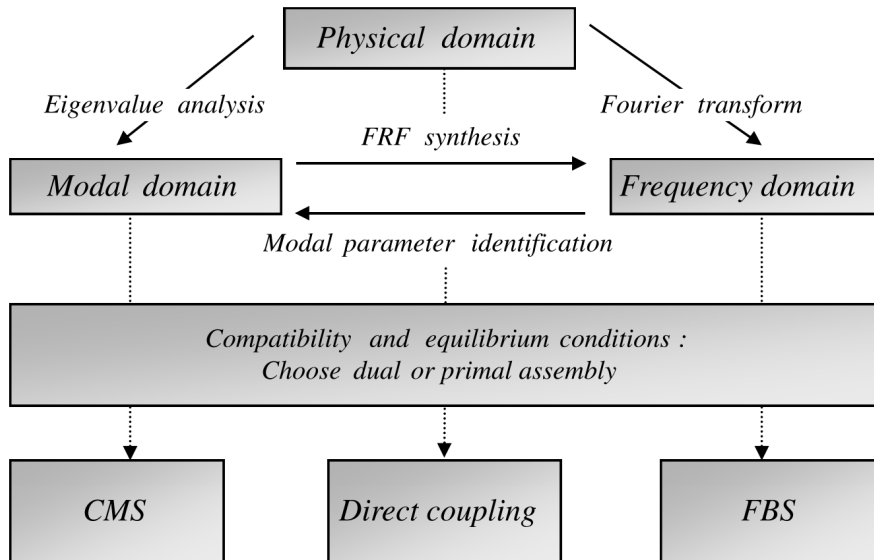


Figure 1.4: Representation of system dynamics in three domains [59]

2 Methodology

This chapter presents the details of various aspects of the mathematical modeling utilized in this work. An overview of the baseline comprehensive analysis is given first, including the blade structural and aerodynamic modeling and vehicle trim procedures. The detailed mathematical framework for coupling the rotor to the fixed frame drivetrain and airframe components is described next. Finally, details of the frequency-based substructuring framework used for the engine-airframe coupling are given.

2.1 Comprehensive Analysis: PRASADUM

The baseline rotordynamic analysis for this work was performed using PRASADUM (Parallelized Rotorcraft Analysis for Simulation and Design, University of Maryland), developed by Ananth Sridharan at the University of Maryland and based on the work in Reference [79]. PRASADUM is used to model the rotor aeromechanics and vehicle flight dynamics. The analysis in this work required several modifications to the baseline code to allow for efficient coupling of the rotor with a flexible airframe and/or drivetrain. For completeness and clarity as it pertains to these modifications, a summary of the major components of the methodology is presented here, with de-

tailed descriptions available in Ref. [79]. For the sake of brevity, some of the detailed mathematical equations have not been reproduced, particularly for aspects of the analysis not directly affected by the rotor-structure coupling. However, complete descriptions, including mathematical formulations, of all modifications made to the analysis for this coupling are included within this section.

2.1.1 Overview of Solution Method

The equations of motion governing the system dynamics are formulated in a state-space form as a system of first-order non-linear coupled ODEs of the form

$$\mathbf{f}(\mathbf{y}, \dot{\mathbf{y}}, \mathbf{u}, t) = \boldsymbol{\epsilon} = \mathbf{0} \quad (2.1)$$

Here t is the current time, \mathbf{u} is a vector of control inputs consisting of the main rotor collective and cyclic controls and tail rotor collective, and \mathbf{y} is a vector of system states. The state vector is subdivided into \mathbf{y}_F , \mathbf{y}_λ , and $\mathbf{y}_{\text{rotor}}$, defined as

- \mathbf{y}_F represents the 12 airframe rigid body states
- \mathbf{y}_λ represents the induced inflow coefficients for the main rotor and tail rotor
- $\mathbf{y}_{\text{rotor}}$ represents the vector of deflection states for all blades. In the presence of a flexible hub, this vector will also consist of states representing the hub motion.

Similarly, the residual vector, $\boldsymbol{\epsilon}$, is assembled from $\boldsymbol{\epsilon}_F$, $\boldsymbol{\epsilon}_\lambda$, and $\boldsymbol{\epsilon}_{\text{rotor}}$ defined as

- $\boldsymbol{\epsilon}_F$ are the residuals corresponding to the non-linear equations enforcing force and moment equilibrium for the fuselage rigid body motions and kinematic

compatibility between time derivatives of Euler angles and body-axes angular rates.

- ϵ_λ are the residuals corresponding to the dynamic inflow equations for the main and tail rotors
- ϵ_{rotor} are the residuals corresponding to the mode-weighted Euler-Bernoulli beam equations for the rotor blades. In the case of a flexible hub, ϵ_{rotor} will also contain the residuals for the hub motion equations.

For the rotorcraft trim problem related to in this work, the governing differential equations are numerically reduced to a set of non-linear algebraic equations, represented as

$$\mathbf{F}(\mathbf{X}) = \bar{\epsilon}_{\text{trim}} = \mathbf{0} \quad (2.2)$$

In this case \mathbf{X} is a vector of unknown trim variables, including the pilot controls, vehicle attitudes, rotor induced inflow ratios, and rotor response. The algebraic equation residuals, $\bar{\epsilon}_{\text{trim}}$, are calculated through numerical manipulation of the ODE residuals from Eqn. 2.1. HYBRD, a non-linear system solver available through the open-source library, NETLIB, is used to solve the system algebraic equations to within a user-specified threshold, δ_{trim} for an error metric $e(|\bar{\epsilon}_{\text{trim}}|)$.

2.1.2 Coordinate Systems

PRASADUM makes use of a variety of reference frames depending on what is most relevant at a given stage in the analysis. Forces and moments are resolved into the body axes to ensure equilibrium for trimmed flight. Rotating axes for the blade

deformations are also utilized. Coordinate transformations are used to transfer loads and displacements from one system to another. The coordinate transformations take the form of a rotation matrix representing a three Euler angle rotations, occurring in the following order:

- Yaw rotation about the z -axis through an angle ψ
- Pitch rotation about the intermediate y -axis through an angle θ
- Roll rotation about the intermediate z -axis through an angle ϕ

The rotation matrices for each individual rotation are given by

$$\mathbf{T}_\psi = \begin{bmatrix} \cos \psi & \sin \psi & 0 \\ -\sin \psi & \cos \psi & 0 \\ 0 & 0 & 1 \end{bmatrix} \quad (2.3)$$

$$\mathbf{T}_\theta = \begin{bmatrix} \cos \theta & 0 & -\sin \theta \\ 0 & 1 & 0 \\ \sin \theta & 0 & \cos \theta \end{bmatrix} \quad (2.4)$$

$$\mathbf{T}_\phi = \begin{bmatrix} 1 & 0 & 0 \\ 0 & \cos \phi & \sin \phi \\ 0 & -\sin \phi & \cos \phi \end{bmatrix} \quad (2.5)$$

The full rotation matrix from coordinate system A to coordinate system B, denoted \mathbf{T}_{BA} , consists of the three individual rotation matrices multiplied as

$$\mathbf{T}_{BA} = \mathbf{T}_\phi \mathbf{T}_\theta \mathbf{T}_\psi \quad (2.6)$$

The reverse transformation, from coordinate system B to coordinate system A, denoted \mathbf{T}_{BA} , is achieved through the reverse sequence of opposite rotations. It can be easily demonstrated with trigonometric identities and matrix properties that these two transformations are the transpose of each other. That is,

$$\mathbf{T}_{AB} = \mathbf{T}_{-\phi} \mathbf{T}_{-\theta} \mathbf{T}_{-\psi} = \mathbf{T}_{BA}^{\top} \quad (2.7)$$

2.1.2.1 Time derivatives of rotation matrices

Because the various rotation angles can be time-dependent and the coordinate transformations are used to transform time-dependent quantities and their derivatives, it is also necessary to know the time-derivatives of these rotation matrices.

The first and second time derivatives each of the sequential rotations are given by

$$\dot{\mathbf{T}}_{\psi} = \begin{bmatrix} -\sin \psi & \cos \psi & 0 \\ -\cos \psi & -\sin \psi & 0 \\ 0 & 0 & 0 \end{bmatrix} \dot{\psi} \quad (2.8)$$

$$\dot{\mathbf{T}}_{\theta} = \begin{bmatrix} -\sin \theta & 0 & -\cos \theta \\ 0 & 0 & 0 \\ \cos \theta & 0 & -\sin \theta \end{bmatrix} \dot{\theta} \quad (2.9)$$

$$\dot{\mathbf{T}}_{\phi} = \begin{bmatrix} 0 & 0 & 0 \\ 0 & -\sin \phi & \cos \phi \\ 0 & -\cos \phi & -\sin \phi \end{bmatrix} \dot{\phi} \quad (2.10)$$

$$\ddot{\mathbf{T}}_\psi = \begin{bmatrix} -\sin \psi & \cos \psi & 0 \\ -\cos \psi & -\sin \psi & 0 \\ 0 & 0 & 0 \end{bmatrix} \ddot{\psi} + \begin{bmatrix} -\cos \psi & -\sin \psi & 0 \\ \sin \psi & -\cos \psi & 0 \\ 0 & 0 & 0 \end{bmatrix} \dot{\psi}^2 \quad (2.11)$$

$$\ddot{\mathbf{T}}_\theta = \begin{bmatrix} -\sin \theta & 0 & -\cos \theta \\ 0 & 0 & 0 \\ \cos \theta & 0 & -\sin \theta \end{bmatrix} \ddot{\theta} + \begin{bmatrix} -\cos \theta & 0 & \sin \theta \\ 0 & 0 & 0 \\ -\sin \theta & 0 & -\cos \theta \end{bmatrix} \dot{\theta}^2 \quad (2.12)$$

$$\ddot{\mathbf{T}}_\phi = \begin{bmatrix} 0 & 0 & 0 \\ 0 & -\sin \phi & \cos \phi \\ 0 & -\cos \phi & -\sin \phi \end{bmatrix} \ddot{\phi} + \begin{bmatrix} 0 & 0 & 0 \\ 0 & -\cos \phi & -\sin \phi \\ 0 & \sin \phi & -\cos \phi \end{bmatrix} \dot{\phi}^2 \quad (2.13)$$

The individual time derivatives can then be used to construct the time derivatives of the full transformation matrix by considering the expanded derivatives of the sequential multiplication of the individual rotation matrices. These are given by

$$\begin{aligned} \dot{\mathbf{T}}_{AB} &= \frac{d}{dt}(\mathbf{T}_{AB}) = \frac{d}{dt}(\mathbf{T}_\phi \mathbf{T}_\theta \mathbf{T}_\psi) \\ &= \dot{\mathbf{T}}_\phi \mathbf{T}_\theta \mathbf{T}_\psi + \mathbf{T}_\phi \dot{\mathbf{T}}_\theta \mathbf{T}_\psi + \mathbf{T}_\phi \mathbf{T}_\theta \dot{\mathbf{T}}_\psi \end{aligned} \quad (2.14)$$

$$\begin{aligned} \ddot{\mathbf{T}}_{AB} &= \frac{d^2}{dt^2}(\mathbf{T}_{AB}) = \frac{d}{dt}(\dot{\mathbf{T}}_{AB}) \\ &= \ddot{\mathbf{T}}_\phi \mathbf{T}_\theta \mathbf{T}_\psi + \mathbf{T}_\phi \ddot{\mathbf{T}}_\theta \mathbf{T}_\psi + \mathbf{T}_\phi \mathbf{T}_\theta \ddot{\mathbf{T}}_\psi + \\ &\quad 2\left(\dot{\mathbf{T}}_\phi \dot{\mathbf{T}}_\theta \mathbf{T}_\psi + \dot{\mathbf{T}}_\phi \mathbf{T}_\theta \dot{\mathbf{T}}_\psi + \mathbf{T}_\phi \dot{\mathbf{T}}_\theta \dot{\mathbf{T}}_\psi\right) \end{aligned} \quad (2.15)$$

2.1.2.2 Coordinate system definitions

Figure 2.1 (a) shows the general set of non-rotating coordinate systems used when a fixed hub condition is assumed. These are:

- Earth-fixed axes, or gravity axes, $(\hat{\mathbf{i}}_G, \hat{\mathbf{j}}_G, \hat{\mathbf{k}}_G)$ represent an inertial reference frame used to track the motion of the helicopter in space.
- Helicopter body-fixed axes $(\hat{\mathbf{i}}_B, \hat{\mathbf{j}}_B, \hat{\mathbf{k}}_B)$ are obtained from the earth-fixed axes through a translation of the helicopter CG and three Euler rotations ψ_F, θ_F, ϕ_F , representing nose-right yaw, pitch up, and roll right motions, respectively. Rotation from earth-fixed to body-fixed axes is done with \mathbf{T}_{BG}
- Helicopter hub non-rotating axes $(\hat{\mathbf{i}}_H, \hat{\mathbf{j}}_H, \hat{\mathbf{k}}_H)$ are obtained from the helicopter body axes through a translation of the origin to the location of the hub relative to the CG, followed by two Euler rotations, α_S, β_S , representing the tilt of the shaft. There is also a 180° rotation about the intermediate y -axis. This transformation is represented by the matrix \mathbf{T}_{HB} .

Figure 2.1 (b) shows the additional non-rotating coordinate systems used when the rotor is coupled to a flexible airframe model. These are:

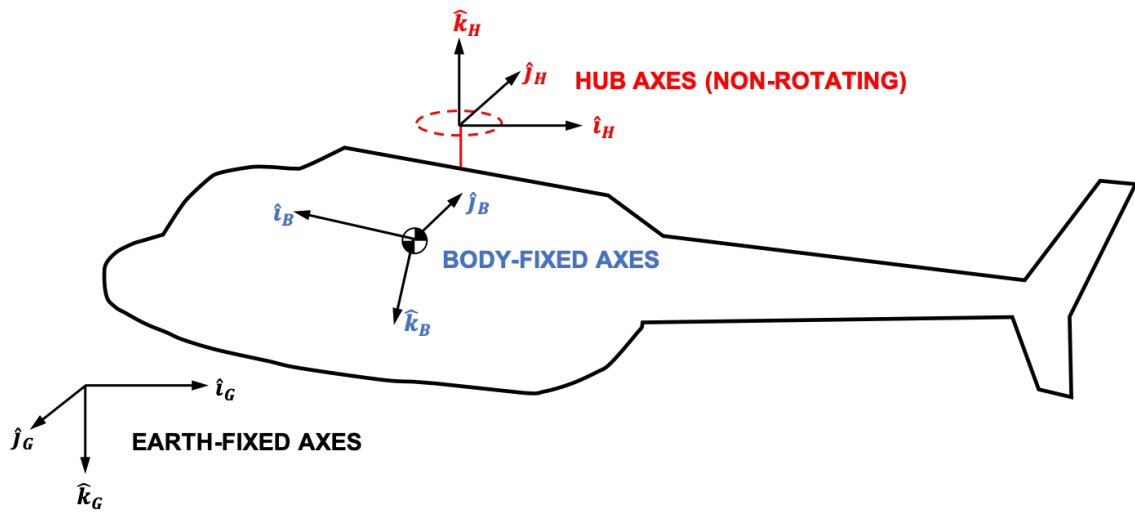
- NASTRAN axes $(\hat{\mathbf{i}}_N, \hat{\mathbf{j}}_N, \hat{\mathbf{k}}_N)$ are similar to the body-fixed axes but are rotated by 180° about the y -axis to align with the NASTRAN convention that the z -axis points up. Since the airframe model used in the analysis was generated in NASTRAN, the eigenvectors or hub frequency response functions used to compute the response of the hub are given in the NASTRAN coordinate system. Since the transformation from the body-fixed axes to the hub-fixed axes is already defined by \mathbf{T}_{HB} , it is simplest to flip the signs of the x - and z -translations and rotations of the hub in the NASTRAN axes, bringing them

into the body-fixed axes and then apply \mathbf{T}_{HB} for transformation to hub-fixed coordinates.

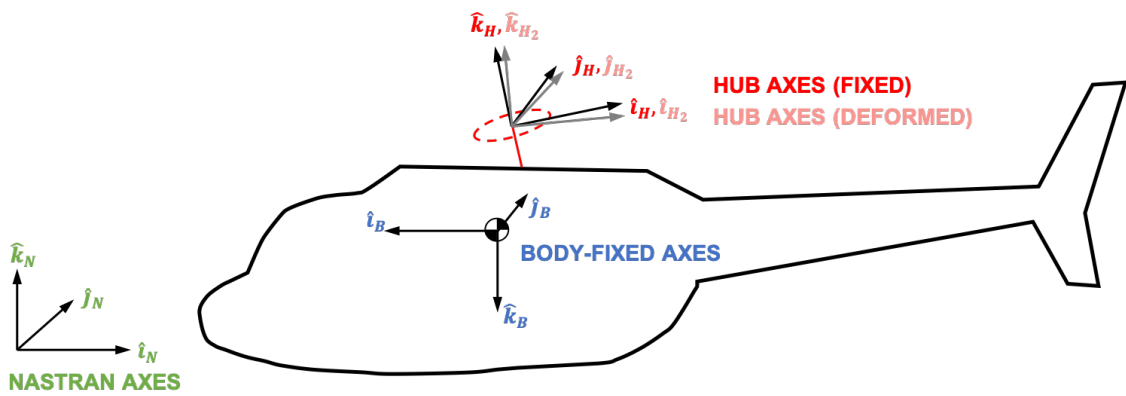
- Deformed hub axes $(\hat{\mathbf{i}}_{H_2}, \hat{\mathbf{j}}_{H_2}, \hat{\mathbf{k}}_{H_2})$ arise as a result of the motion of the hub relative to the airframe. Specifically, the application of hub forces and moments on the airframe will produce displacements, $x_{\text{hub}}, y_{\text{hub}}, z_{\text{hub}}$, and pitch and roll rotations, $\theta_{y_{\text{hub}}}$ and $\theta_{x_{\text{hub}}}$, respectively. Similarly, the hub torque is applied to the drivetrain and produces the $\theta_{z_{\text{hub}}}$ rotation. \mathbf{T}_{H_2H} is the rotation matrix for the transformation from the hub-fixed axes to the deformed hub axes.

For completeness, it is worth listing the remaining coordinate transformations from rotor hub frame to the deformed blade axes. The coordinate systems are illustrated in Fig. 2.2.

- \mathbf{T}_{RH} is the rotation matrix from the non-rotating hub axes to the rotating un-preconed blade axes. This is a rotation about the non-rotating hub z -axis through angle ψ_j for blade j , where ψ_j is the azimuth angle of blade j .
- \mathbf{T}_{UR} is the rotation matrix from the rotating unpreconed blade axes to the undeformed blade preconed axes. This transformation consists of a rotation through angle $-\beta_p$ about the unpreconed y -axis. Because of the definition of the unpreconed axes, β_p is negative for vertically upward motion of the blade tip.
- \mathbf{T}_{DU} is the rotation matrix from the undeformed preconed blade axes to the



(a) Fixed hub coordinate systems



(b) Flexible hub coordinate systems

Figure 2.1: PRASADUM non-rotating coordinate systems (adapted from [79])

deformed blade axes. This transformation is unique to every point on the blade elastic axis. The transformation consists of three translations along the the undeformed axes, representing hinge offset, axial fore-shortening due to bending, spanwise position of the beam cross-section, lead-lag displacement and flap-bending displacement. The translations are followed by three rotations arising from the flap and lag bending and elastic twist of the beam.

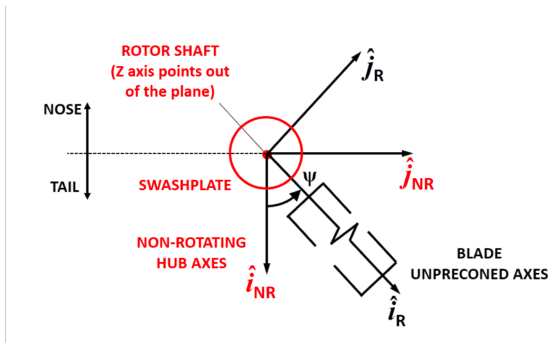
2.1.3 Rigid Body Dynamics

For the purposes of calculating the vehicle flight dynamics, the helicopter fuselage is assumed to be rigid. The airframe linear and angular velocities are obtained from the partition of the system state vector containing the fuselage states, given by

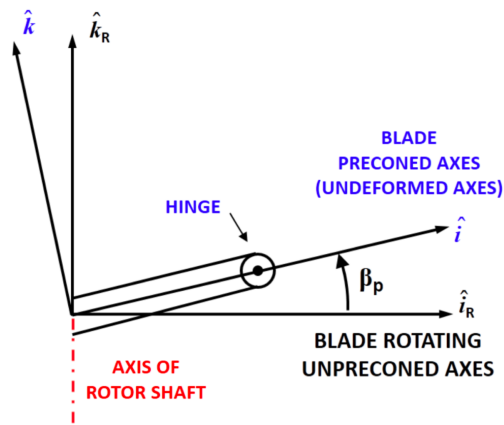
$$\mathbf{y}_F = \{u_F \ v_F \ w_F \ p_F \ q_F \ r_F \ \phi_F \ \theta_F \ \psi_F \ x_{CG} \ y_{CG} \ z_{CG}\}^T \quad (2.16)$$

where the terms $(u_F, v_F, w_F, p_F, q_F, r_F)$ are the linear and angular velocity components of the helicopter CG in the body-fixed axes, $(\phi_F, \theta_F, \psi_F)$ are the Euler angles defining the fuselage orientation with respect to earth-fixed axes, and (x_{CG}, y_{CG}, z_{CG}) represents the position of the helicopter CG in earth-fixed axes.

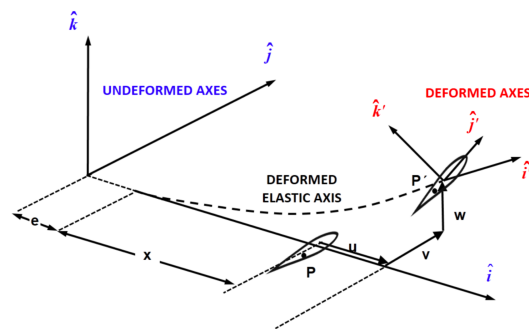
In the fuselage body-fixed axes, the force and moment equilibrium equations



(a) Rotating blade unprecone axes



(b) Blade precone axes



(c) Undeformed and deformed blade axes

Figure 2.2: PRASADUM blade coordinate systems [79]

are

$$X = m_F(\dot{u}_F + q_F w_F - r_F v_F + g \sin \theta_F) \quad (2.17)$$

$$Y = m_F(\dot{v}_F + r_F u_F - p_F w_F - g \sin \phi_F \cos \theta_F) \quad (2.18)$$

$$Z = m_F(\dot{w}_F + p_F v_F - q_F u_F - g \cos \phi_F \cos \theta_F) \quad (2.19)$$

$$L = I_{xx}\dot{p}_F - I_{xy}(\dot{q}_F - p_F r_F) - I_{xz}(\dot{r}_F + p_F q_F) - I_{yz}(q_F^2 - r_F^2) - (I_{yy} - I_{zz})q_F r_F \quad (2.20)$$

$$M = I_{yy}\dot{q}_F - I_{yz}(\dot{r}_F - q_F p_F) - I_{yx}(\dot{p}_F + q_F r_F) - I_{zx}(r_F^2 - p_F^2) - (I_{zz} - I_{xx})r_F p_F \quad (2.21)$$

$$N = I_{zz}\dot{r}_F - I_{zx}(\dot{p}_F - r_F q_F) - I_{zy}(\dot{q}_F + r_F p_F) - I_{xy}(p_F^2 - q_F^2) - (I_{xx} - I_{yy})p_F q_F \quad (2.22)$$

These equations represent half of the equations used to compute the residuals for the fuselage rigid body motions, ϵ_F . The remaining six arise from the equivalence of the linear velocity of the fuselage and the time derivative of the CG position and the kinematic compatibility between time derivatives of Euler angles and body-axes angular rates. These are represented by the following equations:

$$u_F = \dot{x}_{CG} \quad (2.23)$$

$$v_F = \dot{y}_{CG} \quad (2.24)$$

$$w_F = \dot{z}_{CG} \quad (2.25)$$

$$p_F = \dot{\phi}_F - \dot{\psi}_F \sin \theta_F \quad (2.26)$$

$$q_F = \dot{\theta}_F \cos \phi_F + \dot{\psi}_F \cos \theta_F \sin \phi_F \quad (2.27)$$

$$r_F = -\dot{\theta}_F \sin \phi_F + \dot{\psi}_F \cos \theta_F \cos \phi_F \quad (2.28)$$

The terms on the left-hand side of Eqns. 2.17-2.22 represent the total applied forces and moments about the center of gravity from the main rotor (MR), tail rotor (TR), horizontal and vertical tails (HT, VT), and fuselage aerodynamics, given by

$$X = X_{MR} + X_{TR} + X_{HT} + X_{VT} + X_F \quad (2.29)$$

$$Y = Y_{MR} + Y_{TR} + Y_{HT} + Y_{VT} + Y_F \quad (2.30)$$

$$Z = Z_{MR} + Z_{TR} + Z_{HT} + Z_{VT} + Z_F \quad (2.31)$$

$$L = L_{MR} + L_{TR} + L_{HT} + L_{VT} + L_F \quad (2.32)$$

$$M = M_{MR} + M_{TR} + M_{HT} + M_{VT} + M_F \quad (2.33)$$

$$N = N_{MR} + N_{TR} + N_{HT} + N_{VT} + N_F \quad (2.34)$$

The following sections contain further details on the calculations of each of these forces.

2.1.4 Aerodynamics Model

The aerodynamic loads are primarily the result of aerodynamic forces on individual blade sections. These forces are calculated from look-up tables based on the sectional airfoil and local velocity and Mach number at that section. The velocity at a blade section is a combination of the motion of the blade through the air and the inflow through the rotor. The rotor inflow can be calculated using a dynamic

inflow model or free wake model, both of which are briefly described in this section. In addition, the contributions of the helicopter fuselage, empennage, and tail rotor to the aerodynamic forces and moments on the vehicle are discussed.

2.1.4.1 Rotor Inflow Models

The inflow at the main rotor is calculated in two ways, depending on the level of fidelity desired in the solution, either with a dynamic inflow model or free-vortex wake model. This section provides general descriptions of both inflow models. The descriptions given in this section are meant only to summarize the main rotor aerodynamic models used in PRASADUM and are largely qualitative. For further mathematical details, refer to Ref. [79].

Dynamic inflow model

A dynamic inflow model is designed to approximately capture the time-variation of the inflow over the rotor disk. In general, the inflow for specific time at a point on the rotor disk (r, ψ) is given by

$$\lambda(r, \psi) = \lambda_0 + r(\lambda_{1c} \cos \psi + \lambda_{1s} \sin \psi) \quad (2.35)$$

where λ_0 represents the uniform inflow, λ_{1c} is the longitudinal inflow, and λ_{1s} is the lateral inflow. PRASADUM utilizes the Peters-He model [80] for the inflow, which consists of a set of coupled first order differential equations for the inflow parameters, λ_0 , λ_{1c} , and λ_{1s} .

Free-vortex wake model

For vibrations analysis, particularly at flight conditions between hover ($\mu = 0$) and transition speeds ($\mu \approx 0.1$), where blade-vortex interactions are significant, a dynamic inflow model is inadequate. Instead, an in-house free-vortex wake model, known as Maryland Free Wake is used to more accurately capture the effects of the rotor wake on the rotor aerodynamics.

The wake calculations are carried out in two parts, near wake and far wake models. In the near wake, a Weissinger-L lifting surface model is used, illustrated in Fig. 2.3. Each blade is represented using a distribution of horseshoe vortices with a bound vortex at the $1/4$ -chord. The strength of the vortex trailers is found using Helmholtz's laws for vorticity conservation. These trailers make up the near wake of the blade, which is truncated for $\Delta\psi = 30^\circ$ behind the blade. After that point, this vortex sheet is assumed to have completely rolled up and its circulation is concentrated in the free trailers from the blade tips. This is the far wake.

The tip vortices trail from the blade tips in a curved path that is discretized into straight line segments, as illustrated in Fig. 2.4. The vortices are free to convect due to the influence of the local velocity and instantaneous vorticity. The motion of the vortices is tracked using a time-accurate two-step backward predictor-corrector scheme developed by Bhagwat and Leishman [81]. The velocity field induced by the wake at any location is computed by application of the Biot-Savart law, followed by numerical integration of the induced velocity contributed by each vortex element in the flow field.

2.1.4.2 Fuselage and empennage aerodynamics

The aerodynamic forces and moments on the body of the fuselage are computed based on the flow velocity at a reference point on the fuselage, defined relative to the vehicle center of gravity. The flow velocity components comprise the components of the vehicle translational velocity and rigid body angular velocity as well as components of an interference velocity. The interference velocity is calculated from the main rotor downwash, longitudinal tilt of the rotor tip path plane and wake skew angle. From the components of the flow velocity at the reference point, the flow incidence angles are calculated, and with the dynamic pressure at the reference point, the lift, drag and moment coefficients are obtained from look-up tables based on wind-tunnel measurements [82].

Similarly, the aerodynamic loads on the vehicle empennage (horizontal and vertical tail surfaces) are computed based on the flow velocity at a reference point on these surfaces. The flow velocity again comprises an interference velocity, rigid body angular velocity, and vehicle translational velocity, this time with an empirically determined factor to model the loss of dynamic pressure at the tail surfaces due to the wake of the fuselage. The lift and drag coefficients are then obtained using look-up tables (based on wind tunnel measurements) and the incidence angles and dynamic pressure at each surface. Full mathematical details of the fuselage and empennage aerodynamics can be found in Ref. [79].

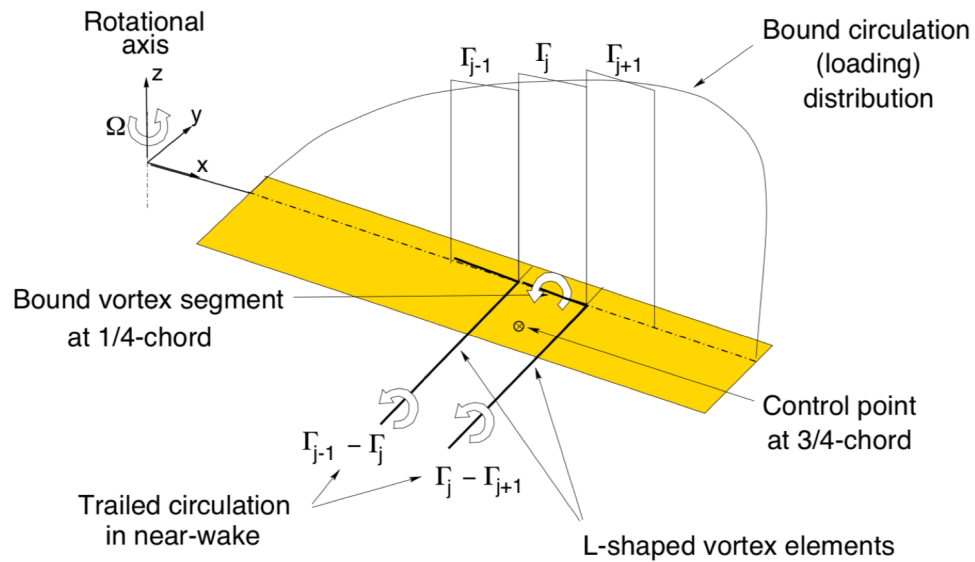


Figure 2.3: Weissinger-L lifting surface model for rotor blade

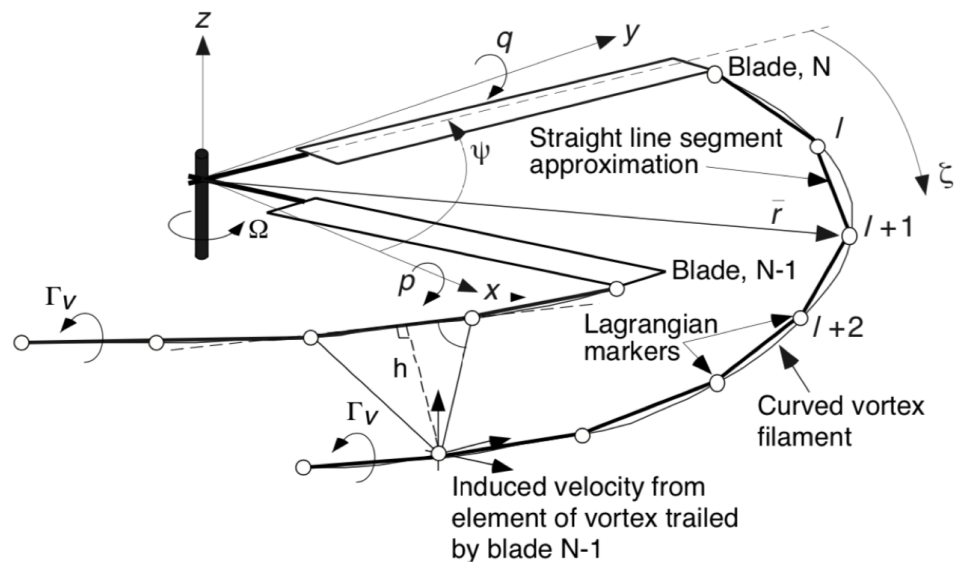


Figure 2.4: Free-vortex wake model of rotor

2.1.4.3 Tail rotor aerodynamics

The induced inflow of the tail rotor is modeled with a 1-state Pitt-Peters dynamic inflow model [83] and is assumed to be uniform over the rotor disk. The governing ODE for the tail rotor is given in Ref. [79].

The tail rotor thrust and torque are calculated in the shaft axes of the tail rotor based on the free-stream velocity and induced inflow. The relationship between these quantities is based on the closed-form solution for a lifting rotor in forward flight given in [84]. The free stream velocity at the tail rotor comprises the vehicle translational velocity, the rigid body angular velocity, and the induced velocity due to the wake of the main rotor and fuselage, obtained from look-up tables based on the wake skew angle and tilt of the tip-path plane. The tail rotor thrust equation also includes a factor to account for the blockage effects of the vertical fin.

2.1.5 Flexible Beam Dynamics

The rotor blades are modeled as flexible isotropic nonlinear Euler-Bernoulli beams with flap and lag bending and elastic torsion using a geometrically exact formulations. The rotor motions are represented by the partition of the state vector given by

$$\mathbf{y}_{\text{rotor}} = \left\{ \dot{\boldsymbol{\eta}}_1^\top \quad \boldsymbol{\eta}_1^\top \quad \dot{\boldsymbol{\eta}}_2^\top \quad \boldsymbol{\eta}_2^\top \quad \cdots \quad \dot{\boldsymbol{\eta}}_{N_m}^\top \quad \boldsymbol{\eta}_{N_m}^\top \right\}^\top \quad (2.36)$$

where $\boldsymbol{\eta}_j$ is a vector of generalized displacements for the j -th mode.

These beam models are discretized into spatial finite elements, and the underlying partial differential equations (PDEs) are reduced to ordinary differential

equations (ODEs) using a numerical implementation of the Galerkin method. Modal reduction is also applied to reduce the number of degrees of freedom while preserving the dominant blade motions of interest.

Contributions to the beam equation residuals include the internal structural loads as well as the aerodynamic, gravitational, and inertial loads. The components of the strain tensor are derived from the displacement field. The strain and material properties are used to calculate the beam stresses, which are integrated over the cross-section to give the sectional elastic forces and moments.

The external loads on the rotor blades consist of the inertial and gravitational loads, and the aerodynamic loads, or fluid forces, due to the relative motion between the blade and the air. To calculate these fluid forces, the absolute velocity of a point in the cross section of the blade is found by adding contributions of the vehicle motion, hub motion, undeformed rotating blade motion and flexible blade motion.

Velocity is transformed into deformed beam axes and broken down into components tangential and perpendicular to the airfoil as well as along the span of the blade. The velocity components lead to the sectional angle of attack used to calculate the lift and drag forces and pitching moment on the airfoil. The aerodynamic forces comprise both contributions from circulatory forces as well as non-circulatory components arising from the pitch rate and plunge acceleration of the airfoil.

2.1.6 Hub Loads

The contributions of all of the rotor forces and moments to the hub is necessary both for achieving a trimmed flight condition (in which rotor and body forces are all balanced) as well as calculating the vibratory response of the airframe or drivetrain needed for this work. The force and moment components per unit span, representing the sum of the inertial and aerodynamic loads, are calculated in the rotating undeformed blade axes. The blade loads for each individual blade are then resolved along the hub non-rotating axes and added together for the total hub loads. The hub loads are converted to the helicopter body axes to give the main rotor contribution to vehicle force and moment equilibrium equations. They are also converted to the NASTRAN axes for calculating the response of the flexible airframe at the main rotor hub.

2.1.6.1 Vibratory hub loads

For computation of the airframe vibratory response from the hub loads, it is necessary to compute the steady vibratory components of the hub loads, generally the pN_b/rev components. To do this, the time history of the hub loads over one rotor revolution is assumed to be represented by a Fourier series as

$$s_N(\psi) = a_0 + \sum_{n=1}^N a_{ns} \sin(n\psi) + \sum_{n=1}^N a_{nc} \cos(n\psi) \quad (2.37)$$

where a_0 , a_{ns} , and a_{nc} are the Fourier coefficients. For a rotor with N_b identical blades, the hub loads consists only of a steady component, represented by a_0 and

harmonics for which $n = pN_b$. In general, N is theoretically infinite, though for the purposes of this analysis, only N_b/rev and $2N_b/\text{rev}$ harmonics are considered, i.e. $4/\text{rev}$ and $8/\text{rev}$ for a 4-bladed rotor.

The Fourier coefficients are calculated from the time histories of the individual hub load components by numerically calculating the following integrals

$$a_0 = \frac{1}{2\pi} \int_0^{2\pi} f(\psi) d\psi \quad (2.38)$$

$$a_{ns} = \frac{1}{\pi} \int_0^{2\pi} f(\psi) \sin(n\psi) d\psi \quad (2.39)$$

$$a_{nc} = \frac{1}{\pi} \int_0^{2\pi} f(\psi) \cos(n\psi) d\psi \quad (2.40)$$

From the sine and cosine coefficients, the magnitude and phase the vibratory hub loads are computed as

$$f_{\text{mag}} = \sqrt{a_{ns}^2 + a_{nc}^2} \quad (2.41)$$

$$f_{\text{phs}} = \tan^{-1}(a_{nc}/a_{ns}) \quad (2.42)$$

2.1.7 Rotor-Airframe Coupling

Most often, the helicopter airframe is included in rotor analysis as a rigid body, in which the rotor hub is rigidly attached to the fuselage at a fixed position relative to the CG. However, as previously discussed, the inclusion of flexible hub motion has been shown to have an impact on the rotor loads, so it is necessary to couple the analysis of the rotor with the flexible airframe. This section will detail how the motion of the hub is incorporated into the rotor analysis as well as how the response of the hub on the airframe is calculated from the rotor hub loads.

2.1.7.1 Rotor Blade Boundary Condition

To calculate the aerodynamic and inertial loads on the rotor blades, it is necessary to know the velocity and acceleration of the blade sections. Consider a point within the cross-section of a blade. The position of the point relative to the ground, \mathbf{r}_p is given by

$$\mathbf{r}_p = \mathbf{r}_{\text{hub}} + \mathbf{r}_{\text{ea}} + \mathbf{r}_{\text{cs}} \quad (2.43)$$

where \mathbf{r}_{hub} is the position of the hub with respect to earth, \mathbf{r}_{ea} is the position of the elastic axis in the undeformed blade frame, and \mathbf{r}_{cs} is the position of the point within the cross-section with respect to the deformed elastic axis.

Helicopter rotor blades are mounted to a hub that is positioned above the vehicle center of gravity. In previous iterations of PRASADUM, the connections from body to shaft, shaft to hub, and hub to blade were assumed to be rigid. In the present analysis, the connection from the shaft to the hub and hub to blade are still considered rigid, but the flexible airframe means that the body to shaft connection is not rigid, and will therefore affect the boundary condition of the blade.

With regard to Eqns. 2.43, the addition of the flexible hub condition does not directly affect the position of either the elastic axis in the undeformed blade frame or the position of the point in the cross-section with respect to the deformed elastic axis. As such, the details of those terms will not be reproduced here, but can be found in Ref. [79]. On the other hand, \mathbf{r}_{hub} is affected by the flexible hub boundary condition.

At the most basic level, the position of the hub is given by

$$\mathbf{r}_{\text{hub}} = \{x_{\text{hub}} \quad y_{\text{hub}} \quad z_{\text{hub}} \quad \theta_{x_{\text{hub}}} \quad \theta_{y_{\text{hub}}} \quad \theta_{z_{\text{hub}}}\}^{\top} \quad (2.44)$$

where x_{hub} , y_{hub} , z_{hub} , $\theta_{x_{\text{hub}}}$, $\theta_{y_{\text{hub}}}$, $\theta_{z_{\text{hub}}}$ are the translations and rotations of the hub in the NASTRAN frame, defined in Section 2.1.2.2. The angular motion of the hub, represented by $\theta_{x_{\text{hub}}}$, $\theta_{y_{\text{hub}}}$, $\theta_{z_{\text{hub}}}$ and their time derivatives are used to compute the transformation matrices from the fixed hub frame to the deformed hub frame, \mathbf{T}_{H_2H} . The full transformation from the deformed hub frame to earth-fixed axes are then given by

$$\mathbf{T}_{GH_2} = \mathbf{T}_{GH}\mathbf{T}_{H_2H} \quad (2.45)$$

$$\dot{\mathbf{T}}_{GH_2} = \dot{\mathbf{T}}_{GH}\mathbf{T}_{H_2H} + \mathbf{T}_{GH}\dot{\mathbf{T}}_{H_2H} \quad (2.46)$$

$$\ddot{\mathbf{T}}_{GH_2} = \ddot{\mathbf{T}}_{GH}\mathbf{T}_{H_2H} + 2\dot{\mathbf{T}}_{GH}\dot{\mathbf{T}}_{H_2H} + \mathbf{T}_{GH}\ddot{\mathbf{T}}_{H_2H} \quad (2.47)$$

where \mathbf{T}_{GH} is the transformation from the hub-fixed axes to the earth-fixed axes and is based only on the rigid body motions of the airframe.

The components of the hub velocity and acceleration that are used in the calculation of the aerodynamic and inertial loads of the blade sections are also modified by the addition of elastic displacements of the hub relative to the vehicle CG. Consider that the fixed position of the hub relative to the vehicle CG is given by $\mathbf{R} = \mathbf{r}_{CG}$ and that the angular rotation of the fixed hub about the CG is given by $\boldsymbol{\Omega}$. The flexible hub contributes to the offset from the CG as

$$\mathbf{R} = \mathbf{r}_{CG} + \mathbf{r}_{hub} \quad (2.48)$$

The velocity of the hub relative to the CG is then given by

$$\dot{\mathbf{r}}_{hub} = \mathbf{v}_{hub} + \boldsymbol{\Omega} \times \mathbf{R} \quad (2.49)$$

which is added to the existing rigid body translational velocity of the hub to give the total velocity of the hub in the earth-fixed axes. Similarly, the components of the hub acceleration are given by

$$\ddot{\mathbf{r}}_{hub} = \mathbf{a}_{hub} + \dot{\boldsymbol{\Omega}} \times \mathbf{R} + \boldsymbol{\Omega} \times \dot{\mathbf{r}}_{hub} \quad (2.50)$$

Again, this contribution of the acceleration due to the motion of the hub about the CG is added to the rigid body acceleration to give the total acceleration of the hub in the earth-fixed frame. These adjusted velocity and acceleration terms for the hub are then used in the calculation of the aerodynamic and inertial loads of the blade sections.

2.1.7.2 Hub Response

Consider that the rotor is attached to a flexible structure, such as a test stand, airframe, or drivetrain. The dynamics of this structure may be expressed as a linear system of the form

$$\mathbf{M}\ddot{x}_s + \mathbf{C}\dot{x}_s + \mathbf{K}x_s = \mathbf{F}_s \quad (2.51)$$

where x_s represents the set of structural degrees of freedom, and \mathbf{M} , \mathbf{K} , and \mathbf{C} represent the mass, stiffness, and damping matrices of the structure, respectively. \mathbf{F}_s represents the forcing vector on each of the hub nodal degrees of freedom.

These matrices can be condensed to a modal representation in the usual way. In modal space, each mode is uncoupled from the other modes, and the scalar

governing equation for each mode is given by

$$\ddot{\eta}_i + 2\zeta_i\omega_{n_i}\dot{\eta}_i + \omega_{n_i}^2\eta_i = f_i \quad (2.52)$$

The modal forcing at the hub on the airframe or drivetrain is computed from the dot product of the hub forcing with the shape of the eigenvector at the hub node as

$$f_i = \sum_{j=1}^6 V_{ij}F_j \quad (2.53)$$

where the subscript i represents a specific mode and the subscript j represents the hub degree of freedom. In general, there are six hub degrees of freedom. However, the hub torque is transmitted through the drivetrain only. Therefore, the indicated sum includes only the hub torque ($j = 6$) for drivetrain coupling, and includes the three hub forces and hub pitch and roll moments ($j = 1, 2, 3, 4, 5$) for airframe coupling.

For a given modal forcing and set of modal coefficients satisfying Eqn. 2.52, the response at the hub can be reconstructed as

$$q_j = \sum_{i=1}^{N_m} V_{i,j}\eta_i \quad (2.54)$$

where N_m is the number of airframe or drivetrain modes included in the analysis. This hub motion is then used as the hub boundary condition as described in the previous section.

2.1.8 Trim

The rotorcraft trim problem, known as coupled or propulsive trim, combines the concept of general aircraft trim (as applied to fixed wing aircraft) with the con-

cept of rotor trim. For a rotor to be trimmed, the blade response in level flight should be periodic over one rotor revolution. In other words, when the forces and moments are averaged over one rotor revolution, steady-state values are achieved between cycles. For the aircraft to be trimmed, the combined forces and moments on the aircraft must be in equilibrium. In general, the forces and moments on a rotorcraft are oscillatory in nature. However, it has been shown that the overall vehicle trim state is insensitive to the vibratory loads on the aircraft, so the time-averaged forces and moments generated by the trimmed rotor with periodic response are sufficient for establishing the overall aircraft trim condition. In general, a rotorcraft trim problem is formulated for a steady coordinated helical climbing turn of constant radius. This condition is satisfied for constant flight speed, V , constant flight path angle, γ , and constant turn rate, $\dot{\psi}$. For this work, only steady level flight is considered, which is the special case of a coordinated turn in which $\gamma = 0$ and $\dot{\psi} = 0$.

2.1.8.1 Basic Trim Equations

This section lists the trim variables and associated trim equations that must be satisfied for rotorcraft trim:

- The first six trim variables are the four pilot controls of main rotor collective and lateral/longitudinal cyclic and tail rotor pedal and the fuselage pitch and roll attitudes. The associated trim equations ensure that the body forces and moments are in equilibrium. That is, the sum of all the rotor and body forces and moments about the vehicle CG is zero.

- **Dynamic inflow:** The trim variables associated with the main rotor and tail rotor inflow are

$$\mathbf{X}_\lambda = \{ \lambda_{0,\text{MR}} \quad \lambda_{1c,\text{MR}} \quad \lambda_{1s,\text{MR}} \quad \lambda_{\text{TR}} \} \quad (2.55)$$

The corresponding trim equations ensure that the inflow ratios are time-invariant when averaged over one revolution of the main rotor, as in

$$\epsilon_{\lambda_{0,\text{MR}}} = \int_0^T \dot{\lambda}_{0,\text{MR}} dt \quad (2.56)$$

$$\epsilon_{\lambda_{1c,\text{MR}}} = \int_0^T \dot{\lambda}_{1c,\text{MR}} dt \quad (2.57)$$

$$\epsilon_{\lambda_{1s,\text{MR}}} = \int_0^T \dot{\lambda}_{1s,\text{MR}} dt \quad (2.58)$$

$$\epsilon_{\lambda_{\text{TR}}} = \int_0^T \dot{\lambda}_{\text{TR}} dt \quad (2.59)$$

- **Rotor response:** The trim variables for the rotor response represent the steady and harmonic components of the rotor response when a Galerkin method with harmonic balance is used to obtain the time resolution of the rotating blade modes.

$$\mathbf{X}_{\text{rotor}} = \{ \dots \quad \eta_{j,0}^{(\text{R})} \quad \eta_{j,kc}^{(\text{R})} \quad \eta_{j,ks}^{(\text{R})} \quad \dots \} \quad (2.60)$$

where j goes from 1 to the number of blade modes, N_m , and k goes from 1 to the number of harmonics to be included in the solution, N_h . The residuals for

the steady, sine, and cosine components of the blade motions are given by

$$\epsilon_{\text{steady}} = \int_0^T \epsilon_{\text{blade 1}}(t) dt \quad (2.61)$$

$$\epsilon_{\text{cos},k} = \int_0^T \epsilon_{\text{blade 1}}(t) \cos k\Omega t dt \quad (2.62)$$

$$\epsilon_{\text{sin},k} = \int_0^T \epsilon_{\text{blade 1}}(t) \sin k\Omega t dt \quad (2.63)$$

$$(2.64)$$

2.1.8.2 Trim with Free Wake

When a free wake model is used in trim, a loose-coupling procedure is used to separately converge the aerodynamics and rotor/flight dynamics. As a first step, the vehicle is trimmed as described above using dynamic inflow, generating a starting guess for the controls, fuselage orientation, and rotor response. With this initial trim solution, the free wake solution is computed until a converged wake solution is achieved. The converged wake geometry is then used to compute the inflow over the rotor disk, and the trim solver is called again with this inflow to solve for an updated set of trim variables, excluding the dynamic inflow variables. This procedure is iterated until a converged solution is achieved for both the wake and trim variables to within a given threshold.

2.1.8.3 Trim with Flexible Hub

When the rotor is coupled to a flexible airframe or drivetrain, the trim procedure is modified to account for this coupling with the addition of trim variables associated with the flexible hub motion and the associated residuals.

The vector of trim variables for the hub motion is given by

$$\mathbf{X}_{hub} = \{\dots, \eta_{i,4c}^{(h)}, \eta_{i,4s}^{(h)}, \eta_{i,8c}^{(h)}, \eta_{i,8s}^{(h)}, \dots\} \quad (2.65)$$

representing the 4/rev and 8/rev sine and cosine components of the airframe or drivetrain response for each mode included in the analysis. In general, this set of trim variables would include all harmonics up to the total number of harmonics included in the analysis, however, since only 4/rev and 8/rev components of the vibratory hub loads are transmitted to airframe, the other coefficients are assumed to be zero and omitted from the set of trim variables.

The modal response of the hub node for the airframe or drivetrain can be calculated by

$$\eta_i^{(h)}(\psi) = \sum_{k=4,8} \left(\eta_{i,kc}^{(h)} \cos k\psi + \eta_{i,ks}^{(h)} \sin k\psi \right) \quad (2.66)$$

Recall that the modal equations of the airframe/drivetrain are given by

$$m_i \ddot{\eta}_i + c_i \dot{\eta}_i + k_i \eta_i = f_i \quad (2.67)$$

where f_i is the modal forcing given by

$$f_i = \sum_{j=1}^6 V_{ij} F_j \quad (2.68)$$

The residual for each airframe/drivetrain mode at a given time is then given by

$$\epsilon_i = m_i \ddot{\eta}_i + c_i \dot{\eta}_i + k_i \eta_i - f_i \quad (2.69)$$

The weighted residuals for the hub motion are then calculated for each mode and

each harmonic as

$$\epsilon_{i,kc} = \int_0^T \epsilon_i \cos k\Omega t \, dt \quad (2.70)$$

$$\epsilon_{i,ks}^{(h)} = \int_0^T \epsilon_i \sin k\Omega t \, dt \quad (2.71)$$

$$(2.72)$$

2.2 Engine-Airframe Coupling

The engine and airframe coupling can be taken care of in several ways. First, the engine model can be included directly into the airframe analysis. That is, the engine is included in the FE model used to generate either the airframe modes or the frequency response used in either of the rotor-airframe coupling procedures described in the previous sections. In the second approach, the engine and airframe are modeled separately, for the purposes of studying the effects of different engine mount structure parameters on the engine response. A coupling framework for coupling the airframe and engine FE models was developed and implemented utilizing frequency response functions of separate components. The general terminology for the method is frequency-based substructuring (FBS). Two versions of this methodology will be described in this section. The first is an iterative harmonic balance method. The second is a more mathematically formal method built from a framework introduced by deKlerk, Rixen, and Voormeeren [59].

2.2.1 Mathematics of Dynamical Systems

The dynamics of each component structure can be described by the structure's mass, stiffness, and damping matrices. The equations of motion of a substructure can then be written as

$$\mathbf{M}^{(s)}\ddot{\mathbf{u}}^{(s)}(t) + \mathbf{C}^{(s)}\dot{\mathbf{u}}^{(s)}(t) + \mathbf{K}^{(s)}\mathbf{u}^{(s)}(t) = \mathbf{f}^{(s)}(t) \quad (2.73)$$

where $\mathbf{M}^{(s)}$, $\mathbf{C}^{(s)}$, and $\mathbf{K}^{(s)}$ are the generalized mass, damping, and stiffness matrices of the substructure, $\mathbf{u}^{(s)}$ is the vector of the substructure degrees of freedom, and $\mathbf{f}^{(s)}$ is the vector of applied forces. In general, these forces may be externally applied, as in the case of main rotor hub loads, or may be interaction forces between two subcomponents.

In the frequency domain, the equation of motion can be expressed as

$$[-\omega^2\mathbf{M}^{(s)} + i\omega\mathbf{C}^{(s)} + \mathbf{K}^{(s)}]\mathbf{U}^{(s)}(i\omega) = \mathbf{F}^{(s)}(i\omega) \quad (2.74)$$

or, more compactly,

$$\mathbf{Z}^{(s)}(i\omega)\mathbf{U}^{(s)}(i\omega) = \mathbf{F}^{(s)}(i\omega) \quad (2.75)$$

where $\mathbf{Z}^{(s)}(i\omega)$ is the dynamic stiffness matrix or, as it's commonly referred to in literature, the displacement impedance matrix, and is defined as

$$\mathbf{Z}^{(s)}(i\omega) = [-\omega^2\mathbf{M}^{(s)} + i\omega\mathbf{C}^{(s)} + \mathbf{K}^{(s)}] \quad (2.76)$$

This equation can be solved for the nodal displacements and rewritten as

$$\mathbf{U}^{(s)} = \mathbf{Y}^{(s)}\mathbf{F}^{(s)} \quad (2.77)$$

where \mathbf{Y} is the mobility matrix or the frequency response transfer function and is given by

$$\mathbf{Y}^{(s)} = [\mathbf{Z}^{(s)}]^{-1} \quad (2.78)$$

The transfer function relates the output displacement response to an input excitation force, and in this form is complex-valued and frequency-dependent. Individual terms in the \mathbf{Y} matrix, Y_{ij} , represent the response of point i (or more generally, DOF i),

U_i , due to a unit oscillatory force (or moment) at DOF j , F_j . In other words,

$$Y_{ij} = \partial U_i / \partial F_j \quad (2.79)$$

2.2.2 Iterative Harmonic Balance Solution

Using substructuring to couple individual components together begins with identifying all of the separate structures that will be coupled, or subcomponents, and the interactions between the subcomponents. Figure 2.5 shows these elements schematically, as well as an example assembly of two subcomponents.

2.2.2.1 Subcomponents

Each subcomponent in the analysis is a dynamical system modeled with free-free boundary conditions, as shown in Fig. 2.5(a). Each subcomponent might have hundreds or even thousands of nodes included in the full finite element model, however, for the purposes of this analysis, only a small subset of “interface” nodes are important to the overall substructure assembly. Those nodes are:

1. Nodes where external forces are applied
2. Nodes connected to nodes of other subcomponents
3. Nodes where specific output is desired

There may be some overlap among these categories, but identification of the full set of $N_n^{(s)}$ interface nodes for each subcomponent is the first step in the substructuring procedure. In general, every node is assumed to have 6 degrees of freedom, 3

translational and 3 rotational. The frequency response transfer functions, $\mathbf{Y}^{(s)}$, are computed with unit magnitude sinusoidal forcing individually applied for each of the 6 N_n degrees of freedom with responses recorded at all 6 N_n degrees of freedom, for a total of 36 N_n^2 frequency response transfer functions for a single subcomponent. These 36 N_n^2 FRFs are computed for every frequency of interest in the analysis and generally consist of a magnitude and phase or are complex-valued. For the analysis in this work, the frequency response transfer functions are computed using the NASTRAN SOL 108 solution sequence, which computes direct frequency response of the full model, without any modal reduction. With this solution method, the contributions of every model degree of freedom is included in the response, even though only a subset of responses is recorded.

The forces acting on a given subcomponent may be a combination of both externally applied forces, \mathbf{F}_e , and interaction forces, \mathbf{F}_m , due to connection with other subcomponents (explained in the following section). The response of the a given node is then calculated by

$$\mathbf{U}_n(s) = \Sigma_m \mathbf{Y}_{nm}(s) \mathbf{F}_m(s) + \Sigma_e \mathbf{Y}_{ne} \mathbf{F}_e \quad (2.80)$$

Thus, interface forces and externally applied loads are treated in an identical manner in the analysis to compute the response at the key nodes using linear superposition.

2.2.2.2 Interaction elements

Interaction elements, shown in Fig. 2.5(b) refer to massless springs and/or dampers that connect two or more subcomponents together. These elements are

the counterparts of subcomponents: while the dynamical systems have input forcing and output displacement, interface elements are used to compute output forcing for input displacements.

To simplify the analysis, each interface element is assumed to connect two distinct interface nodes, each located on a different subcomponent. \mathbf{K}_m and \mathbf{C}_m are matrices that contain the spring and damper coefficients (including any cross-coupling between degrees of freedom) at an interface and are used to compute the interface loads using the resultant spring compression and/or damper velocity. These quantities are obtained from the relative response of the nodes at either end of the interface, $\mathbf{U}_n^{(A)}$ and $\mathbf{U}_n^{(B)}$. The total interface force due to both springs and dampers is given by

$$\mathbf{F}_m = (\mathbf{K}_m + i\omega\mathbf{C}_m) \left(\mathbf{U}_n^{(B)} - \mathbf{U}_n^{(A)} \right) \quad (2.81)$$

2.2.2.3 Solution procedure

A schematic representation of simple system is shown in Fig. 2.5(c). In this system, two subcomponents are connected between a pair of nodes with an interaction element. A force is applied on subcomponent A and the response is desired from subcomponent B. The known quantities for the system consist of the frequency response transfer functions of each of the subcomponents, the stiffness and damping matrices for the interaction element, and the magnitude and phase of the external forcing. The response displacements for the nodes of the subcomponents are the unknowns. In the following procedure, an implicit harmonic balance formulation is used in which the generally complex-valued forces and responses are recast using

sine and cosine components. This somewhat complicates the equations used to calculate the responses, and for the sake of brevity, the details of those calculations are omitted here.

1. Let the response of a given nodal degree of freedom be given by

$$\mathbf{U}_i(t) = \mathbf{X}_{i,c} \cos \omega t + \mathbf{X}_{i,s} \sin \omega t \quad (2.82)$$

$\mathbf{X}_{i,c}$ and $\mathbf{X}_{i,s}$ are the unknown harmonic coefficients for each nodal degree of freedom. The vector of unknowns for the full system is then given by

$$\mathbf{X} = \{\mathbf{X}_{1,c}, \mathbf{X}_{1,s}, \dots, \mathbf{X}_{N,c}, \mathbf{X}_{N,s}\} \quad (2.83)$$

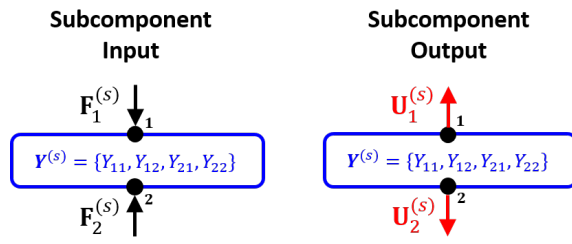
where N is the total of all interface nodes for all subcomponents. Assign an initial guess of $\mathbf{X}_0 = \mathbf{0}$.

2. Compute the interface forces \mathbf{F}_m using Eqn. 2.81 for the given set \mathbf{X} .
3. Compute the output nodal response \mathbf{X}_n using Eqn. 2.80, and extract the harmonic coefficients \mathbf{X}_{nc} and \mathbf{X}_{ns}
4. Calculate the difference between the guess value and output value of the nodal responses as

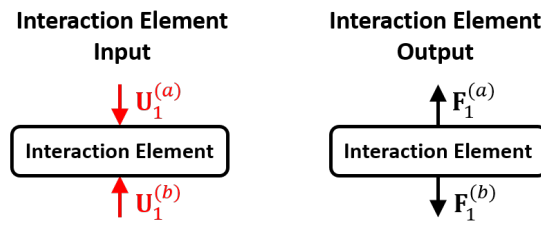
$$\epsilon = |\mathbf{X}_0 - \mathbf{X}_n| \quad (2.84)$$

If the guess values \mathbf{X}_0 are exactly equal to the calculated response coefficients \mathbf{X}_n , then the initial guess is a consistent solution. Otherwise, the initial guess is updated using Newton-Raphson iterations until the error, ϵ , reduces below a pre-determined threshold.

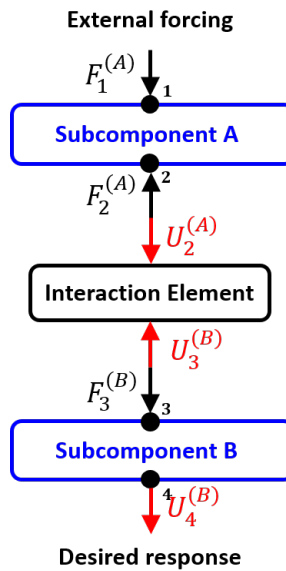
This process is repeated for each of the external forcing frequencies.



(a) Substructuring subcomponents



(b) Substructuring interaction elements



(c) Interaction of subcomponents and interaction elements

Figure 2.5: Overview of substructuring components

2.2.3 General Formulation of Frequency Based Substructuring

Although the procedure outlined in the previous section produces accurate results, the implementation of the procedure is somewhat confusing and the solution procedure can be lengthy and somewhat slow. As such, the analysis was reformulated to take advantage of a more compact mathematical structure introduced by deKlerk, Rixen, and Voormeeren [59]. The reformulation has the advantages of being much simpler to code and faster to run. In addition, it allows specifically for rigid connections between subcomponents. In the previous formulation, a rigid connection can only be approximated with a very stiff spring.

It is instructive at this point to consider a very simple system to understand the mathematical formulation. A more complicated system will be used later in this section to validate the methodology before finally applying the methodology to the airframe-engine system in the next chapter. Figure 2.6 shows a simple system consisting of two sets of three masses connected with springs, each set representing one substructure component. The two components are connected by either a rigid or flexible connection to form one coupled system. Clearly, this system could be easily modeled without the use of substructuring, but the details of the modeling are more easily understood for a simple system first.

As before, the equations of motion for each subcomponent can be written as

$$\mathbf{U}^{(s)} = \mathbf{Y}^{(s)}[\mathbf{F}^{(s)} + \mathbf{G}^{(s)}] \quad (2.85)$$

where now the applied forces have been specifically separated into externally applied forces, $\mathbf{F}^{(s)}$, and interface forces, $\mathbf{G}^{(s)}$. The procedure for the coupling of n individual substructures begins with assembling the individual substructure equations of motion in a block-diagonal format as

$$\begin{Bmatrix} \mathbf{U}^{(1)} \\ \vdots \\ \mathbf{U}^{(n)} \end{Bmatrix} = \begin{bmatrix} \mathbf{Y}^{(1)} & & \\ & \ddots & \\ & & \mathbf{Y}^{(n)} \end{bmatrix} \begin{Bmatrix} \mathbf{F}^{(1)} \\ \vdots \\ \mathbf{F}^{(n)} \end{Bmatrix} + \begin{Bmatrix} \mathbf{G}^{(1)} \\ \vdots \\ \mathbf{G}^{(n)} \end{Bmatrix} \quad (2.86)$$

$$\mathbf{U} = \mathbf{Y}[\mathbf{F} + \mathbf{G}] \quad (2.87)$$

This system of equations represents all of the substructures of the assembled system. In this system, generally the system mobility matrix \mathbf{Y} and external forces \mathbf{F} are known, while the nodal displacements \mathbf{U} and the interface forces \mathbf{G} are unknowns. The interface forces can be separated into rigid and flexible interface forces, \mathbf{G}_r and \mathbf{G}_f , respectively. The constraint equations defining the rigid and flexible interfaces between the substructures will be derived in the following sections.

2.2.3.1 Rigid Interface

At a rigid interface between substructures, two conditions must be met: interface compatibility and force equilibrium. Interface compatibility requires that displacements on either side of the connection be equal, while force equilibrium requires that the sum of the interface forces be zero. Consider a coupled system with N total degrees of freedom and N_r rigid interface degrees of freedom. The

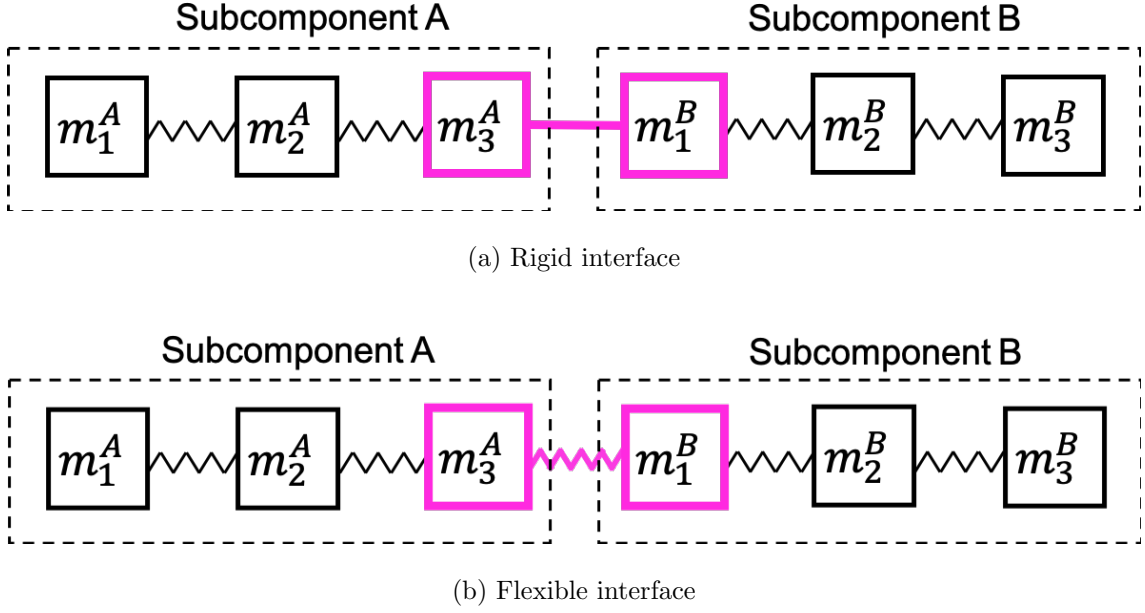


Figure 2.6: Simple spring-mass system with two substructure components

compatibility condition for a rigid interface can be expressed by

$$\mathbf{B}_r \mathbf{U} = \mathbf{0} \quad (2.88)$$

where \mathbf{B}_r matrix is a signed Boolean matrix (entries are either 0, 1, or -1) having dimensions $N_r \times N$ which expresses the condition that pairs of matching interface degrees of freedom have the same displacement. For example, in the simple mass-spring system is shown in Fig. 2.6, the vector of displacements for the system would be

$$\mathbf{U} = \{U_1^A, U_2^A, U_3^A, U_1^B, U_2^B, U_3^B\}^T \quad (2.89)$$

The condition of the rigid interface between mass 3 from subsystem A and mass 1 from subcomponent B is $U_3^A = U_1^B$ or $U_3^A - U_1^B = 0$, which can be expressed as $\mathbf{B}_r \mathbf{U} = \mathbf{0}$, where

$$\mathbf{B}_r = \begin{bmatrix} 0 & 0 & 0 & 1 & -1 & 0 & 0 & 0 \end{bmatrix} \quad (2.90)$$

The quantity $\mathbf{B}_r \mathbf{U}$ can be viewed as a vector of relative displacements for all interface degrees of freedom, which will be useful in the consideration of flexible interfaces. The force at the rigid interface between the two substructures can be written as

$$\mathbf{G}_r = -\mathbf{B}_r^T \boldsymbol{\lambda} \quad (2.91)$$

where $\boldsymbol{\lambda}$ is a vector of length N_r where each element represents the unknown magnitude of the force at each rigid interface. Returning to the sample problem, we see that

$$\mathbf{G}_r = -\mathbf{B}_r^T \boldsymbol{\lambda} = \begin{bmatrix} 0 \\ 0 \\ 0 \\ -\lambda \\ \lambda \\ 0 \\ 0 \\ 0 \end{bmatrix} \quad (2.92)$$

where the equal magnitude and opposite sign elements ensure force equilibrium at the interface.

2.2.3.2 Flexible Interface

For a coupled system with a flexible interface, as shown in Fig. 2.6(b), the condition of interface compatibility required for a rigid interface is no longer necessary, though force equilibrium must still be ensured. As before, the interface force

vector is given by

$$\mathbf{G}_f = \mathbf{B}_f^T \boldsymbol{\lambda}_f \quad (2.93)$$

where \mathbf{B}_f matrix is a signed Boolean matrix (entries are either 0, 1, or -1) having dimensions $N_f \times N$ defined identically to the \mathbf{B}_r matrix for the rigid interface. N_f in this instance is the number of flexible interface connections that exist in the system.

The previous equation 2.92 shows that force equilibrium is achieved.

Because interface compatibility is not necessary for a flexible connection, $\mathbf{B}_f \mathbf{U} \neq \mathbf{0}$. Instead, $\mathbf{B}_f \mathbf{U}$ represents the relative displacement between the interface nodes, and thus can be used with the interface stiffness to calculate the interface force magnitude of the interface forces, $\boldsymbol{\lambda}_f$, as follows

$$\boldsymbol{\lambda}_f = \mathbf{K} \mathbf{B}_f \mathbf{U} \quad (2.94)$$

Here, \mathbf{K} is the stiffness matrix representing the stiffness between subcomponents.

2.2.3.3 Rigid and flexible interfaces

For a coupled system with both rigid and flexible interfaces, the results of the previous two sections are combined. Combining equations 2.87, 2.88, 2.91, 2.93, and 2.94 the fully coupled system with a rigid and flexible connections is represented by the equations

$$\mathbf{U} = \mathbf{Y}[\mathbf{F} - \mathbf{B}_r^T \boldsymbol{\lambda}_r - \mathbf{B}_f^T \boldsymbol{\lambda}_f] \quad (2.95)$$

$$\boldsymbol{\lambda}_f = \mathbf{K} \mathbf{B}_f \mathbf{U} \quad (2.96)$$

$$\mathbf{B}_r \mathbf{U} = \mathbf{0} \quad (2.97)$$

Equation 2.95 is a system of equations representing the N total degrees of freedom in the uncoupled system. Equations 2.96 and 2.97 are the constraint equations for the N_f flexible connections and N_r rigid connections, respectively, resulting in a total of $N - N_r - N_f$ degrees of freedom for the coupled system.

2.2.3.4 Damping

In general, damping can be included in a model in a number of ways. There may be individual viscous dampers in the structure. If modal reduction is used, a modal damping factor can be specified for each of the normal modes. It is also possible that a structural damping factor is applied to the entire structure. Structural damping is given as an imaginary component to the FE model's stiffness matrix.

Any or all of these damping methods may be applied in a given structure. If damping is included in a component model when the frequency response is calculated, it will be embedded in the resulting FRF and does not need to be considered separately. The addition of damping at the interface is the only damping that needs to be accounted for. Whether a viscous damper or structural damping factor is applied at the interface, the damping force is added to the magnitude of the flexible interface force defined in Eqn. 2.96.

For a viscous damper, the damping coefficients are defined in a matrix \mathbf{C} , and the force is proportional to velocity, $\dot{\mathbf{U}}$. In the frequency domain, velocity is related to displacement by $\dot{\mathbf{U}} = i\omega\mathbf{U}$ so that the addition of damping to the flexible interface force is given by

$$\lambda_f = [\mathbf{K} + i\omega\mathbf{C}]\mathbf{B}_f\mathbf{U} \quad (2.98)$$

When structural damping is applied at the interface, a structural damping coefficient, γ , is applied as an imaginary component to modify structure's stiffness matrix such that the stiffness matrix is $(1 + i\gamma)\mathbf{K}$. This leads to the interface force being given as

$$\boldsymbol{\lambda}_f = (1 + i\gamma)\mathbf{K}\mathbf{B}_f\mathbf{U} \quad (2.99)$$

Comparing Eqns. 2.98 and 2.99, it is straightforward to see that structural damping can be replaced with an equivalent viscous damper with damping matrix given by

$$[\mathbf{C}] = \frac{\gamma}{\omega}[\mathbf{K}] \quad (2.100)$$

This is especially useful when utilizing the iterative harmonic balance solution procedure described in the previous section.

2.2.4 Validation: Simple Test Case

A simple 8-dof spring-mass-damper system is used to validate the analysis. A schematic of this system is shown in Fig. 2.7. The full system is partitioned into two substructures, as indicated by the dotted lines. Free-free frequency response transfer functions are generated for nodes 1 and 4 in substructure A and nodes 5 and 8 in substructure B. The two substructures are then connected via an interface stiffness/damping element between nodes 4 and 5. Finally, a unit harmonic force is applied at node 1 and the resulting response of node 8 is examined.

Systematic validation of the modeling was done to ensure that all interface and damping options were accounted for. Figures 2.8 and 2.9 show the comparison of the magnitude and phase of the response between the NASTRAN calculation

and the developed substructuring analysis. The following cases are present in the results:

- No damping, rigid interface
- No damping, flexible interface
- Flexible interface, viscous dampers
- Flexible interface, structural damping, $\gamma = 0.04$
- Flexible interface, viscous and structural damping, $\gamma = 0.04$

The results show complete agreement between the substructuring analysis and NAS-TRAN analysis for this example system. This agreement provides confidence in application of the substructuring methodology to a complex coupled airframe-engine model. Validation of that modeling is presented in the following chapter.

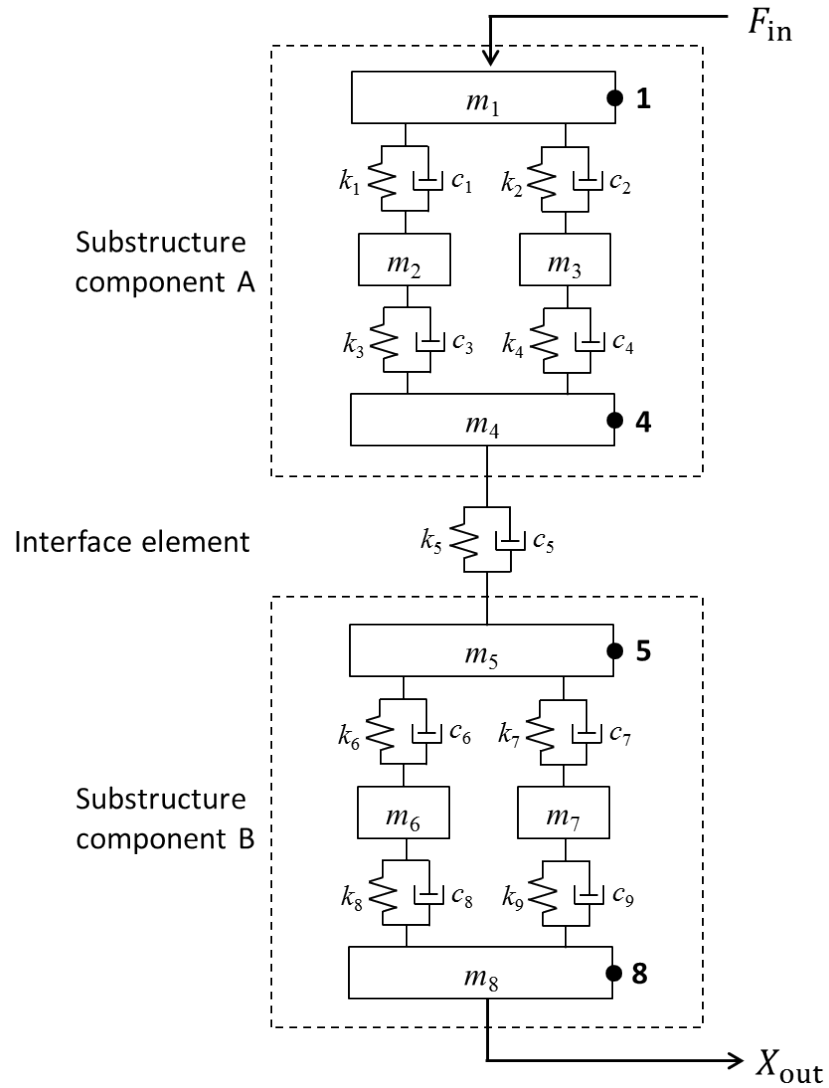
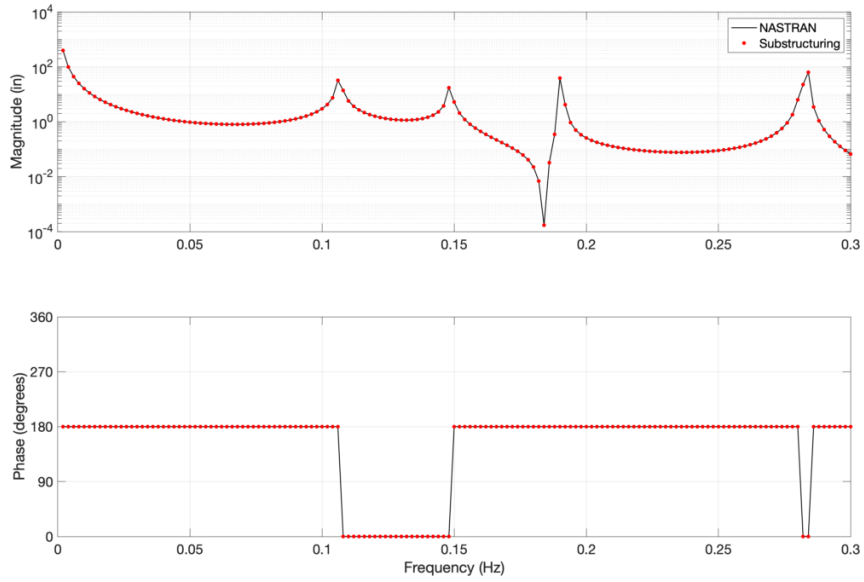


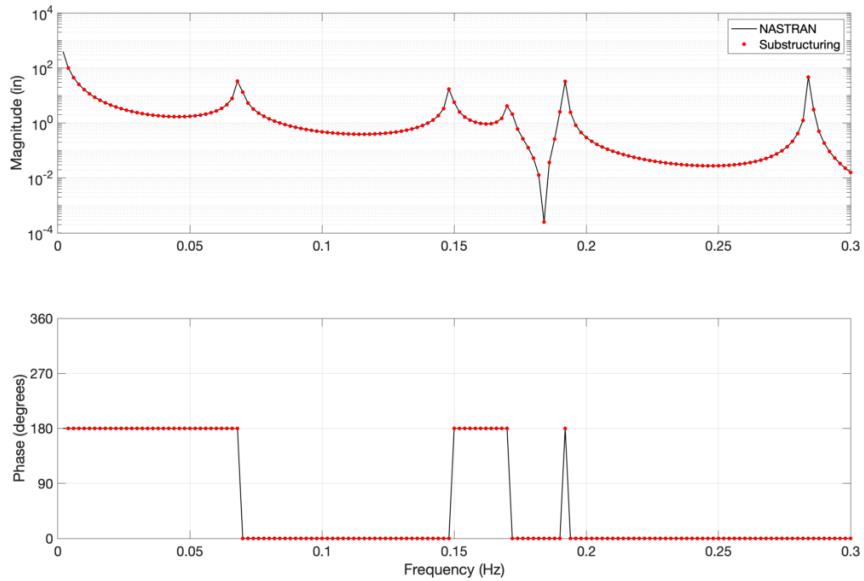
Figure 2.7: Schematic of 8-DOF mass-spring-damper system

$$m_1 = m_3 = m_7 = m_8 = 1, m_2 = m_6 = 2, m_4 = m_5 = 4$$

$$k_i = 1, c_i = 0.01, i = 1, 2, \dots, 9$$

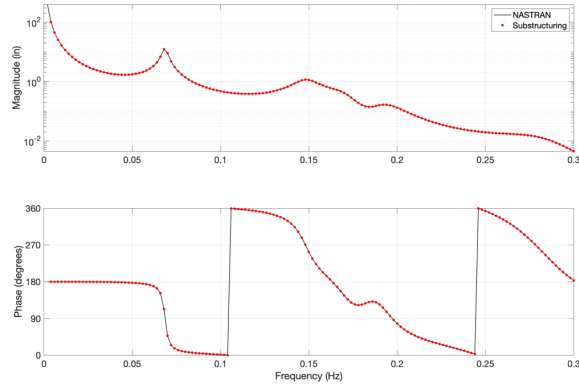


(a) Rigid interface

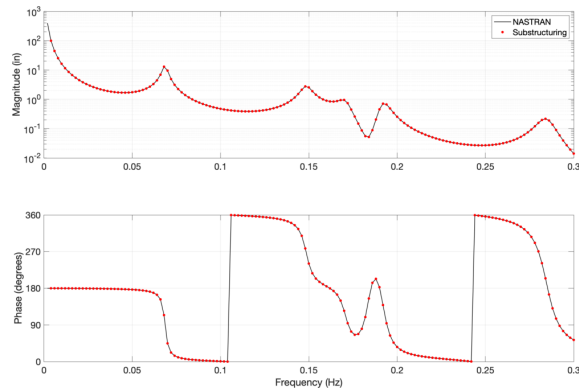


(b) Flexible interface

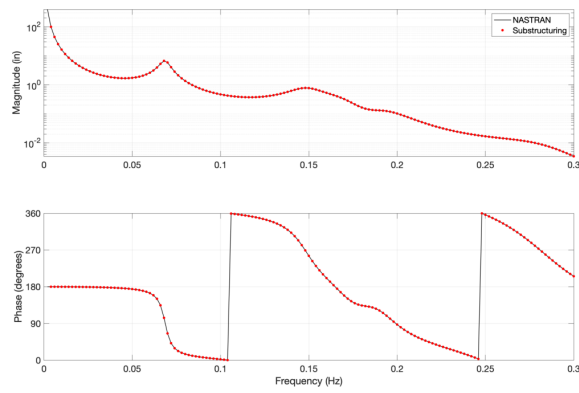
Figure 2.8: Comparison of NASTRAN and substructuring results for validation test case without any damping



(a) Viscous damping



(b) Structural damping



(c) Viscous and structural damping

Figure 2.9: Comparison of NASTRAN and substructuring results for validation test case with different damping types

3 Modeling Details

Several aspects of the modeling details are described in this chapter. First, the baseline models used in the comprehensive analysis are given, including the details of the rotor model, blade structural and aerodynamic properties, and fuselage aerodynamic and inertial properties. Next, the drivetrain model is described. Finally, the detailed finite element models of the engine and airframe models are described, along with details of the connections between the engine and airframe and validation of the coupled engine/airframe analysis.

3.1 Baseline Helicopter Rotor Model

The helicopter modeled in this analysis is based on the UH-60A Blackhawk. Significant parameters related to the main rotor geometry are given in Table 3.1. The blade structural properties are based on values given in Ref. 85. Spanwise distribution of the blade mass, m , flap bending stiffness, EI_y , lag bending stiffness, EI_z , and torsion stiffness, GJ , are given in Figs. 3.1-3.4. A fan plot representing the rotating natural frequencies as a function of RPM for this rotor is shown in Fig. 3.5 and agrees well with fan plots for this rotor generated by other comprehensive analysis codes. The frequencies for the first ten blade modes are given in

Table 3.2.

The primary airfoil for the main rotor is the SC1095. Details of the airfoil aerodynamic properties are given in Ref. [82]. Similarly, the aerodynamic properties of the fuselage and empennage are taken from Ref. [82]. Parameters used for the tail rotor modeling are given in Table 3.4.

Finally, a summary of the parameters used for the rotor and wake discretization are given in Tables 3.5 and 3.6.

3.2 Drivetrain Model

The drivetrain model used in this study is the Rotor Systems Research Aircraft (RSRA) drivetrain model [82]. The schematic of this model has been reproduced in Fig. 3.6. This model represents an equivalent single speed representation of the actual geared drivetrain. The model consists of torsional inertia and stiffness elements representing the rotating masses and flexible shafts of the complete drivetrain. The gears in the drivetrain impose constraints on the shaft speeds of each station, which modify the effective stiffness and inertia values of the model. The effective stiffness and inertia properties, K^* and J^* , are defined based on the ratio of the rotational speed of the component to that of the main rotor, $r = \Omega/\Omega_{MR}$, and are related the actual stiffness and inertia properties, K and J , as $J^* = r^2J$ and $K^* = r^2K$ [86]. The values of these parameters are shown in Tables 3.7 and 3.8.

For coupling with the rotor as described in the previous chapter, a modal representation of the drivetrain is obtained. If the rotation of the individual inertia

elements, θ^* , are the degrees of freedom of the drivetrain, the equations of motion for the model are

$$[M]\{\ddot{\theta}^*\} + [K]\{\theta^*\} = \{\tau^*\} \quad (3.1)$$

where $[M]$ is the diagonal mass matrix consisting of the inertia elements J_1^* , J_2^* , J_3^* , J_4^* , and J_5^* . The stiffness matrix, $[K]$, is given by

$$[K] = \begin{bmatrix} K_{12}^* & -K_{12}^* & 0 & 0 & 0 & 0 \\ -K_{12}^* & K_{12}^* + K_{23}^* & -K_{23}^* & 0 & 0 & 0 \\ 0 & -K_{23}^* & K_{23}^* + K_{34}^* + K_{35}^* + K_{36}^* & -K_{34}^* & -K_{35}^* & -K_{36}^* \\ 0 & 0 & -K_{34}^* & K_{34}^* & 0 & 0 \\ 0 & 0 & -K_{35}^* & 0 & K_{35}^* & 0 \\ 0 & 0 & -K_{36}^* & 0 & 0 & K_{36}^* \end{bmatrix} \quad (3.2)$$

The resulting natural frequencies for a free-free boundary condition are shown in Table 3.9 and the mode shapes are shown in Fig. 3.7. The first elastic mode consists entirely of anti-symmetric engine motion, and so does not contribute to the rotor shaft rotation. Similarly, mode 5 shows negligible hub participation and was excluded from the solution. Therefore, only modes 2-4 were included in the analysis.

3.3 Airframe Model

The airframe used in this study is a representative medium lift helicopter. The full finite element model, shown in Fig. 3.9 was developed by the airframe manufacturer, and consists of a total of 15732 nodal grid points with connections between them modeling the complete airframe structure. A superelement model [87]

for the airframe was generated by the OEM from the full finite element model and provided for this work. The superelement reduces the full airframe model down to 388 nodes. Comparisons between the full model and the superelement model show excellent agreement between the first 100 natural frequencies for the two models (up to 69.1 Hz or 16/rev).

Frequency response functions (FRFs) for the airframe finite element model were generated using NASTRAN's SOL 108 with a structural damping factor of $\gamma = 0.04$ (2%). SOL 108 computes the direct frequency response of the structure, meaning no modal reduction is used to compute the FRFs. As described in the preceding chapter, the FRFs give the response of individual nodal degrees of freedom due to individual unit sinusoidal forcing components at those same nodes. The FRFs were generated for a wide range of frequencies, including the specific 4/rev and 8/rev frequencies for the UH-60A rotor, 17.34 Hz and 34.68 Hz, respectively. The grid points used are listed in Table 3.11.

In addition to the FRFs, natural frequencies and mode shapes were calculated from the provided superelement model. The first ten natural frequency values and modes shape descriptions for the airframe are given in Table 3.12 to give some basic information about the system.

3.4 Engine Model

A NASTRAN finite element model of the turboshaft engine used in the provided airframe was provided by the engine manufacturer and is shown in Fig. 3.10.

The model consists of a total of 478 grid points. Since the model is one-dimensional (all nodes on the engine axis), off-axis points were added to the physical connection points on the engine at the rear mount plane to facilitate connection to the top of the struts connecting to the engine (fully detailed in the following section). Additionally, the model was replicated with non-repeated grid points so two identical engines could be included with the airframe model.

The translations and rotations of the rearmost node on the engine axis were used to obtain the motions of the mounting nodes on the engines. The vertical plane containing the mounting nodes was assumed to only undergo rigid-body rotations. This configuration allows for accurate modeling of the load transfer from the rear mount struts to the engine. As with the airframe, FRFs for the engine were generated using NASTRAN's direct frequency response solution (SOL 108). Unit forces and moments were applied at the fore mount point and the two off-axis rear mount points. The resulting displacements were obtained at the fore and aft mount locations on the engine axis. The engine grid points are listed in Table 3.13.

The first few natural frequencies of the engine mode are given in Table 3.14. It should be noted that the engine model is axially symmetric, so the natural frequencies occur in pairs for the two directions transverse to the engine axis.

3.5 Airframe-Engine Interface

With respect to the substructuring analysis used to couple the engine and airframe, there are five separate substructure components: the airframe, two engines,

and two engine mount torque tubes. These components are connected using a combination of rigid connections and interface stiffness and damping elements. Care was taken to ensure that the substructuring methodology matched the relevant features of the fully coupled NASTRAN model. The connections between the airframe, engine, and torque tube are shown schematically in Fig. 3.11 and the details of these connections are discussed in the following sections.

3.5.1 Fore mount

The fore end of the engine is connected to the transmission input by a torque tube. The torque tube consists of 9 beam elements with axial, bending, and torsion degrees of freedom. The mass and stiffness matrices for the torque tube were provided by the manufacturer and frequency response functions were generated for the responses to unit load excitation at each of the end nodes. The aft end of the torque tube is connected rigidly to the fore engine mount point in all 6 degrees of freedom. The fore end of the torque tube is rigidly connected to the airframe in the three translation degrees of freedom (i.e., gimbal).

3.5.2 Aft mount

The aft mount of each engine consists of three struts. As illustrated in Fig. 3.12 (a), the aft end of the engine (A1, A2) is connected by a rigid bar to the top of the struts (S1a-b, S2a-b), and the bottom of the struts are connected directly to the airframe (S1c-e, S2c-e). One outboard strut and two inboard, shown schematically

in Fig. 3.12(b) comprise the aft mount structure. The struts all lie in the same vertical plane and are symmetric between the left and right engines. The struts are represented by axially extensible linear bar elements. Based on the geometry and material properties of these elements, stiffness matrices are computed to use as the interface between the engine and airframe transfer function models.

3.5.2.1 Strut geometry and stiffness matrices

In order to properly resolve the transmission of forces between the engine and airframe, the geometry of the struts must be accounted for. The coordinates of the end points for each strut are given in Table 3.15. Note that, since the six struts are symmetric, only the right side set of struts is listed. The left side struts have identical x - and z -coordinates and opposite signed y -coordinates.

The struts lie in the vertical $y - z$ plane, so the geometry of the problem is simplified to two dimensions. The struts are modeled as axially extensible rod elements. The force transmitted along the length of a rod is given by

$$F = EA \frac{\Delta L}{L} = k_{\text{eff}} \Delta L \quad (3.3)$$

where E is the Young's modulus, A is the cross-sectional area, L is the length of the rod, and ΔL is the change in length of the rod due to compression or extension. The physical characteristics of the rod can be combined to give an effective axial stiffness, $k_{\text{eff}} = EA/L$.

Consider an axial stiffness element oriented arbitrarily in a two-dimensional plane as illustrated in Fig. 3.13. Implementation of the strut stiffness into the

substructuring methodology requires properly resolving the force along the rod into y -and z -components, F_y and F_z , resulting from the y -and z -components of the rod's change in length, Δy and Δz . The rod's change in length is

$$\Delta L = (\Delta y \cos \theta + \Delta z \sin \theta) \quad (3.4)$$

The force in rod can be decomposed into the horizontal and vertical F_y and F_z as

$$F_y = F \cos \theta = k_{eff} \Delta L \cos \theta \quad (3.5)$$

$$F_z = F \sin \theta = k_{eff} \Delta L \sin \theta \quad (3.6)$$

Combining Eqns. 3.4-3.6 gives

$$F_y = k_{eff} (\Delta y \cos^2 \theta + \Delta z \sin \theta \cos \theta) \quad (3.7)$$

$$F_z = k_{eff} (\Delta y \sin \theta \cos \theta + \Delta z \sin^2 \theta) \quad (3.8)$$

Using the relations $\sin \theta = \frac{L_z}{L}$ and $\cos \theta = \frac{L_y}{L}$ gives

$$F_y = \frac{k_{eff}}{L^2} (L_y^2 \Delta y + L_y L_z \Delta z) \quad (3.9)$$

$$F_z = \frac{k_{eff}}{L^3} (L_y L_z \Delta y + L_z^2 \Delta z) \quad (3.10)$$

These equations can be combined and rewritten in matrix form

$$\begin{bmatrix} F_y \\ F_z \end{bmatrix} = \frac{k_{eff}}{L^2} \begin{bmatrix} L_y^2 & L_y L_z \\ L_y L_z & L_z^2 \end{bmatrix} \begin{bmatrix} \Delta y \\ \Delta z \end{bmatrix} = [K] \begin{bmatrix} \Delta y \\ \Delta z \end{bmatrix} \quad (3.11)$$

with the stiffness matrix for the strut represented by

$$[K] = \frac{k_{eff}}{L^2} \begin{bmatrix} L_y^2 & L_y L_z \\ L_y L_z & L_z^2 \end{bmatrix} \quad (3.12)$$

Since the struts only allow axial extension in the $y - z$ plane, the remaining elements of a full 6×6 stiffness matrix $[K]$ are all zero.

3.6 Airframe-Engine Coupling Validation

To validate the substructuring analysis of the baseline coupled airframe-engine model, FRFs of the engine response at the mount points due to forcing at the main rotor hub were calculated and compared to the results based on the full coupled NASTRAN model. The comparisons for the transfer function magnitudes of the response of one engine mount are shown in Fig. 3.14. The substructuring approach completely captures the behavior of the NASTRAN model for various frequencies from 0 to 40 Hz, including the magnitude and phase over a range of frequencies.

Table 3.1: Main rotor properties

Property	Value
Rotor type	articulated
Number of blades	4
Radius, R	26.83 ft
Rotor speed, Ω	258 RPM
Chord, c	1.73 ft
Blade weight	256.9 lb
Shaft tilt (positive aft)	-3°
Primary airfoil	SC1095
Hinge offset	$0.0466R$
Root cutout	$0.2R$
Location of swept tip	$0.929R$
Tip sweep angle	20°
Pitch link stiffness	67900 ft-lb/rad
Solidity, σ	0.0832
Lock number, γ	6.33

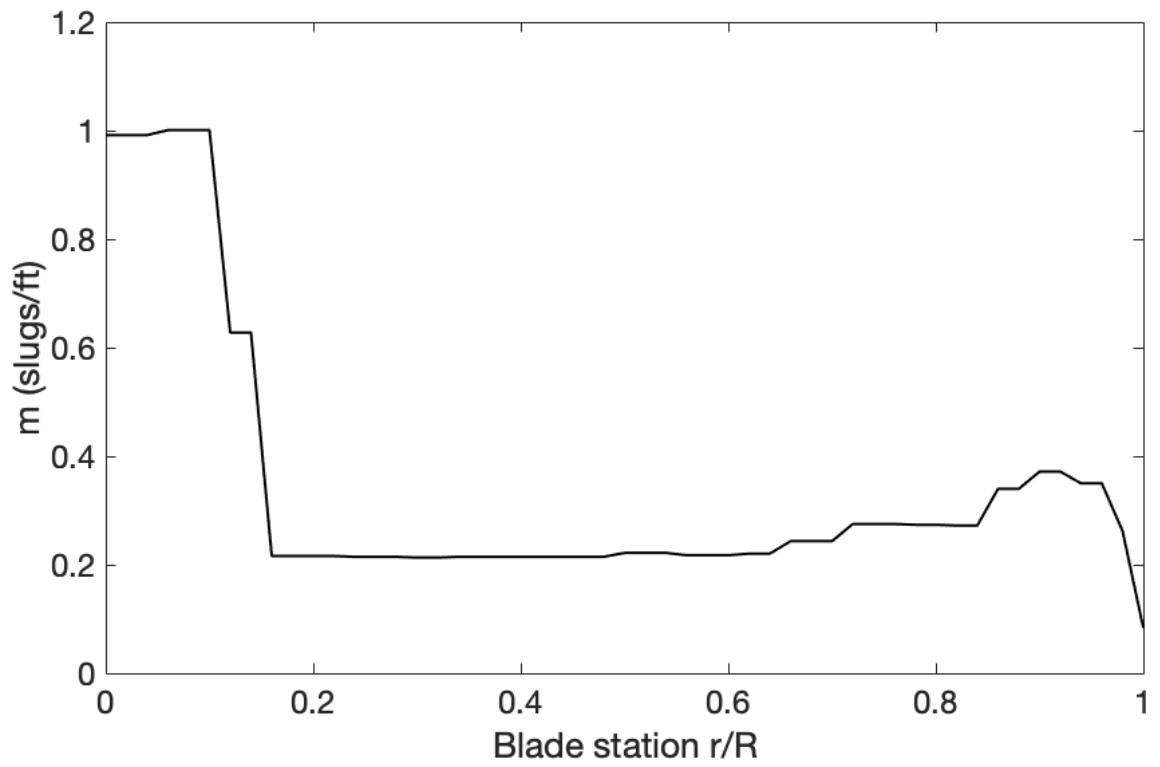


Figure 3.1: Blade mass distribution

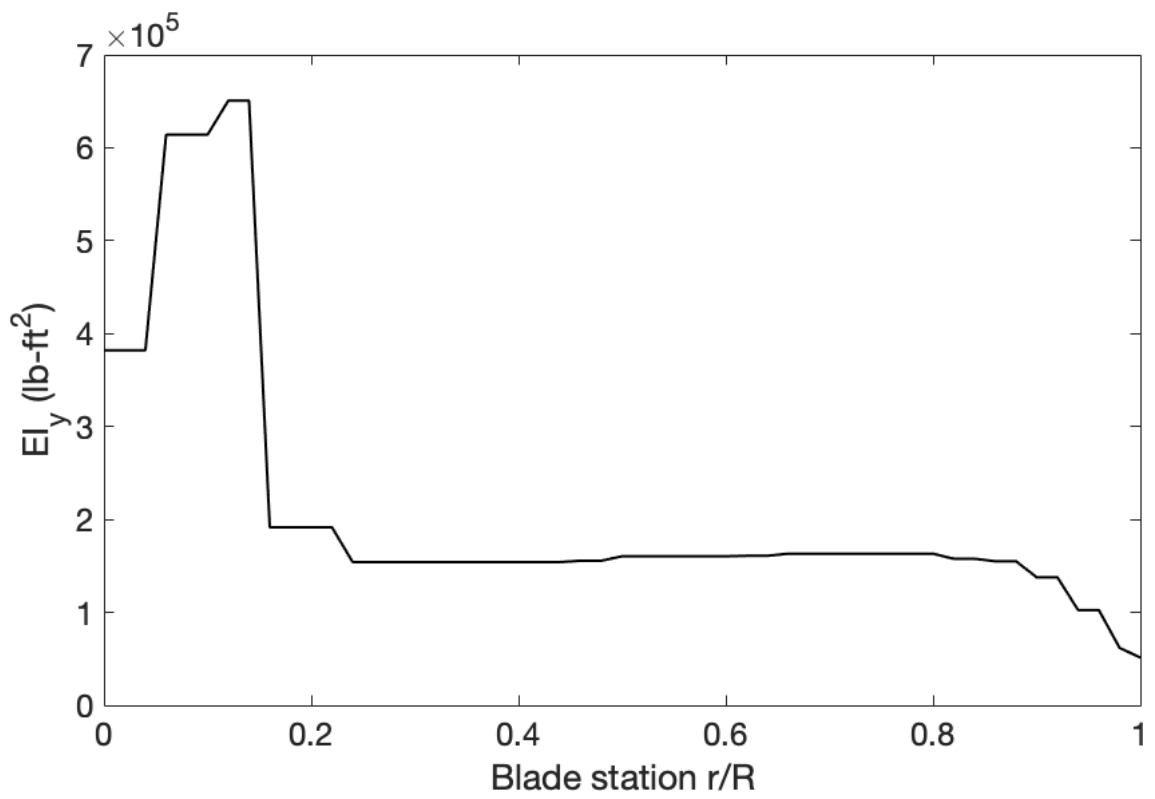


Figure 3.2: Blade flap bending distribution

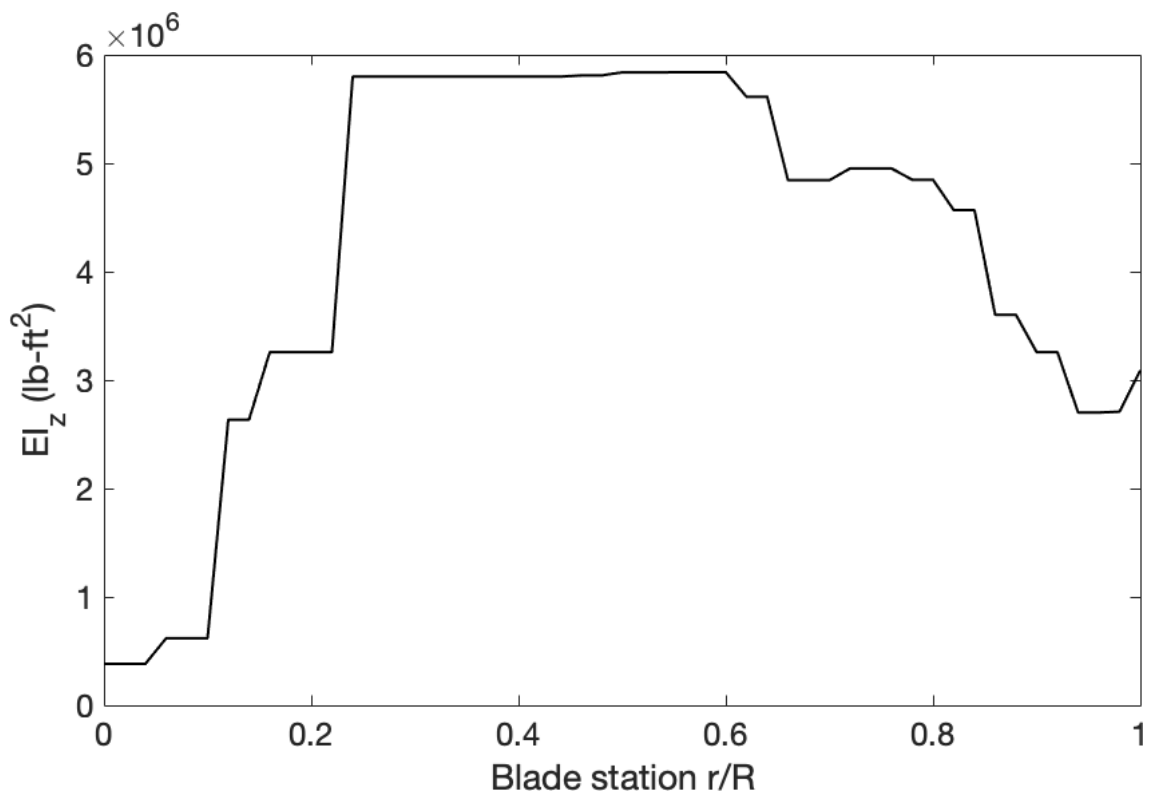


Figure 3.3: Blade lag bending distribution

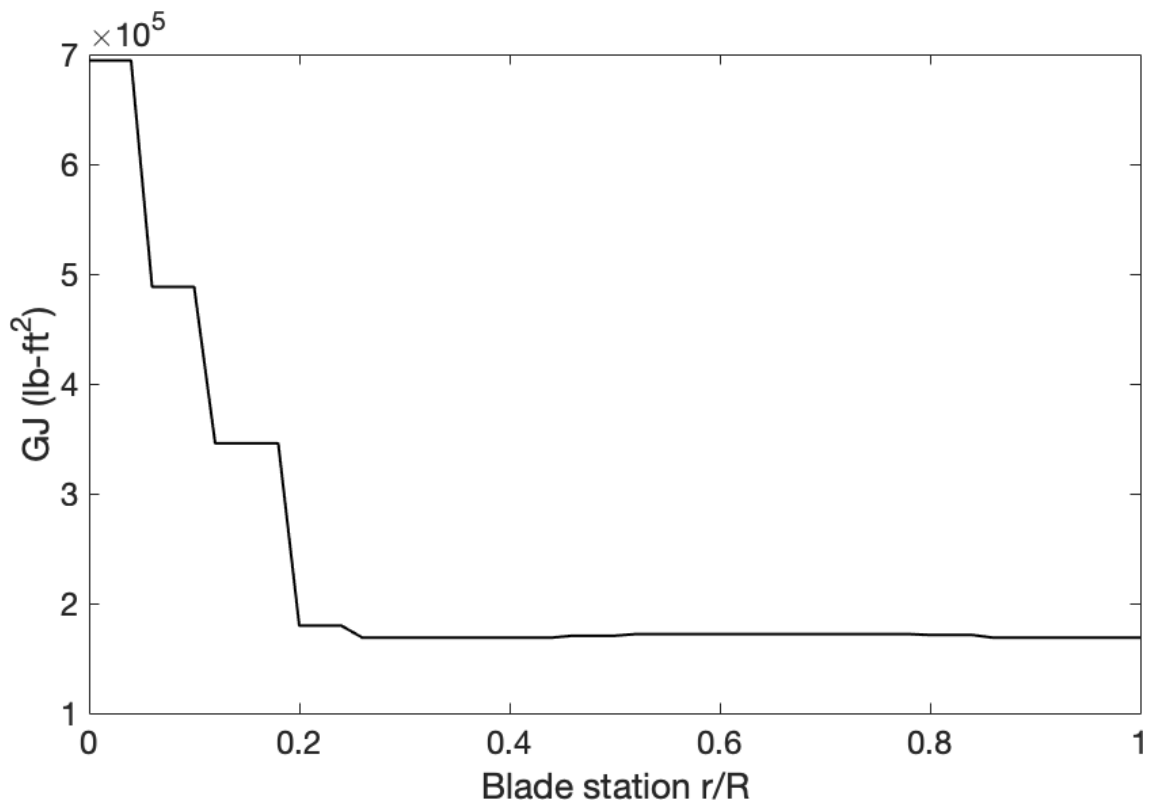


Figure 3.4: Blade torsional stiffness distribution

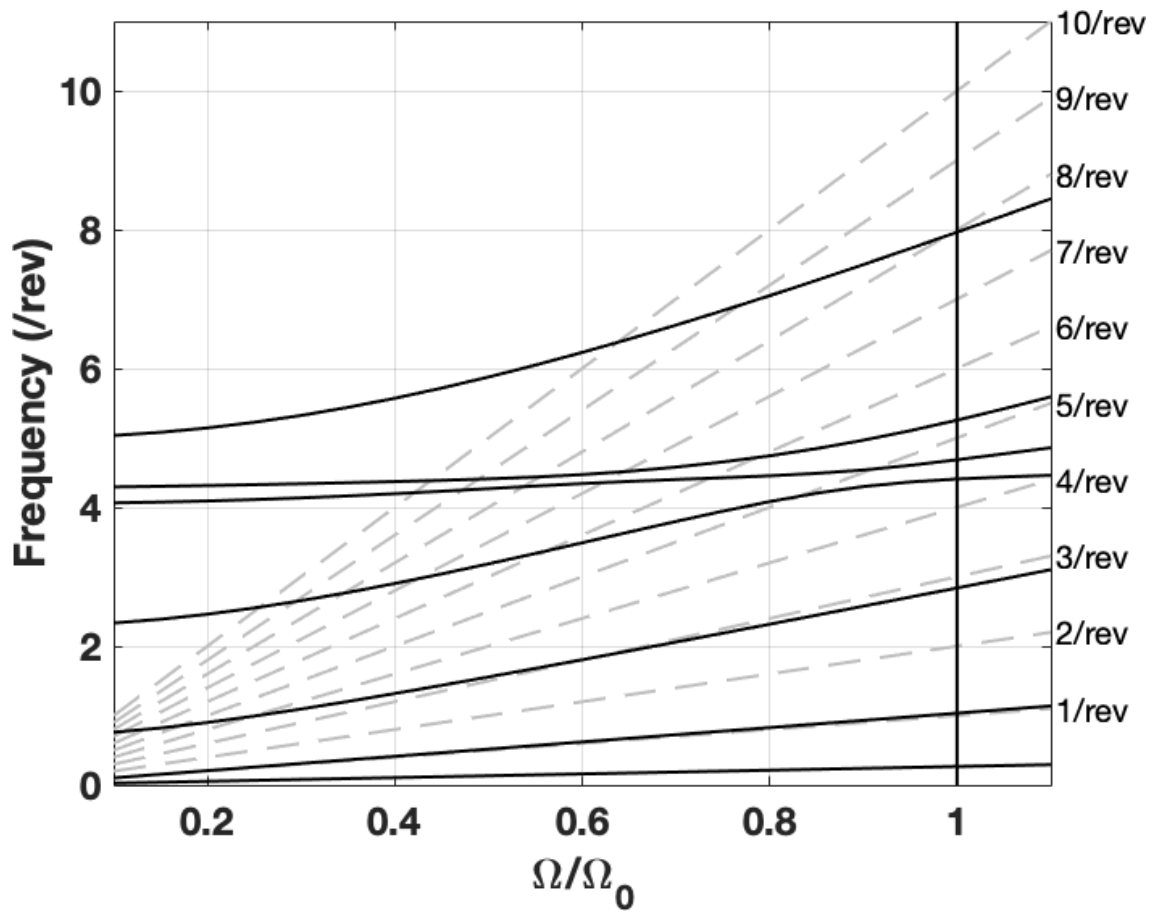


Figure 3.5: Rotor blade natural frequencies

Table 3.2: Main Rotor Blade Frequencies

Mode	Freq (/rev)
1	0.267
2	1.035
3	2.837
4	4.600
5	4.710
6	5.222
7	7.923
8	11.567
9	12.426
10	14.214

Table 3.3: Airframe properties

Property	Value
Roll inertia, I_{xx}	4658 slug-ft ²
Pitch inertia, I_{yy}	38512 slug-ft ²
Yaw inertia, I_{zz}	36796 slug-ft ²
Roll-yaw coupling inertia, I_{xz}	1882 slug-ft ²
Fuselage CG location	(360, 0, 243)
Main rotor shaft location	(341.215, 0, 300)

Table 3.4: Tail rotor geometry

Property	Value
Number of blades	4
Radius	5.5 ft
Rotation speed	124.62 rad/s
Section lift-curve slope	5.73 /rad
Chord	0.81 ft
Cant angle (from vertical)	20°

Table 3.5: Rotor blade discretization parameters

Parameter	Value
Azimuthal samples for trim	40
Flexible finite elements	20
Quadrature points per element	8
Number of blade modes	6
Blade harmonics per mode	9

Table 3.6: Wake discretization parameters

Parameter	Value
Wake discretization	10 degrees
Near wake	30 degrees
Blade bound vortex segments	40
Number of wake turns	6

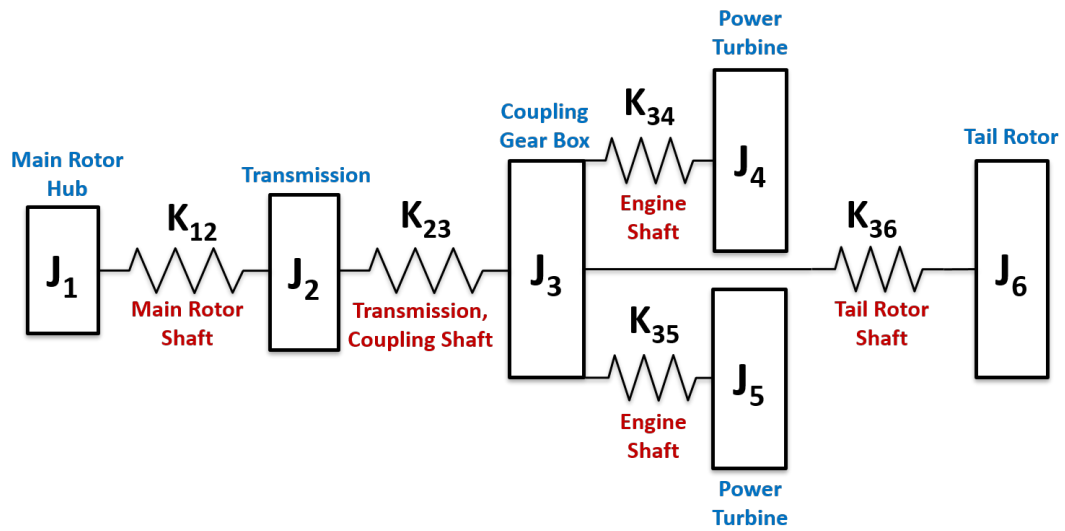


Figure 3.6: RSRA drivetrain model (Ref. [85])

Table 3.7: Inertia and stiffness properties of RSRA drivetrain model (Ref. [85])

Description	Symbol	Value
Inertia values (in-lb-sec ²)		
Main rotor hub (MR)	J_1^*	75
Transmission (TRAN)	J_2^*	909
Coupling gear box (GB)	J_3^*	1044
Power turbine (EN1)	J_4^*	6494
Power turbine (EN2)	J_5^*	6494
Tail rotor (TR)	J_6^*	4724
Stiffness values (in-lb/rad)		
Main rotor shaft	K_{12}^*	42.95E+06
Transmission, coupling shaft	K_{23}^*	1679E+06
Engine shaft	K_{34}^*	1184E+06
Engine shaft	K_{35}^*	1184E+06
Tail rotor shaft	K_{36}^*	4797E+06

Table 3.8: Speed ratios of drivetrain components

Component	RPM	Scale, r
Main rotor	258	1
Engine	20900	81
Tail rotor	1214	4.1

Table 3.9: Natural frequencies of drivetrain model with free-free boundary condition

Mode	Frequency		
	rad/s	Hz	/rev
1	427.0	68.0	15.8
2	637.7	101.5	23.6
3	751.6	119.6	27.8
4	1305.1	207.2	48.3
5	3075.9	489.5	113.5

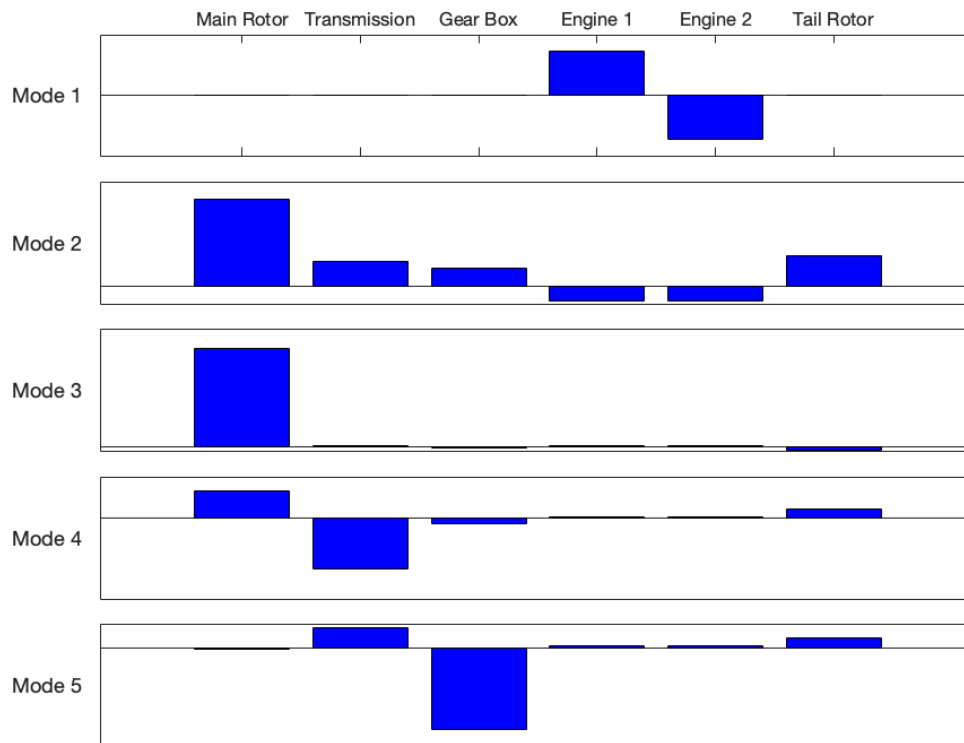


Figure 3.7: Mode shapes of drivetrain model with free-free boundary condition

Table 3.10: Natural frequencies of drivetrain model with fixed engines

Mode	Frequency		
	rad/s	Hz	/rev
1	520.2	82.8	19.3
2	749.8	119.3	27.8
3	1303.7	207.5	48.3
4	3069.4	488.5	113.7

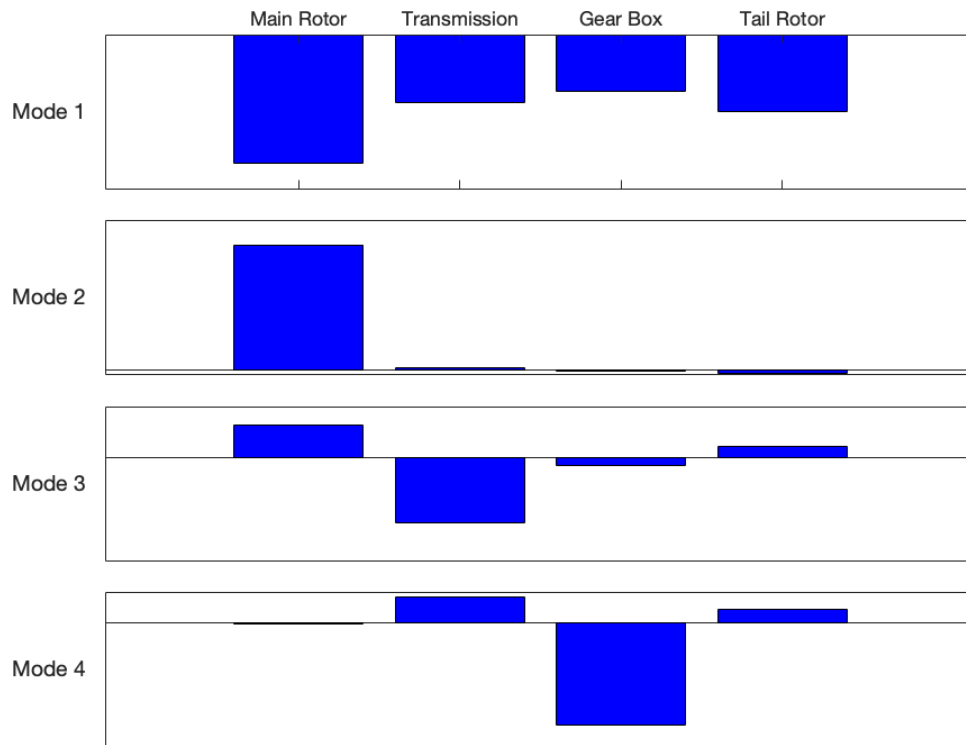


Figure 3.8: Mode shapes of drivetrain model with fixed engines

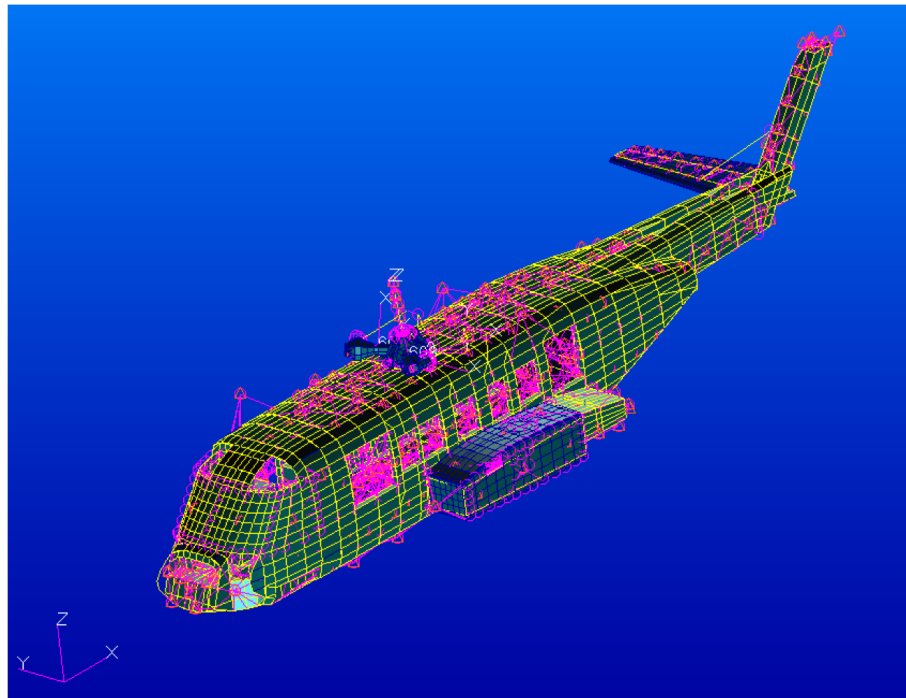


Figure 3.9: NASTRAN FE model of airframe

Table 3.11: Grid point ID numbers for NASTRAN airframe model

Grid ID	Description
690	Pilot floor (left)
698	Co-pilot floor (right)
1805	Inner strut connection (left)
1806	Middle strut connection (left)
1809	Outer strut connection (left)
1847	Outer strut connection (right)
1850	Middle strut connection (right)
1851	Inner strut connection (right)
16401	Torque tube connection (right)
17401	Torque tube connection (left)
115910	Main rotor hub
160004	Tail rotor hub

Table 3.12: Natural frequencies for baseline airframe model

Mode	Freq (/rev)	Description of mode
1-6	0.0	Rigid body modes
7	1.29	Vertical bending
8	1.50	Lateral bending
9	2.13	Tail boom torsion
10	2.28	Horizontal tail vertical bending
11	2.42	Transmission pitch
12	2.92	Fuselage torsion
13	3.07	Landing gear (symmetric)
14	3.13	Landing gear (asymmetric)
15	3.34	Horizontal tail/landing gear
16	3.41	Fuselage torsion



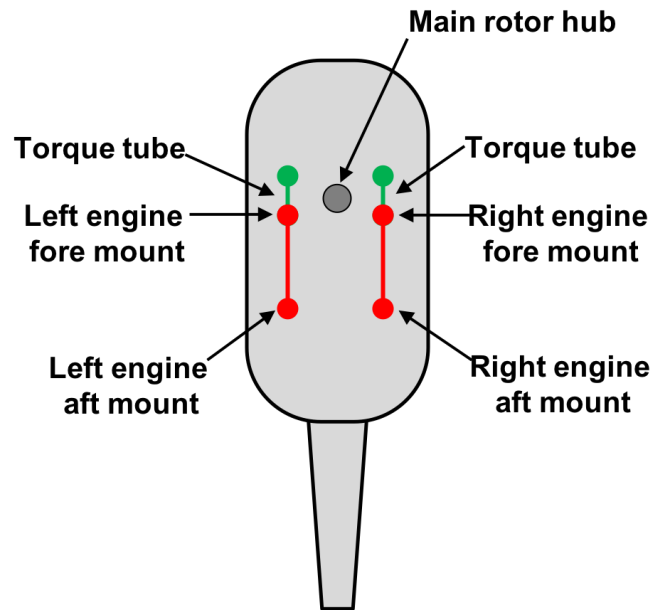
Figure 3.10: NASTRAN FE model of GE CT7-8 engine

Table 3.13: Grid point ID numbers for NASTRAN engine model

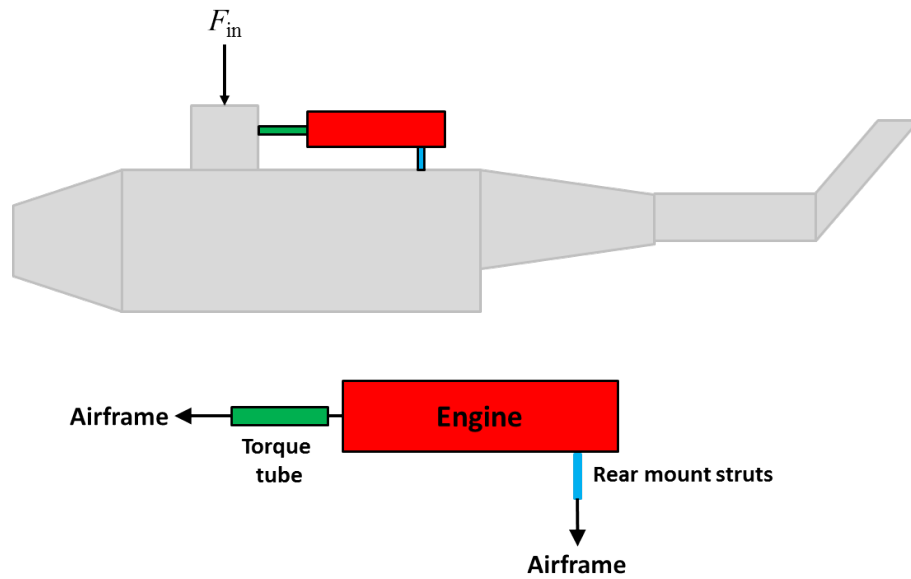
Grid ID	Description
16403	Aft off-axis inboard (right)
16405	Aft off-axis outboard (right)
17403	Aft off-axis inboard (left)
17405	Aft off-axis outboard (left)
9500044	Aft on-axis point (left)
9500048	Fore on-axis point (left)
9600044	Aft on-axis point (right)
9600048	Fore on-axis point (right)

Table 3.14: Natural frequencies for engine model

Mode	Freq (/rev)
1-6	0.0
7	15.52
8	15.52
9	18.29
10	18.29
11	22.33
12	22.33
13	27.00
14	27.00
15	33.39
16	33.39

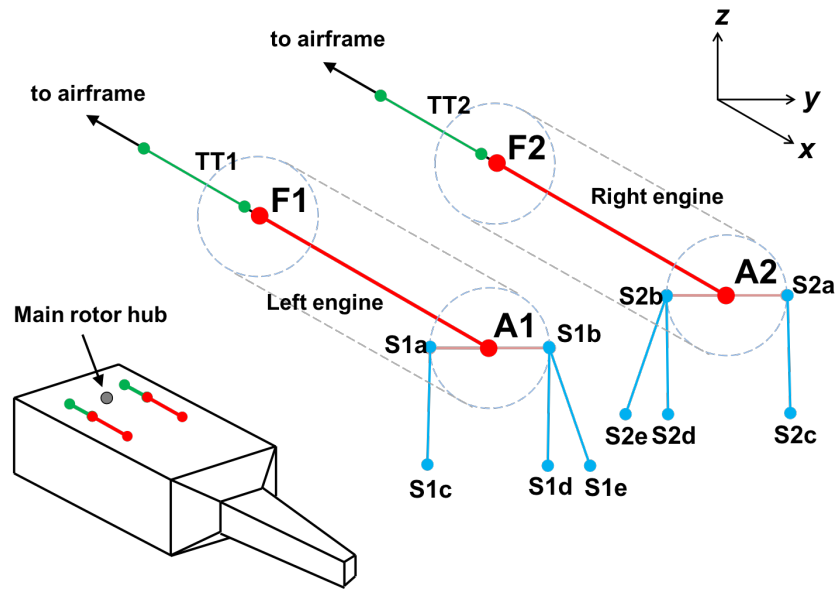


(a) Location of the four engine mount points and main rotor hub

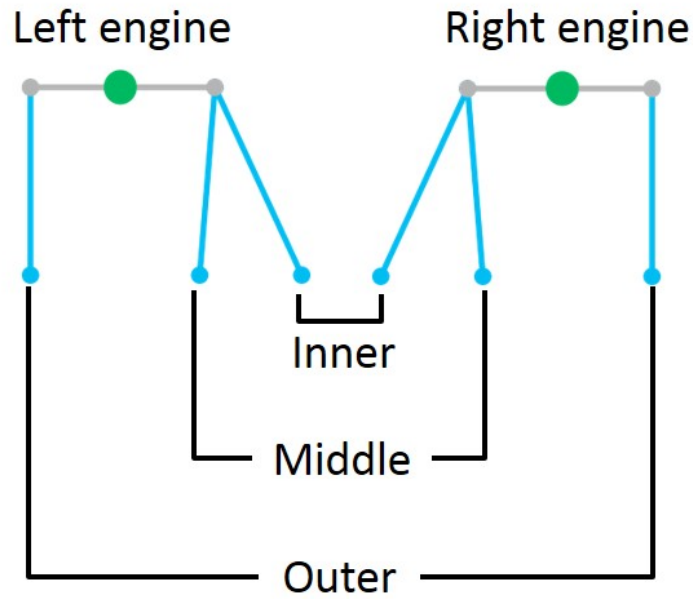


(b) Interfaces between airframe, engine, and torque tube models

Figure 3.11: Overview of Helicopter/Engine/Airframe interfaces, mounts and forcing node



(a) Engine-airframe connections (right engine)



(b) Rear engine mount struts

Figure 3.12: Schematic of engine mount structures

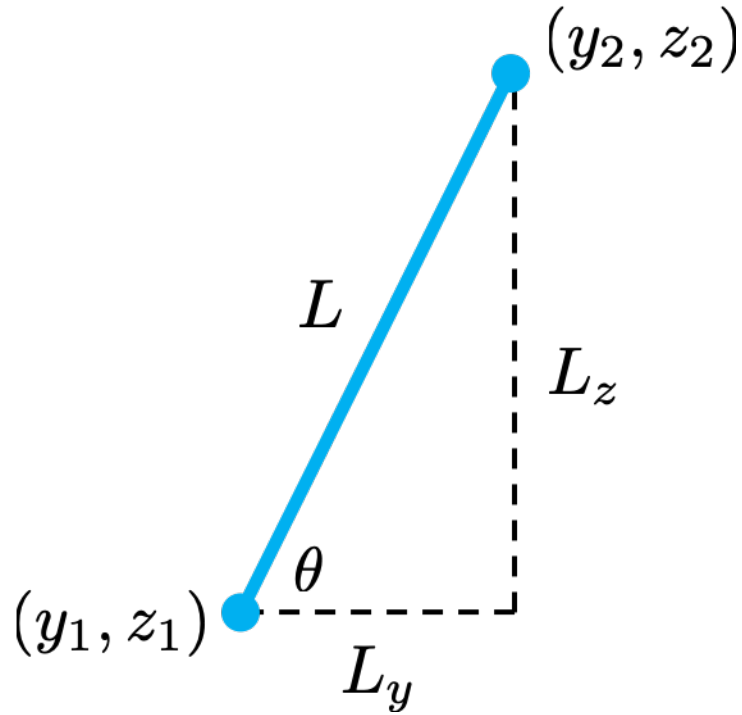
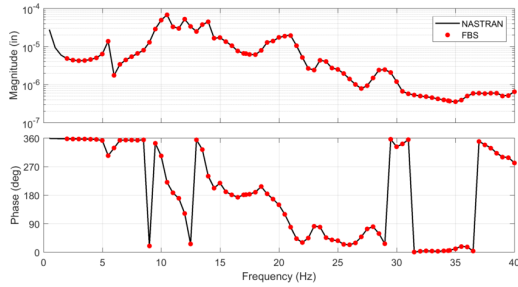


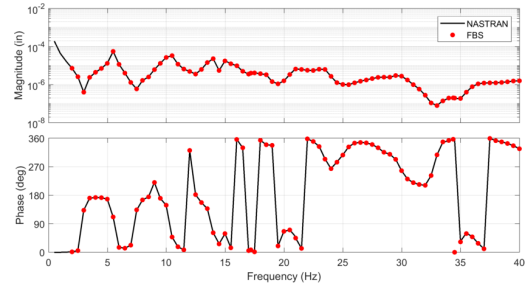
Figure 3.13: Geometry of axial stiffness element

Table 3.15: Coordinates for aft engine struts

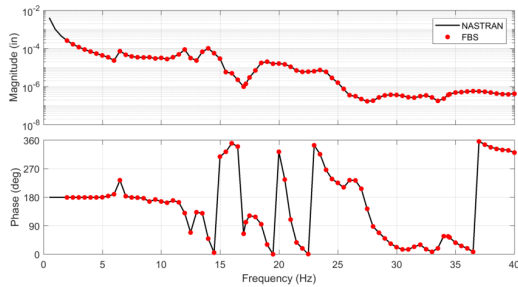
Strut position	Coordinate 1	Coordinate 2
Inner	(380.7, 16.5, 268.5)	(380.691, 20.3, 279.3)
Middle	(380.7, 21.6, 267.7)	(380.691, 20.3, 279.3)
Outer	(380.7, 37.6, 258.5)	(380.691, 39.7, 279.3)



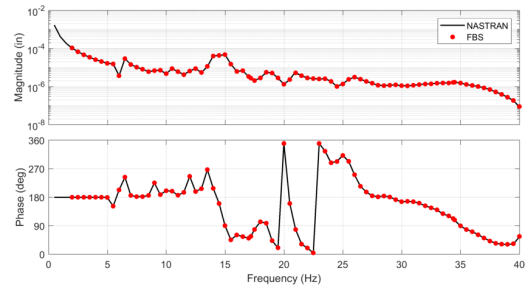
(a) F_x in, y out



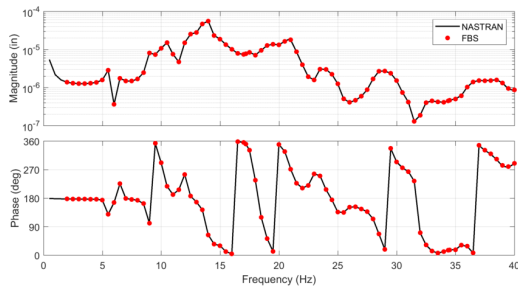
(b) F_x in, z out



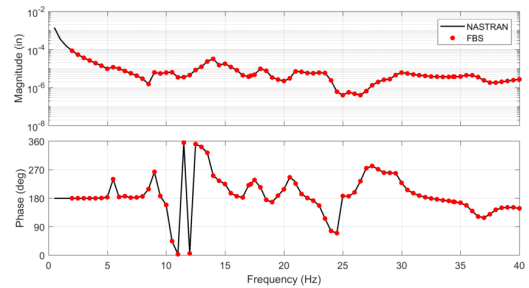
(c) F_y in, y out



(d) F_y in, z out



(e) F_z in, y out



(f) F_z in, z out

Figure 3.14: Comparison of substructuring and NASTRAN results for coupled airframe-engine model: lateral and vertical translation response magnitude and phase of left engine aft mount point to unit amplitude forcing at main rotor hub

4 Engine Mount Parametric Study

Having developed and validated the frequency-based substructuring methodology for coupling a helicopter airframe model with the associated engine model, parametric studies were conducted to determine the effects of changing stiffness and damping properties of the engine mount structures on the vibration levels experienced at different points on the engines. This chapter begins with a description of the baseline analysis results, followed by discussion of the effects of changing the stiffness and damping of the torque tube and engine struts on the baseline.

4.1 Baseline Results

Following the validation of the coupled model, 4P and 8P hub loads were applied to the coupled model frequency response functions (FRFs) and the resulting (steady-state) response magnitudes and phases at the four engine mounts were calculated to yield FRFs for the entire structure for a particular set of engine mount properties. These global FRFs represent the response (magnitude and phase) of the engine mount point along a particular direction due to unit amplitude vibratory hub loads. Tables 4.1 and 4.2 show the 4P and 8P response displacement magnitudes for each of the engine mounts due to individual hub load components.

For the results presented here, PRASADUM was used to calculate hub loads for the UH-60A rotor described previously using 6 coupled blade modes in conjunction with harmonic balance method up to 9P. Hub forces and moments were calculated at a density altitude of 5,000 ft, and steady level flight at speeds of 55, 80, 100, 125 and 150 knots, representing advance ratios of 0.128, 0.187, 0.233, 0.291 and 0.349, respectively. Figure 4.1 shows the magnitudes of the 4P and 8P hubload components for these flight conditions.

Scaling the FRF magnitudes by a single hub load amplitude (and with appropriate phase shift) for a specific flight condition provides the contribution of that hub forcing component to the total response. Vector addition of the contributions from all six hub loads yields the total engine response. Using this technique, multiple flight conditions can be analyzed using the same set of FRFs for a particular set of mount properties, further reducing the number of calculations required for the analysis. Since vibrations normal to the engine axis are thought to be more detrimental to the engine than those along the engine shaft, for this analysis, particular attention was paid to the y and z degrees of freedom, i.e., the transverse response.

Figure 4.2 shows the lateral and vertical 4P response acceleration of each engine mount point, a_y and a_z , due to each of the hub load components at 100 knots, as well as the total response from 0 to 90 degrees of rotor azimuth. Examining the breakdown of the engine response in this way allows for the identification of the hub load components that contribute dominantly to the total engine vibration. For instance, at the fore mount point of the right engine, the 4P component of the pitching moment (M_y forcing) contributes most to the lateral response (y), while

the hub roll moment (M_x forcing) is the biggest contributor to the vertical response (z). The hub forces and moments have similar magnitudes at 4P and comparable sensitivities, so the contribution of each is directly reflected in the response levels. It should be noted that although the rotor torque, M_z , is included in the hub loads and transfer functions presented here, the analysis does not include contributions from M_z , since the torque load is transmitted through the drivetrain, not directly to the airframe as the other forces and moments.

The contributions of each hub load component to the 8P response of each engine mount point are shown in Fig. 4.3, also for 100 knots flight condition. For 8P, the hub roll moment, M_x , is the primary contributor to the lateral response of each mount point and the vertical response of the aft mount points. Both hub roll and pitch moments, M_x and M_y contribute significantly to the vertical 8P response of the fore mount points.

To capture the inherent axisymmetry in the engine and quantify vibrations with a common metric, the a_y and a_z components of the acceleration were condensed into the total transverse response, $a_{yz} = \sqrt{a_y^2 + a_z^2}$ using vector addition of the accelerations along the y and z coordinate directions. Figure 4.4 shows the total 4P and 8P transverse acceleration for each of the engine mounts for each of the speed cases considered. The responses were calculated using the procedure described above, and represent baseline values for possible minimization. The following trends were noted:

1. There is an overall minimum in engine vibratory response at 80 knots ($\mu =$

0.187), though this effect is driven by reduced vibratory loading from the main rotor as the wake is swept away and tip compressibility drag is minimal.

2. There is a high degree of asymmetry between the left and right engines in this helicopter. The 4P transverse response of the left engine has similar magnitudes for the fore and aft mounts, but for the right engine, the fore and aft mounts vibrate at distinctly different amplitudes (up to 100% more vibration at the intake compared to exhaust end).
3. The transverse response of all four mounts is driven primarily by the 8P rolling moment. The peaks in response occur at 55 and 100 knots, following the trend in M_x moments shown in Fig. 4.1(a).
4. The left and right engines show comparable 8P response levels with the fore mount of each showing transverse response magnitudes close to double those of the aft mounts.
5. Overall, the peak accelerations due to 8P excitation are about one order of magnitude greater than the corresponding response levels due to 4P excitation.

This information reveals the possibility of targeting specific loads as a means of reducing the engine response. It also highlights the need for accurate vibratory loads prediction in terms of both magnitude and phase in addition to accurate structural modeling. While structural models can provide a measure of the sensitivity of certain response degrees of freedom to each hub load component, the inclusion of the phase of the response and loads can lead to either an increase or decrease in the overall

engine mount vibration.

After establishing these baseline levels of vibration, the substructuring analysis was used to perform parametric studies that would be untenable with traditional NASTRAN analysis of the fully coupled assembly. Since the 100 knots airspeed case represents a relatively high engine vibration case for both 4P and 8P, the remaining results were generated using 100 knots hub vibratory loads. Table 4.3 lists the baseline 4P and 8P transverse accelerations for the four engine mount points. The stiffness and damping values for the torque tube and struts were varied from the baseline values to identify the sensitivity of these vibration levels to each design parameter. The results of these parametric studies are discussed in the remaining sections.

4.2 Torque Tube Stiffness Sweep

A parametric sweep was conducted to determine the effect of changing the stiffness properties of the torque tube on vibratory response of the engine at the mount points. The stiffness matrix for the torque tube was scaled by a factor ranging from 0.25 to 4, corresponding to possible changes in the torque tube material and/or cross-sectional dimensions. The 2% structural damping of the baseline model was preserved for all components, and the rear mount strut properties were preserved at their baseline values. The 4P and 8P responses at both mounts of the left and right engines for various torque tube stiffnesses are shown in Fig. 4.5.

The right and left engine response sensitivity to varying torque tube stiffness

show similar trends for both 4P and 8P response. Changing the torque tube stiffness has very little effect on the 4P response of either engine at the aft mount point. Similarly, the aft mount response at 8P is relatively less sensitive to the torque tube stiffness. However, the 8P fore mount response reduces by about half for 200% torque tube stiffness. Decreasing the torque tube stiffness shows a marked increase in both 4P and 8P response at the fore mount locations. Reducing the torque tube stiffness to 50% results in a 65% increase in the 8P response and marginal increase in the 4P response.

4.3 Symmetric Strut Stiffness Sweep

A parametric sweep was performed by scaling the axial stiffness of the aft mount struts with a factor ranging from 0.25 to 4. A schematic of the six mount struts is shown in Fig. 3.12. The mount configurations for the left and right engines are symmetric, with each engine supported by two inboard struts (labeled inner and middle) and one outboard strut (labeled outer). For this study, the stiffness values of the pairs of inner, middle, and outer struts were varied independently, maintaining the symmetry between the left and right engine mounts. The effects of strut stiffness on the 4P and 8P transverse response levels are examined in the remainder of this section.

4.3.1 Uniform strut stiffness effects

For this study, the effects of collectively varying the stiffness of the struts were analyzed. Figure 4.7 shows the 4P and 8P transverse response of all four engine mount points due to changing the stiffness of all six struts.

Decreasing all strut stiffnesses uniformly results in increased 4P response at all but one mount point. At 50% strut stiffness, both mount points of the right engine and the aft mount of the left engine show significant increases in response from the baseline. In particular, the aft right mount increases from the 0.4g baseline to 1.2g. However, the fore mount of the left engine shows a decrease from the 0.25g baseline to a minimum of 0.16g. On the other hand, increasing the stiffness of all the struts beyond the baseline decreases the 4P response of the aft right mount significantly from 0.4g to 0.25g at 400% strut stiffness. The effects on the 4P response of the other mounts are less noticeable, though all but the aft left mount show a decrease with increasing stiffness.

The trends in the 8P response are the same for all four engine mount points, with differences only in magnitude. Increasing strut stiffness beyond the baseline results in decreased response, with each engine mount point achieving a reduction of about 0.3g when the strut stiffness is increased to 400% of the baseline. Alternatively, decreasing the strut stiffness results in increased transverse response, with the peak response level occurring around 35% baseline stiffness.

4.3.2 Damping effects

The effects structural damping were also examined. Structural damping factors of $\gamma = 0.04, 0.1$ and 0.2 corresponding to 2%, 5%, and 10% proportional damping, respectively, were applied for each case of the uniform stiffness sweep. Figures 4.8 and 4.9 shows the results of this study. Structural damping in the struts has a significant effect on the 4P response, particularly in the right engine aft mount, with reduction of up to 40% at 50% strut stiffness. The impact on the 8P response is less pronounced, though increased damping does result in up to 20% reduction of 8P response for 20-50% strut stiffness. However, for the increased stiffness values that achieve reduced response levels, damping has almost no effect. Therefore, damping was maintained at the baseline 2% for the remainder of the study.

4.3.3 Individual strut stiffness effects

Figures 4.10 and 4.11 show the variations in transverse 4P and 8P response, respectively, at all engine mount points due to independent variations of the inner, middle, or outboard strut stiffness. The stiffness effects of the two inboard struts (inner and middle) on the 4P response show the same trends of the uniform stiffness sweep, while the outboard strut stiffness has no effect on the 4P response. The results of varying the stiffness of both pairs of inboard struts simultaneously are not shown here, but reveal that either of the two inboard struts could be changed to achieve nearly identical results as changing both.

In contrast with the 4P results, a uniform change in the 8P response magni-

tudes at all 4 mount points appears to be driven by the stiffness of the outboard struts. Changes in the outboard strut stiffness produce the same results as changing the stiffness of all three pairs of struts. If the inner strut is stiffened or softened, the acceleration increases on the fore mounts and decreases on the aft mounts, while the middle strut mainly affects acceleration of the fore mounts of both engines, though both effects are small.

4.4 Asymmetric Strut Stiffness Sweep

The parametric studies of the previous sections were conducted while maintaining symmetry between the left and right struts. This is largely due to considerations of ease of manufacturing and installation. However, asymmetry has been noted in the response between the left and right engines, indicating that an asymmetric solution study might provide improved results. Another parametric sweep was conducted, independently scaling each of the six mounts struts with a factor ranging from 0.25 to 4.

Figures 4.12 and 4.13 show the effects on the 4P and 8P transverse response due to simultaneously varying only the left or right set of struts while keeping the other set at the baseline. Reduction of the left strut stiffness to 50% baseline results in an increased response at all four mount points though only the aft left mount increase is significant. Increasing only the left mount stiffness has negligible effects on the 4P response. Increasing the stiffness of just the right struts results in decreases in the right mount response with no effect on the left mounts. Decreasing the right

strut stiffness also leads to a significant increase in the response of the right engine, especially at the aft mount, but results in a slight decrease in the response of the left engine.

Changing the strut stiffness on one side has negligible effects on the 8P response of the engine mounts on the other side. On the other hand, the 8P response of one engine is affected by the stiffness of the struts on that side. Increases in stiffness lead to decreased response and decreases in stiffness lead to increased response, with the right strut stiffness having the greatest effect.

4.5 Minimizing Engine Response

In the previous sections, the sensitivity of the 4P and 8P engine response to changes in stiffness of one or more struts was examined, holding the other stiffness values constant at the baseline. For the large parameter space that is created by changing each of six stiffness value independently, the “best” solution might be missed by analyzing the results in this way. That is, a minimum vibration level may be achieved by a combination of stiffness values not included in the analysis. To this end, the full set of parametric sweeps for the strut stiffness scaling was examined to determine the effect of targeting different metrics for minimization. This section will examine several metrics as targets for minimization and discuss the overall changes in vibrations for each of those targets. For most of the results presented, symmetric struts were assumed, with the impact of utilizing an asymmetric design given at the end of the section. The minimization metrics that will be discussed are:

1. 4P/8P response of each of the four individual mount points
2. Average 4P/8P response of only the fore or aft mount points
3. Average 4P/8P response of only the left or right mount points
4. Maximum 4P/8P response
5. Average 4P/8P response of all mount points
6. Average combined 4P and 8P response of all mount points

4.5.1 Minimizing individual mount response

For this study, the strut stiffness factors that result in minimum transverse response for each of the individual 4 mount points were identified and are listed in Table 4.4. These results are given for both symmetric and asymmetric struts. The corresponding reductions in 4P and 8P response levels at the mount points are shown in Table 4.5. These values represent the best possible reduction in vibration for a single mount point at a single frequency for a single flight condition, i.e. these struts are point designs, with no consideration for the response at the other 3 mounts or at other excitation frequencies. These point designs may not be practical to construct. However, the maximum reduction in vibration establishes a baseline to gauge the level of compromise when the response of all 4 mounts at both 4P and 8P excitation are considered.

Fig. 4.14 shows how the responses of each mount point is affected by the choice of mount stiffness corresponding to a minimum for an individual mount stiffness. For instance, targeting a minimum 4P response at the fore left mount yields a reduction

in that response of almost 0.16g or 60%. However, the 4P response of the two aft mounts are increased by 100% or more. Similarly, targeting the minimum 8P response of the aft left mount gives at 0.27g reduction (19%) in that response while increasing the 4P response of that mount by 0.29g (120%). These results indicate that the choice of a point design may adversely affect engine vibration at other mount points, or even the same mount point but at a different excitation frequency. For a practical design, it is necessary to consider the engine mount vibration at multiple points, and multiple frequencies. The following sections systematically expand the scope of the metric involved in identifying a good strut design.

4.5.2 Minimizing maximum mount response

For this study, the strut stiffness factors that produced the minimum largest 4P or 8P response among the four mount points (maximum response) were determined. In other words, for each combination of mount stiffness values, the largest response among the 4 engine mounts was determined. From this set of response values, the smallest response was identified, and that combination of stiffness factors was used to calculate the other response levels.

Figure 4.15 shows the effects of minimizing the maximum overall 4P or 8P response on the response of all the mount points. This is similar metric to minimizing an individual mount response, although it mitigates instances where a large reduction in one mount response might be accompanied by a significant increase in the response of another mount at that frequency. When minimizing the largest 4P

response, the 4P response of all but one mount is reduced by 9-31%, while the 8P response is increased by 17-28%.

Minimizing the largest 8P response results in 5-15% reductions in 8P response. The design results in 40% reduction in the 4P response of the fore left mount, and 19-125% increase in the 4P response of the other three mounts. Therefore, the response at all points and one frequency may still result in increased response at select points at other excitation frequencies.

4.5.3 Minimizing mount response at pairs of points

This section considers the minimum average response at pairs of engine points, one frequency at a time. The four pairs considered are fore mounts for the two engines, aft mounts for the two engines, left engine mounts, and right engine mounts. As an example, minimizing the average 8P response of the fore mounts results in decreased 8P response at all mounts at 8P. However, this design also results in almost 100% increase in 4P response at the aft mount.

Minimizing the average response for the left engine mounts (and separately for the right engine) was also studied, at a single frequency. For 4P excitation, 56% reduction of the one of the targeted mounts corresponds to 67% and 245% increase on the two points not considered. For 8P excitation, the vibration at the target points can be decreased through strut design at that frequency, at the cost of more vibration at 4P at the same points. Further, targeting the 8P response of either the left or right engine mounts results in reductions in the target responses as well as

the 4P response on the opposite side, but leads to large increases in the 8P response on the opposite side and the 4P response on the same side.

These cases again illustrate the nature of the design compromise. Favorable results can indeed be achieved for the targeted locations in the elastic structure at a single frequency. However, the response for the alternate excitation frequency may increase. Further, the set of mounts *not* targeted for response reduction may exhibit more vibration at either 4P or 8P.

4.5.4 Minimizing total response

The results in the preceding section have shown that targeting the individual mounts, or pairs of mounts for vibration reduction can lead to adverse effects on the remaining mounts, and so the average of the response magnitudes from all four engine mounts were considered. Table 4.8 shows the stiffness values which produce the minimum transverse response averaged over the four mount points, for 4P excitation and 8P excitation. The last row shows the strut stiffness ratios (relative to the baseline) obtained when the amplitude of average 4P and average 8P vibration is used as the metric for reduction. Both symmetric and asymmetric strut designs (with respect to left vs. right engine) are considered in this study. The results for symmetric strut design are considered first, and then the results for asymmetric strut design are discussed.

4.5.5 Symmetric strut design

Figure 4.18 shows the resulting change from the baseline response for each mount when the symmetric stiffness values are used. When targeting the average 4P response, the fore left mount response is increased by 30%, and all other mounts exhibit vibration reduction of 24-43%. For this design (first row of Table 4.8), the 8P response decreases marginally (2-3.5%) at the fore mounts and increases marginally (2-5%) at the aft mounts.

When targeting the average 8P response (second row of Table 4.8), all four mounts show a decrease of 9-16% at 8P. For 4P excitation, the response increases by as much as 125% for three of the mounts. The 4P response of the fore left mount exhibits qualitatively opposite behavior to the other three mount response levels, i.e., while the other three mounts exhibit more 4P vibration, the fore left mount exhibits reduction of amplitude (in this case, by 40%).

Targeting only the 4P or 8P response (averaged over all 4 mount points) could lead to adverse effects on the response for the frequency not targeted. Therefore, it may be necessary to target the average response at all mounts *and* at both frequencies. The vibration reductions obtained by tuning the strut stiffnesses for this criterion are shown in Fig. 4.18(c).

Vibration reductions at all mount points and both frequencies are obtained, except the fore mount of the left engine. In particular, the 4P response of the fore left mount increases by 7%, while the other three decrease by 11-39%. The 8P response is reduced by 7-18% at all mounts. This behavior may result from the

asymmetry of the airframe structure; a few airframe mode shapes (in the vicinity of 4P) exhibiting opposite signs for the eigenvector displacement components at the fore mount of the left engine could drive the opposite qualitative behavior for that one mount. This result indicates that the airframe structure may require local redesign to extract additional vibration reduction at the engine mounts. However, such an endeavor must be weighed against other constraints for airframe design such as weight and vibration reduction at other stations.

4.5.6 Asymmetric strut design

When the strut stiffness is allowed to vary between the left and right engine mounts, slightly different vibration trends are noted. The outboard strut design is unchanged when asymmetry is allowed. Further, only the left engine struts change for minimum 4P, and only the right struts change for targeting 8P response. When minimizing the average combined 4P and 8P response (Table 4.8), all 6 struts should be stiffened to 400% baseline for a symmetric design. With symmetric struts, a reduction of 1.18g in combined 4P and 8P response magnitude is achieved. If asymmetry is allowed, softening the left inner strut to 50% provides a marginal benefit: the total reduction increases to 1.22g.

4.6 Summary

The results of the stiffness sweep study show that overall reduction in both 4P and 8P response is possible if the stiffness of all struts is increased above the baseline.

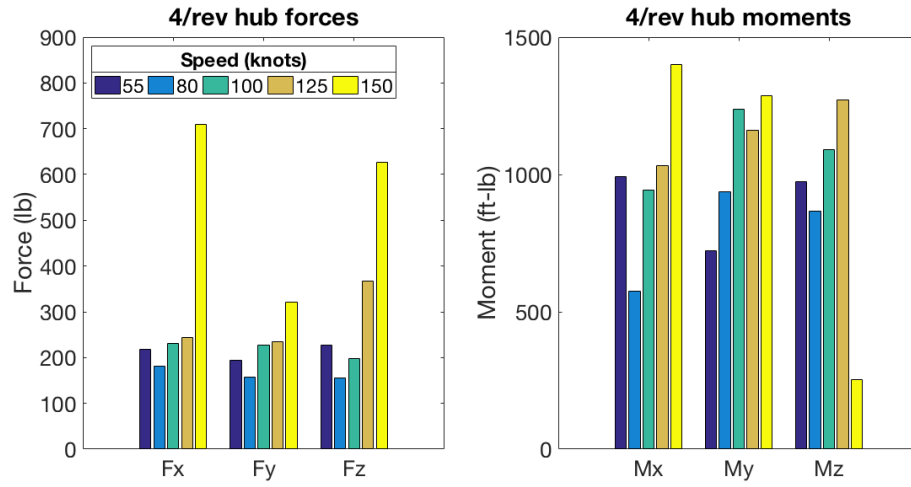
Both the symmetric and asymmetric stiffness sweep results indicate that the largest cumulative percent reduction in the 4P and 8P response of all four mounts can be achieved if all six struts have their stiffness increased to 400% of the baseline.

Further, results of the study of torque tube stiffness indicate that reductions in both 4P and 8P response at the fore mounts is possible if the torque tube stiffness is increased to 200% of its baseline. A final symmetric strut stiffness sweep was conducted with 200% torque tube stiffness. The goal of this sweep was to determine whether changing the torque tube design results in a different strut design, providing a qualitative measure of the cross-coupling between fore mount and aft mount design. It was found that increasing the stiffness of all six struts to 400% of the baseline gives the best improvement in 4P and 8P vibration reduction. In both cases it was found that the large reductions were retained when increasing the strut stiffness to only 200% and only the aft right mount response was further improved by the 400% stiffness, achieving an additional 10% reduction. Trade studies of vibration reduction and the possible weight/cost penalties of increasing the strut stiffness are necessary to determine whether additional stiffening is advantageous on the whole.

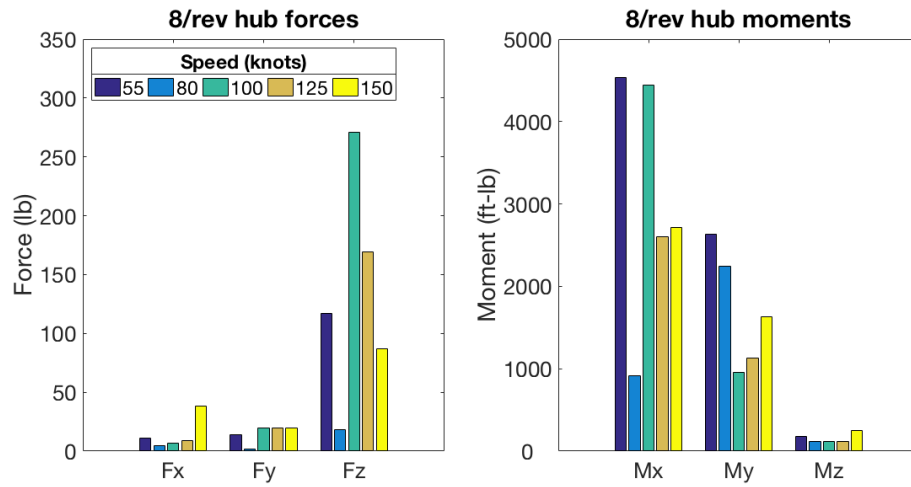
Based on these findings, the transverse response at the four engine mount points were calculated for two improved designs. The first improved design is when only the rear mount struts are stiffened to 200%. The second improved design is when both the struts and torque tube are stiffened to 200%. 4P and 8P hub loads were applied at the main rotor hub based on the four level cruise flight speeds previously considered: 55, 80, 100, 125 and 150 knots. Figures 4.19(a) and 4.19(b) show the 4P and 8P response levels for the baseline and the two improved designs.

This speed sweep demonstrates the cumulative effects of increasing the stiffness of both the fore mount torque tube and aft mount struts. Overall, reductions in the 4P and 8P transverse response are achieved at all four mounts and flight conditions with one exception. The 4P response of the fore left mount shows increases of 5-13% when only the strut stiffness is increased. This detrimental effect is mitigated to 0.3-8% increase for the second improved design. At all other mounts, enormous reductions of 11-58% are achieved at both 4P and 8P.

Specifically, the stiffer aft mounts reduce the 4P response by 30% for the aft right mount and 10-20% for the fore right and aft left mounts. The effect of stiffer struts on reduction of 8P response at all mounts is less significant, but still noticeable (5-8%). A stiffer torque tube results in significant reduction in the 8P response (up to 50%), while having a small benefit on the 4P response at the fore mount points for both engines.



(a) 4P hub load components



(b) 8P hub load components

Figure 4.1: Hub load amplitudes ($C_W/\sigma=0.082$)

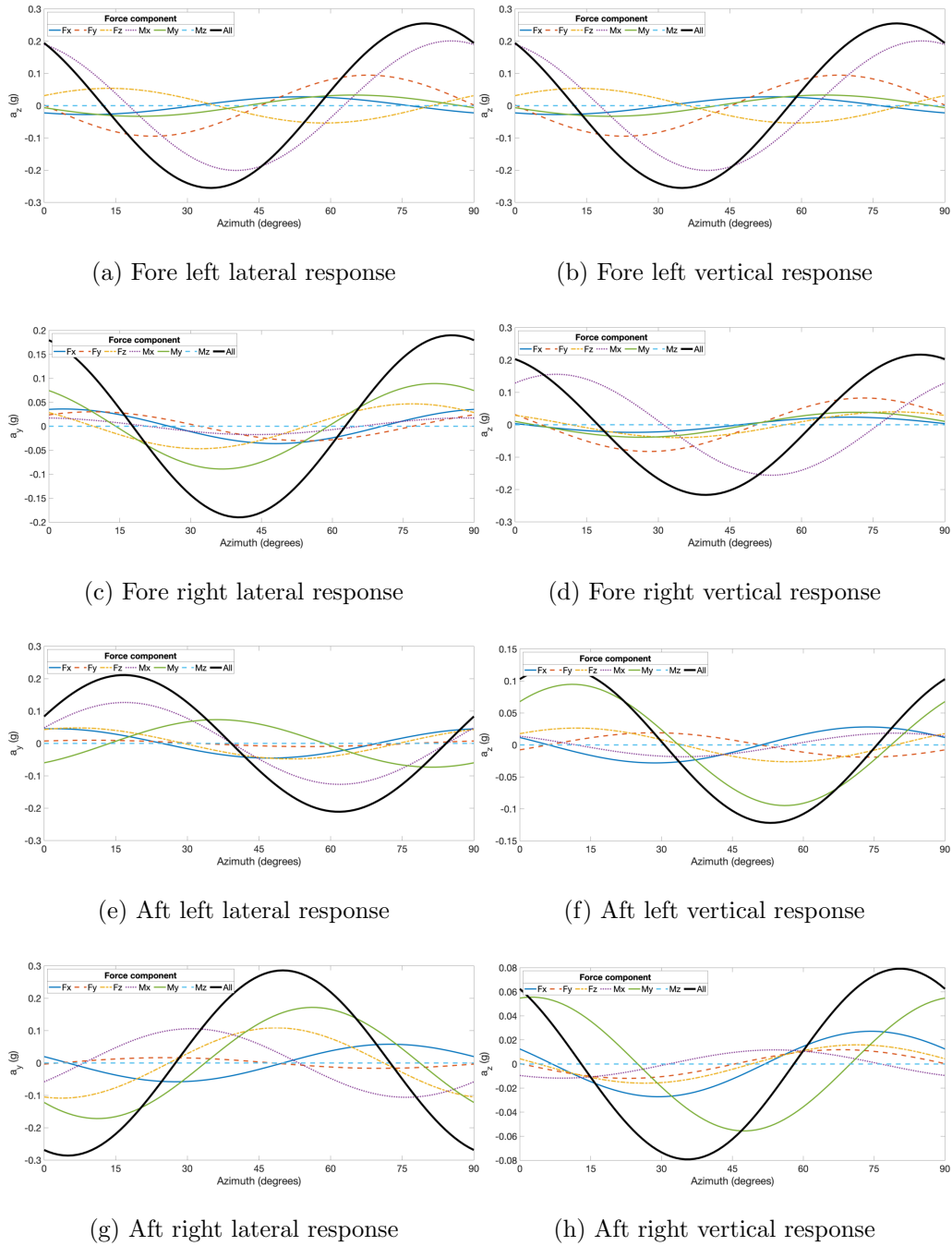
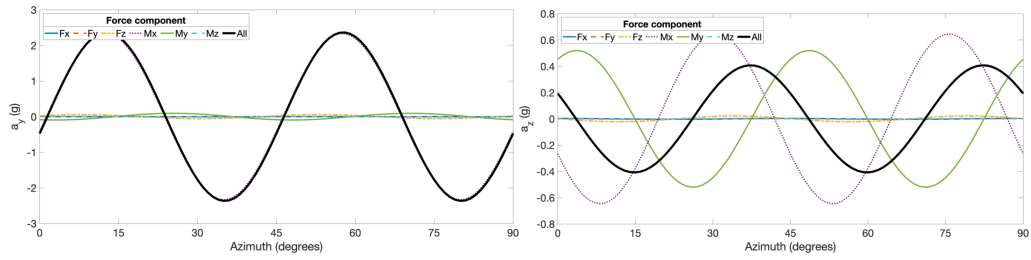
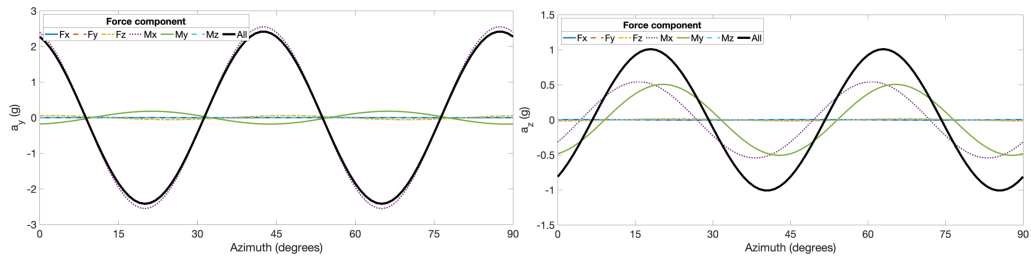


Figure 4.2: Breakdown of 4P engine mount response from individual hub load component contributions ($C_W/\sigma=0.082$, $\mu=0.233$)



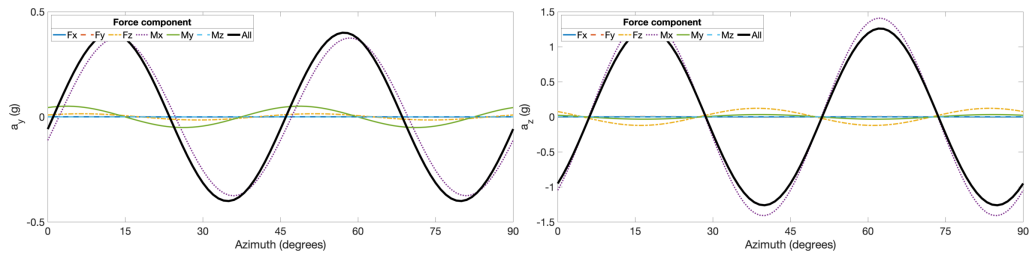
(a) Fore left lateral response

(b) Fore left vertical response



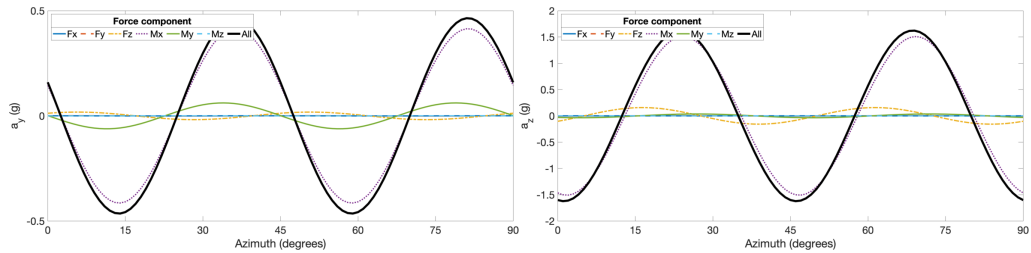
(c) Fore right lateral response

(d) Fore right vertical response



(e) Aft left lateral response

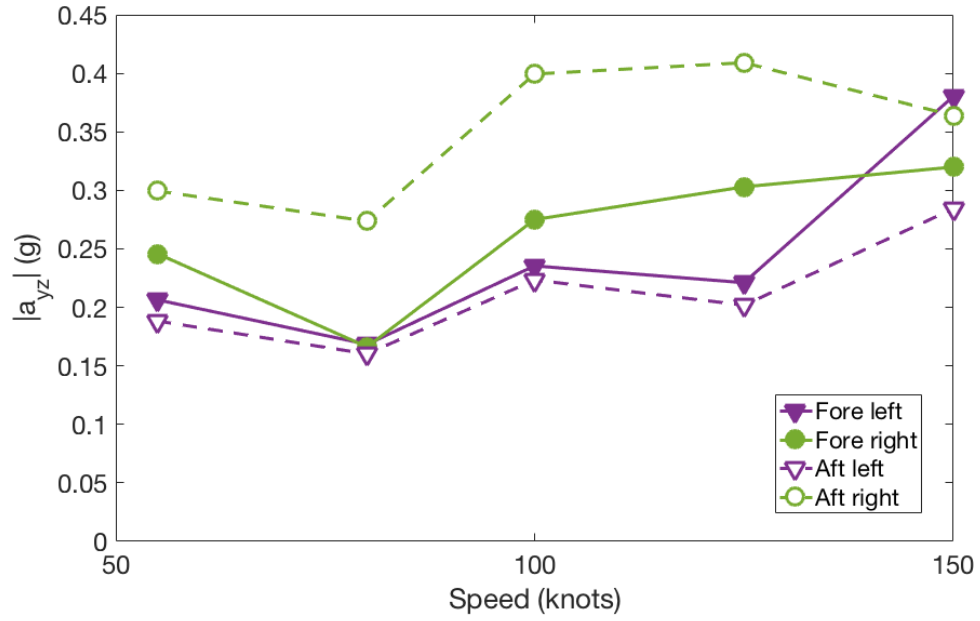
(f) Aft left vertical response



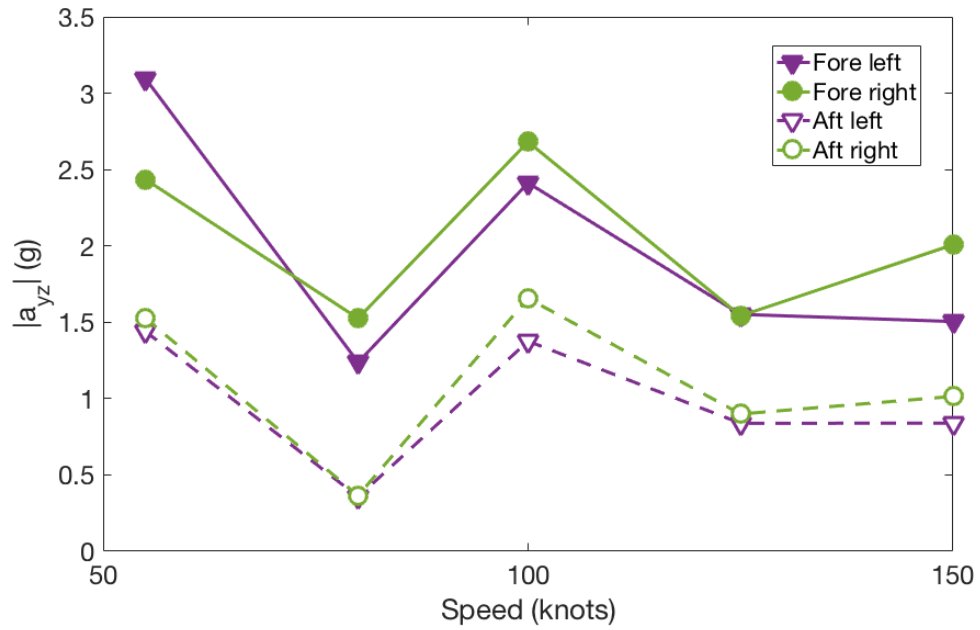
(g) Aft right lateral response

(h) Aft right vertical response

Figure 4.3: Breakdown of 8P engine mount response from individual hub load component contributions ($C_W/\sigma=0.082$, $\mu=0.233$)

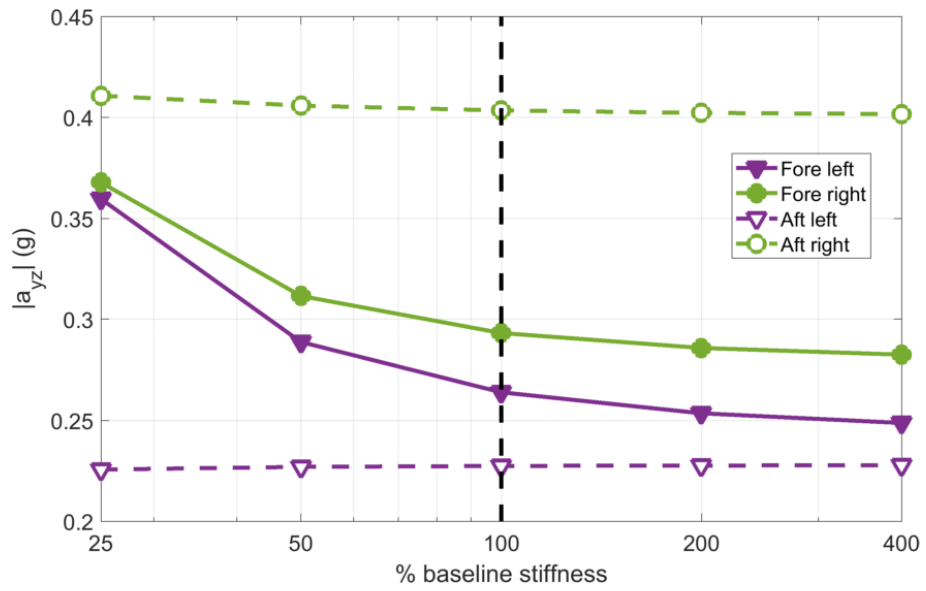


(a) Total 4P transverse response at various flight speeds

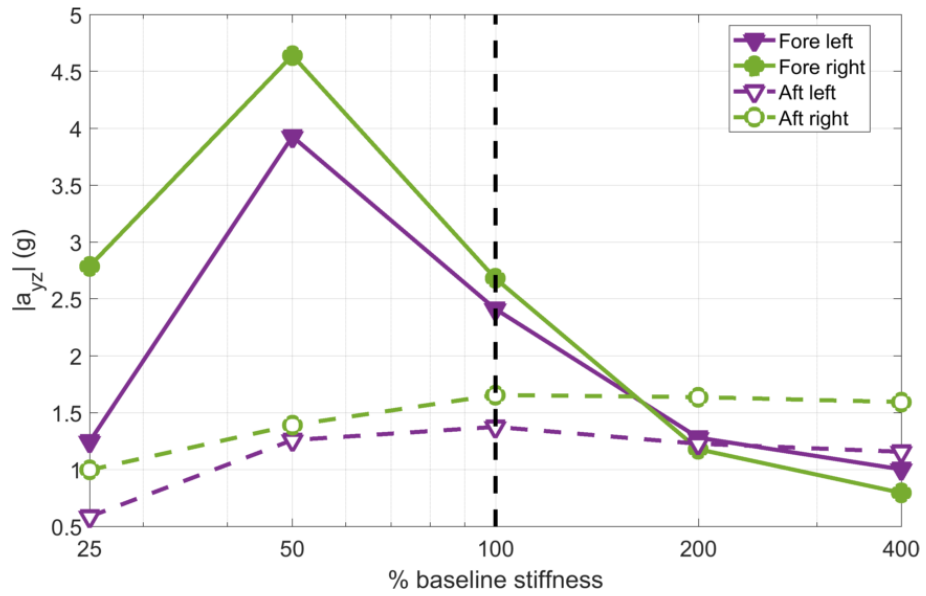


(b) Total 8P transverse response at various flight speeds

Figure 4.4: Total transverse response with forward speed ($C_W/\sigma=0.082$)



(a) 4P response



(b) 8P response

Figure 4.5: 4P transverse response of engine mount points for various torque tube stiffnesses

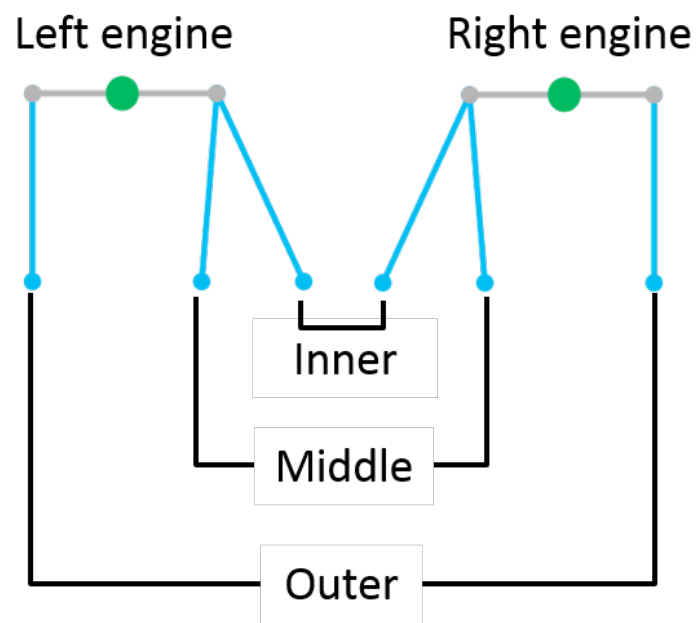
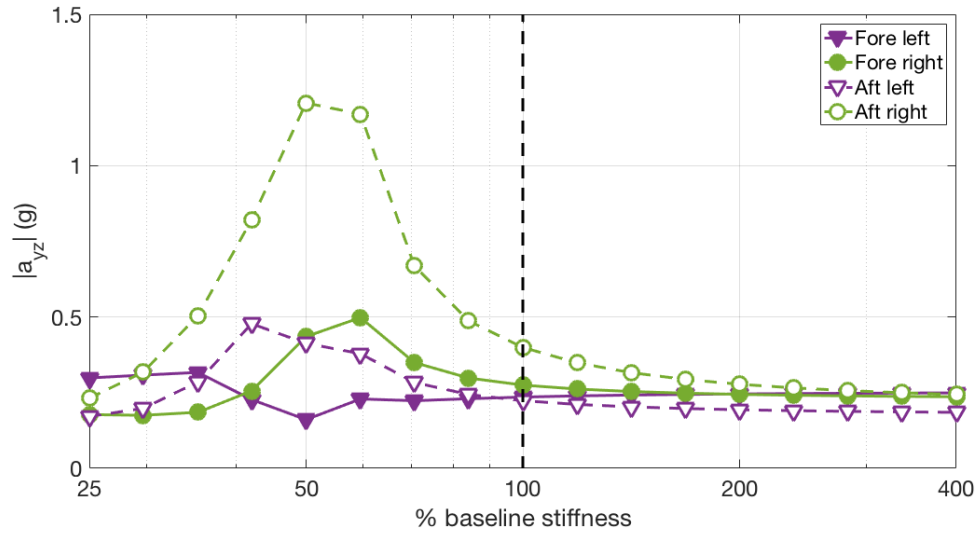
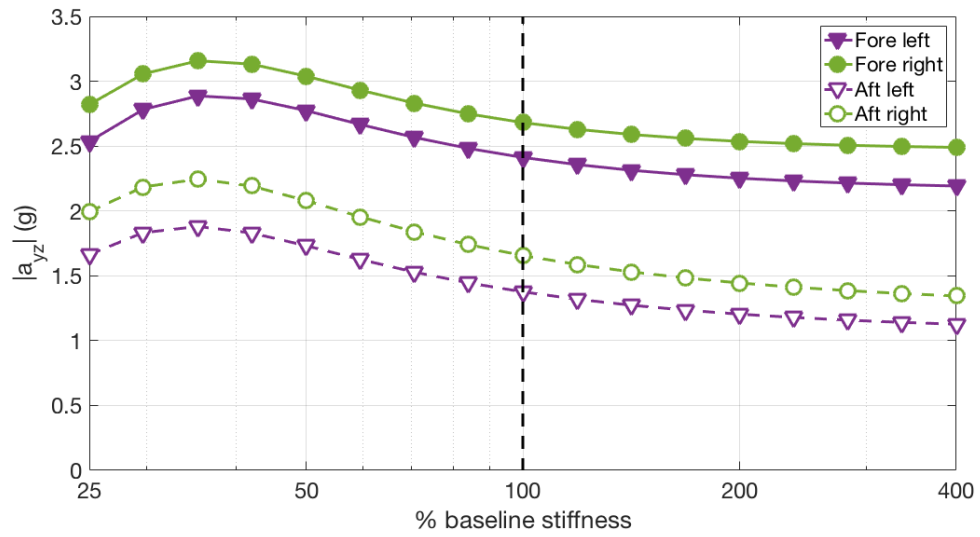


Figure 4.6: Schematic of engine mount structure

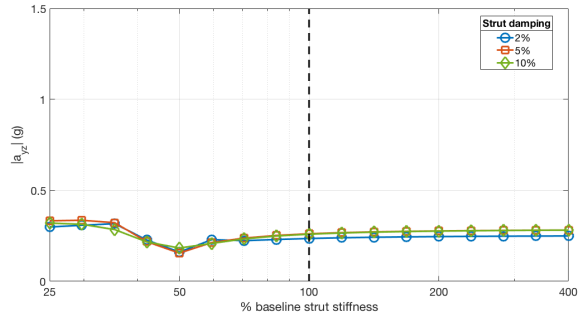


(a) 4P response

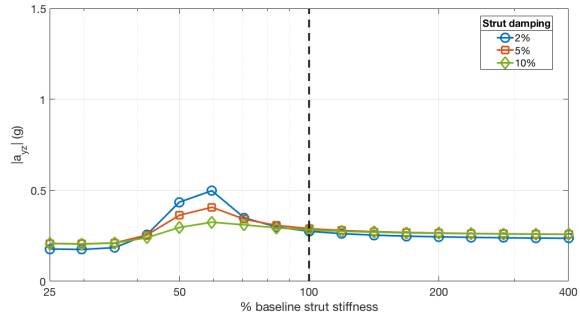


(b) 8P response

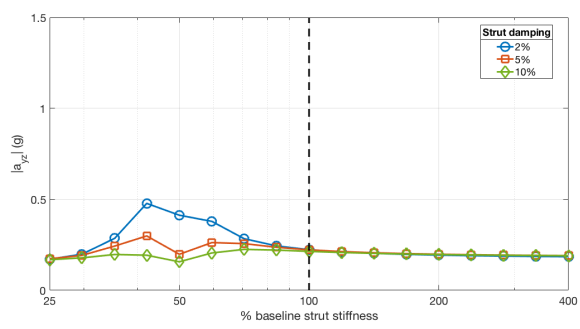
Figure 4.7: Transverse response of engine mount points for variations in all 6 strut stiffness matrices.



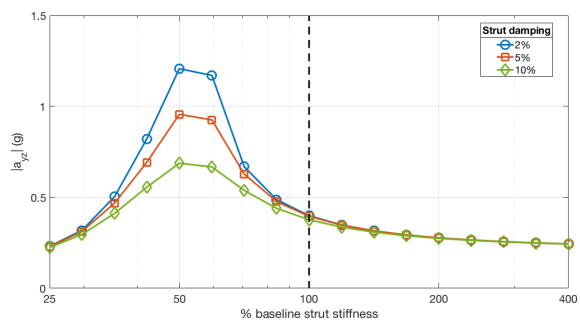
(a) Fore left



(b) Fore right

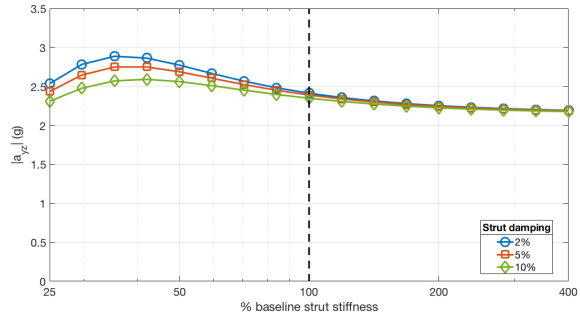


(c) Aft left

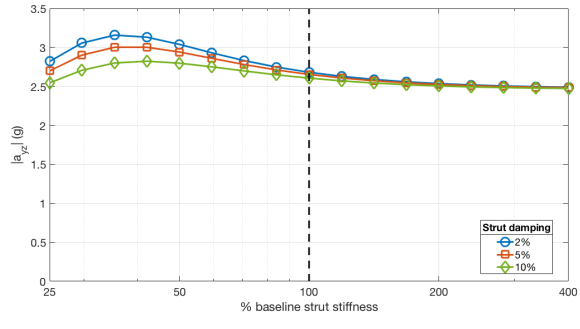


(d) Aft right

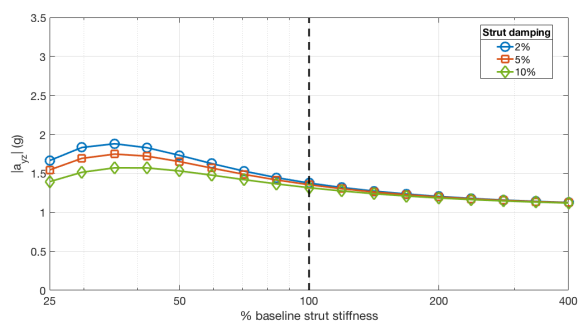
Figure 4.8: Transverse 4P response at engine mounts for variations in stiffness and damping of all 6 struts.



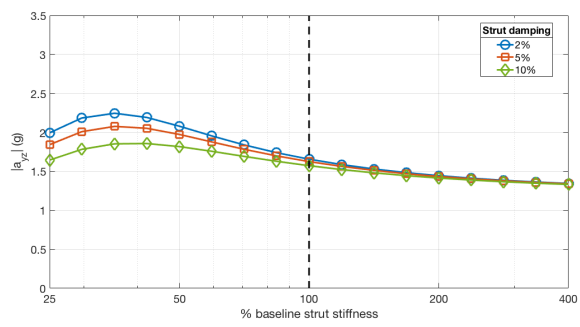
(a) Fore left



(b) Fore right

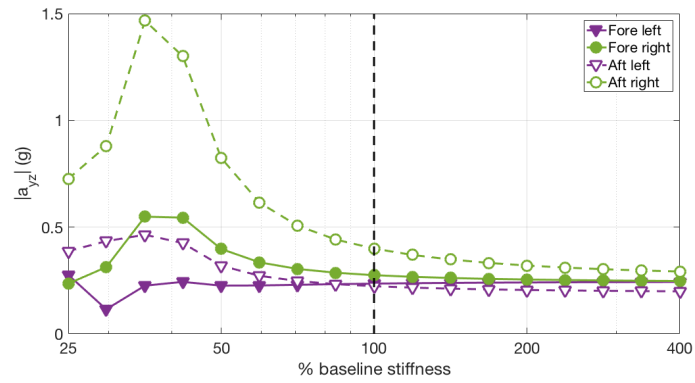


(c) Aft left

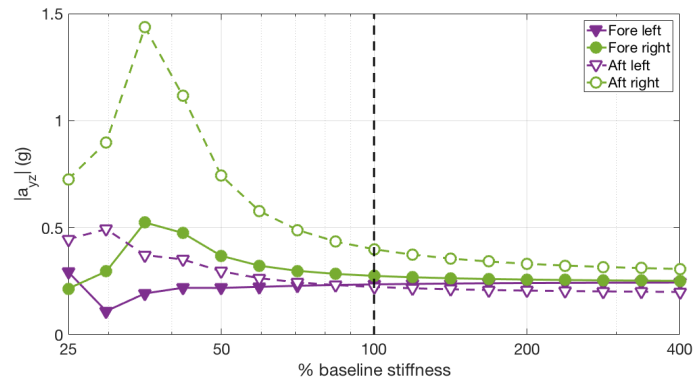


(d) Aft right

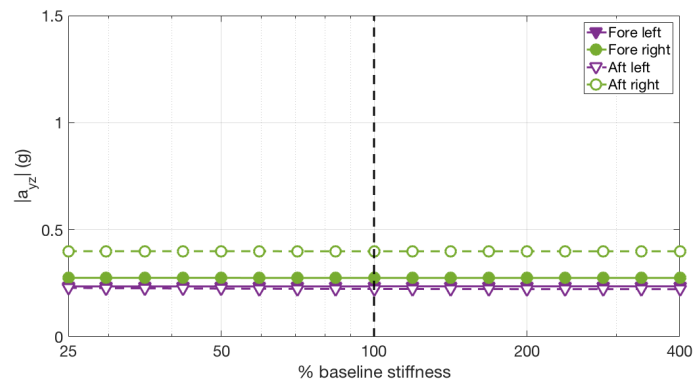
Figure 4.9: Transverse 8P response at engine mounts for variations in stiffness and damping of all 6 struts.



(a) Inner strut effects

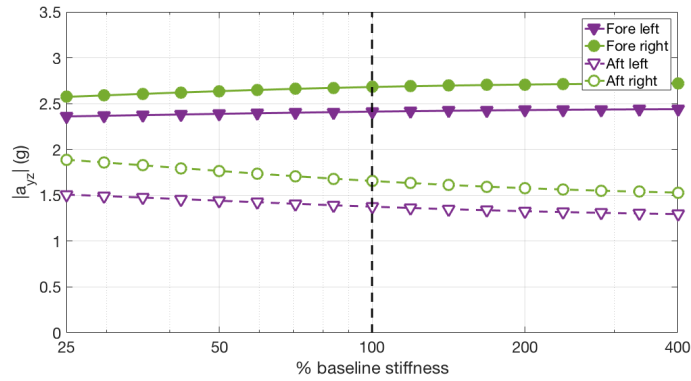


(b) Middle strut effects

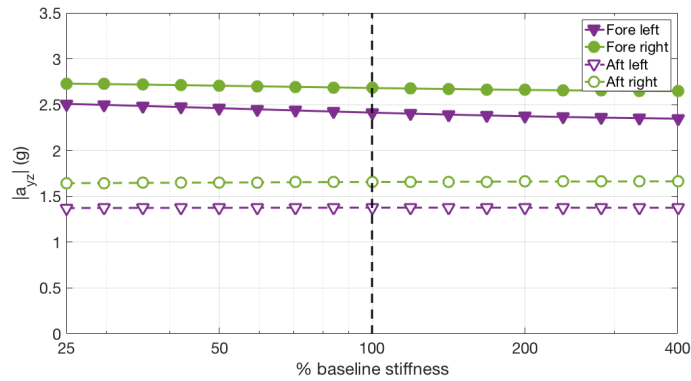


(c) Outer strut effects

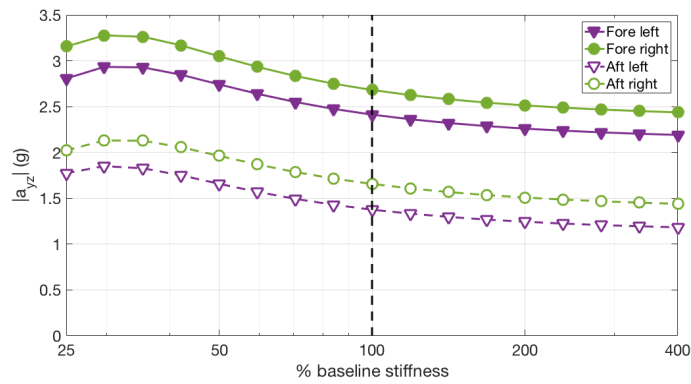
Figure 4.10: Transverse 4P response of engine mount points for left/right symmetric variations in each individual strut holding all others at baseline values.



(a) Inner strut effects

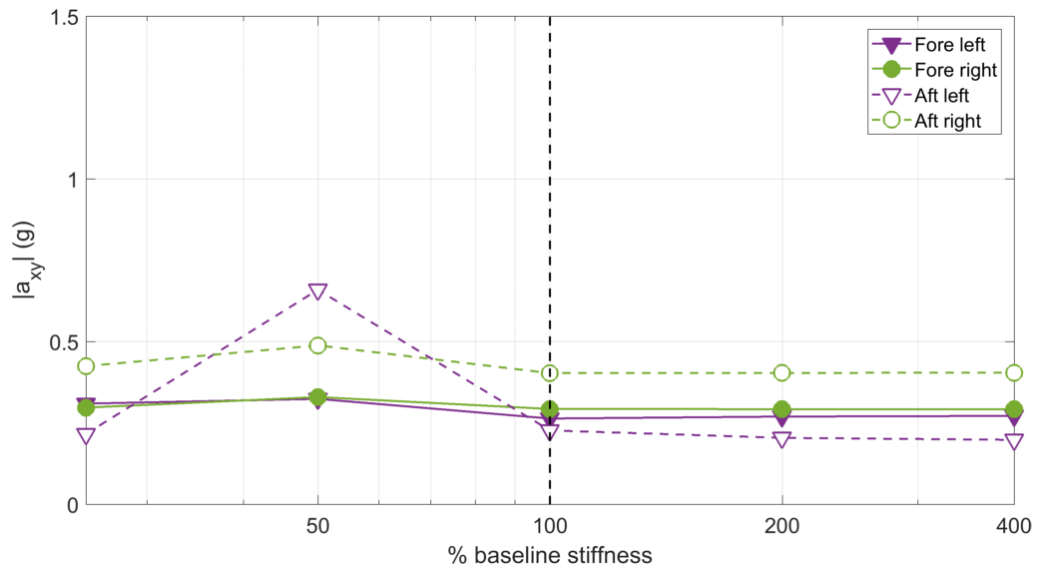


(b) Middle strut effects

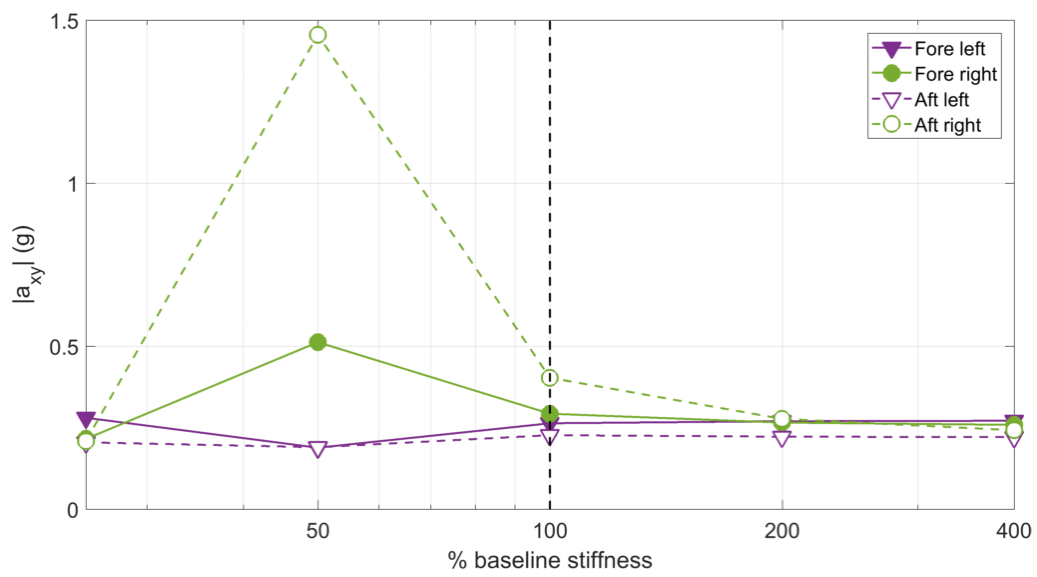


(c) Outer strut effects

Figure 4.11: Transverse 8P response of engine mount points for left/right symmetric variations in each individual strut holding all others at baseline values.

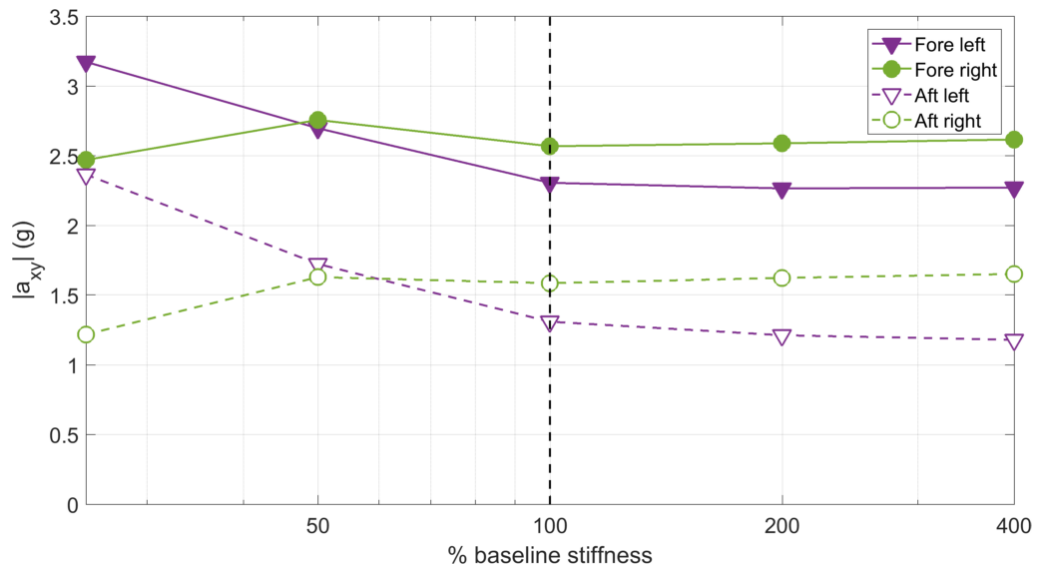


(a) Left strut stiffness effects

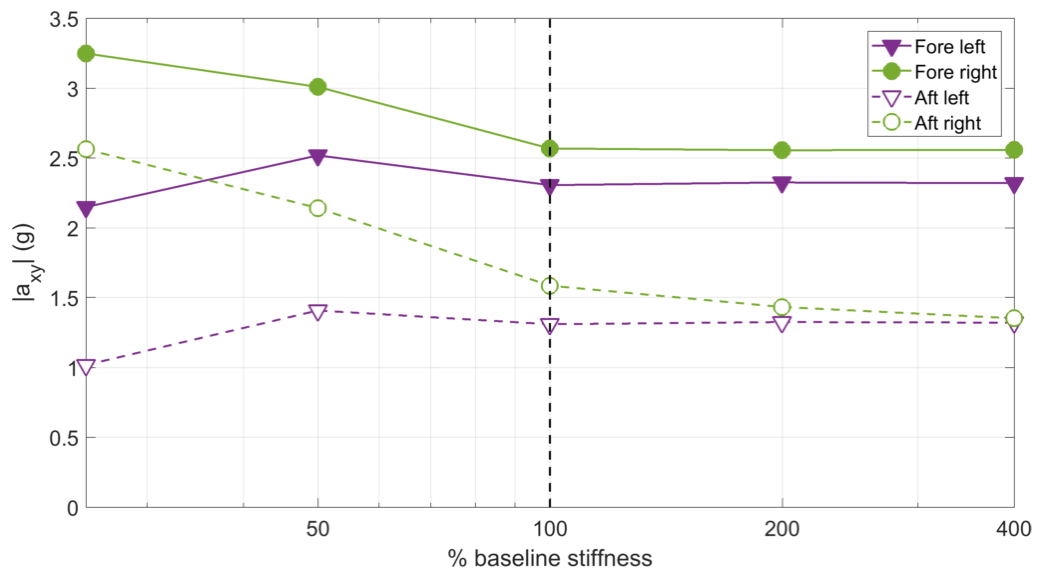


(b) Right strut stiffness effects

Figure 4.12: Effects of changes in left or right strut stiffness on 4P engine response

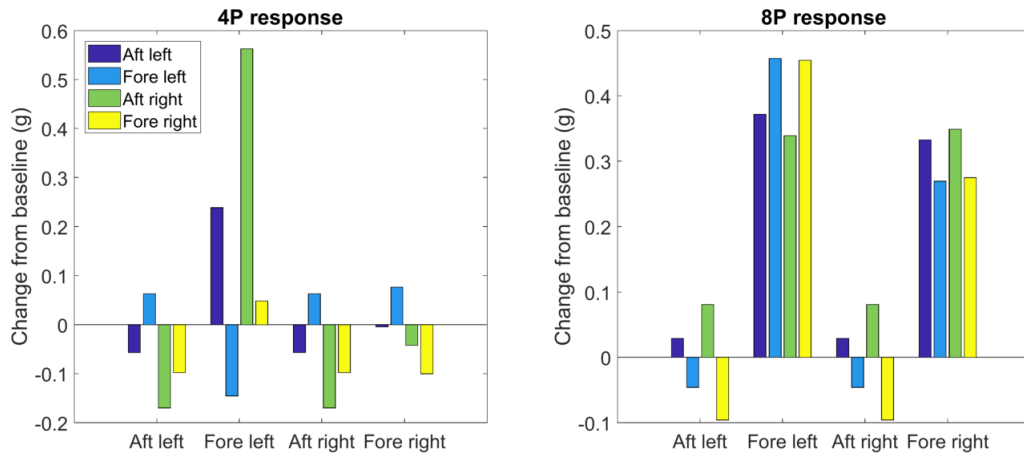


(a) Left strut stiffness effects

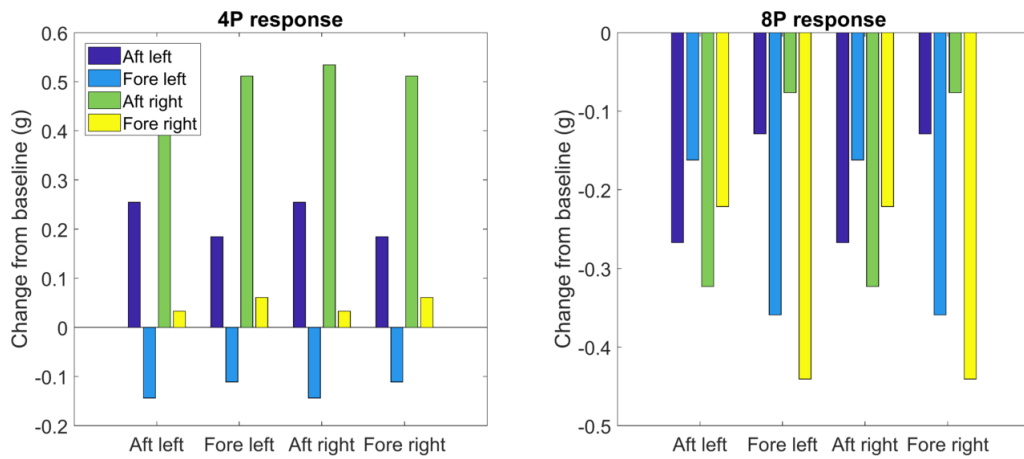


(b) Right strut stiffness effects

Figure 4.13: Effects of changes in left or right strut stiffness on 8P engine response

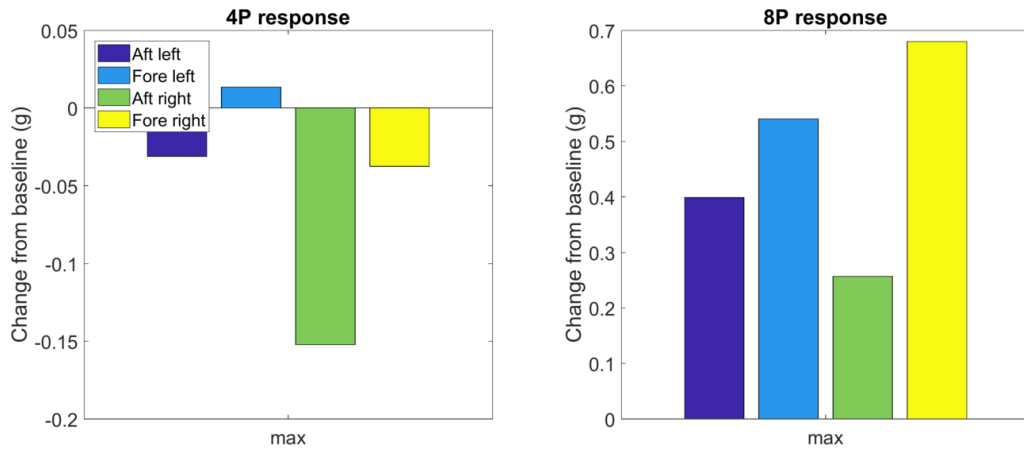


(a) Minimizing individual 4P response

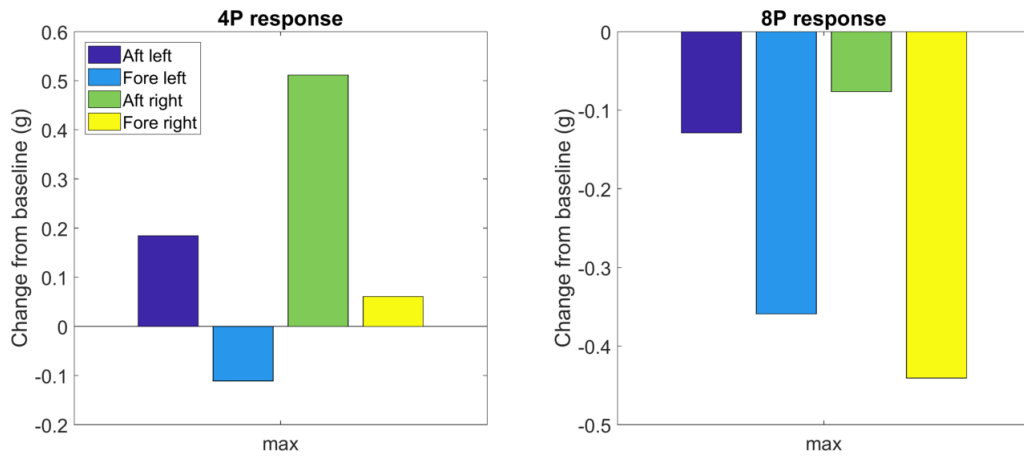


(b) Minimizing individual 8P response

Figure 4.14: Effect of minimizing response at individual engine mount point on response at other points: change in amplitude with respect to vibration for baseline strut design

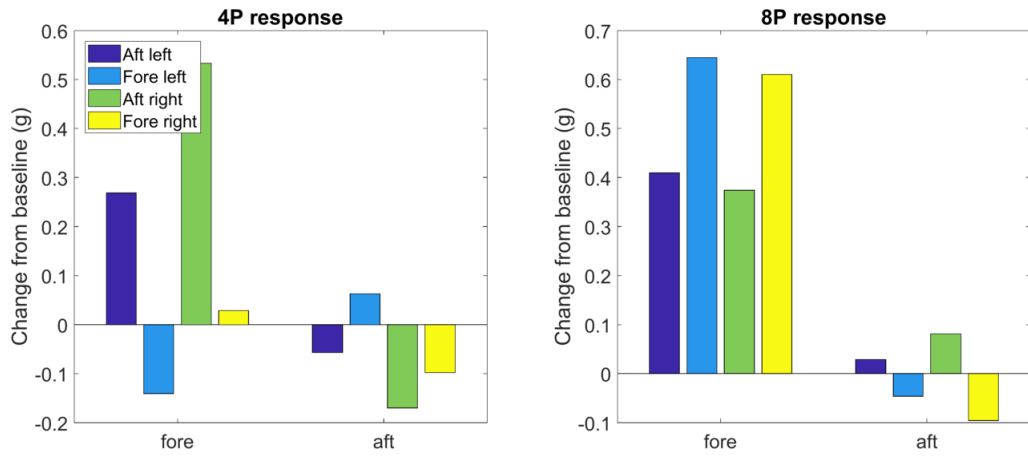


(a) Minimizing maximum 4P response

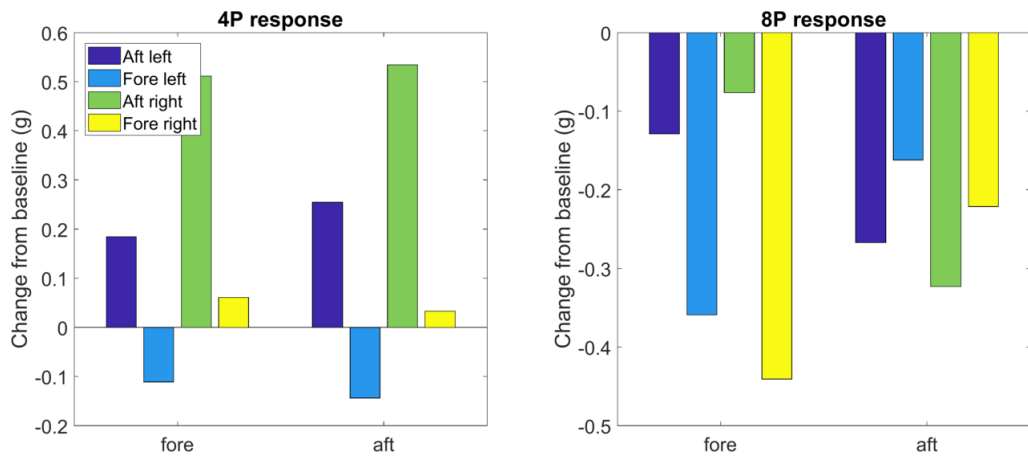


(b) Minimizing maximum 8P response

Figure 4.15: Effect of minimizing response at individual engine mount point on response at other points: change in amplitude with respect to vibration for baseline strut design

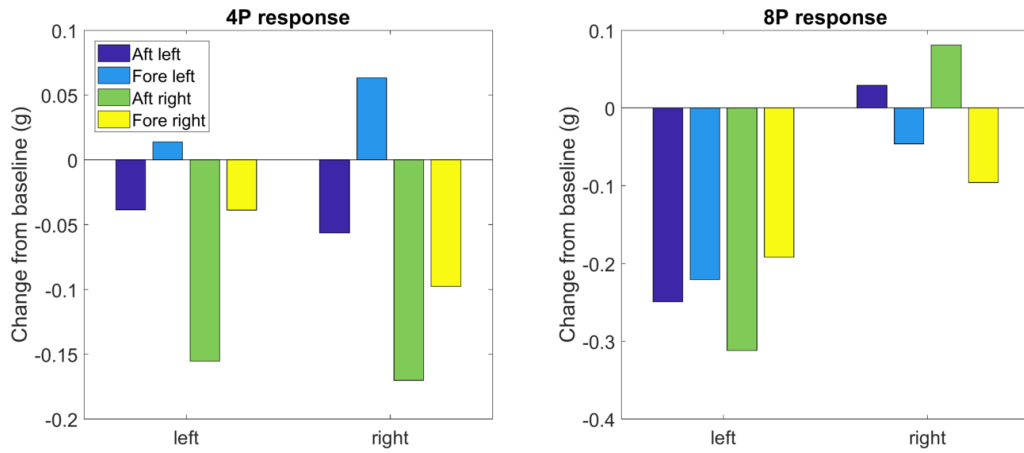


(a) Minimizing fore or aft 4P response

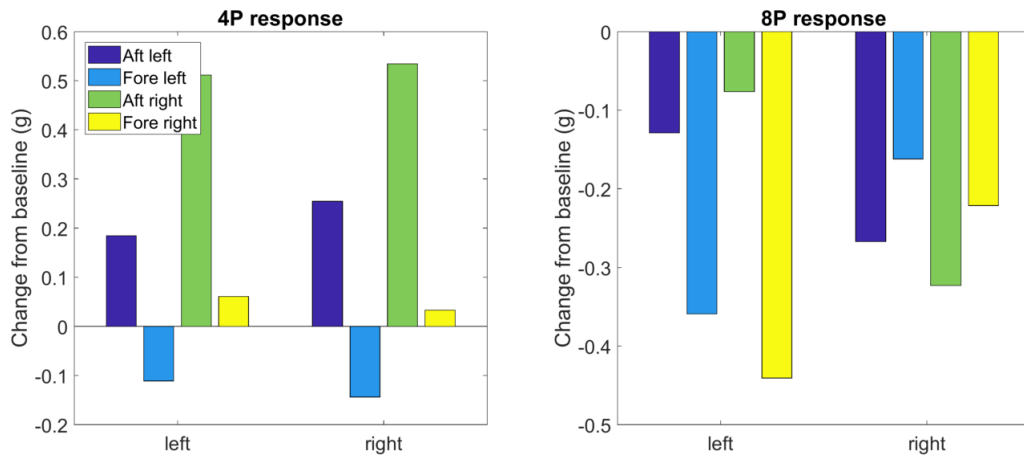


(b) Minimizing fore or aft 8P response

Figure 4.16: Effect of minimizing response of both fore or aft mount points: change in amplitude with respect to vibration for baseline strut design

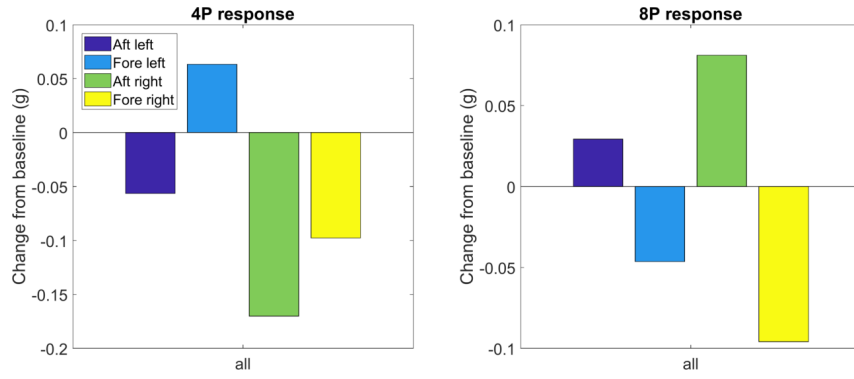


(a) Minimizing left or right 4P response

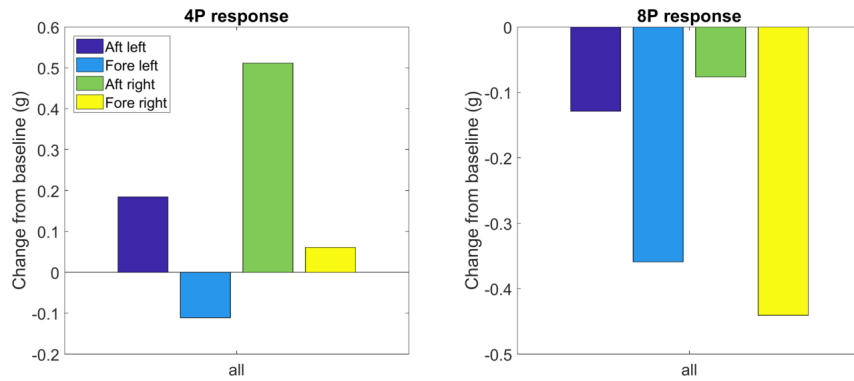


(b) Minimizing left or right 8P response

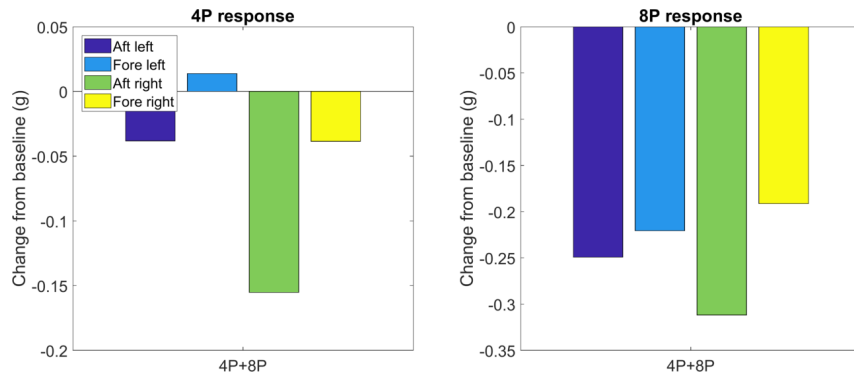
Figure 4.17: Effect of minimizing response of left or right engine mount points on response at other points: change in amplitude with respect to vibration for baseline strut design



(a) Minimizing average 4P response

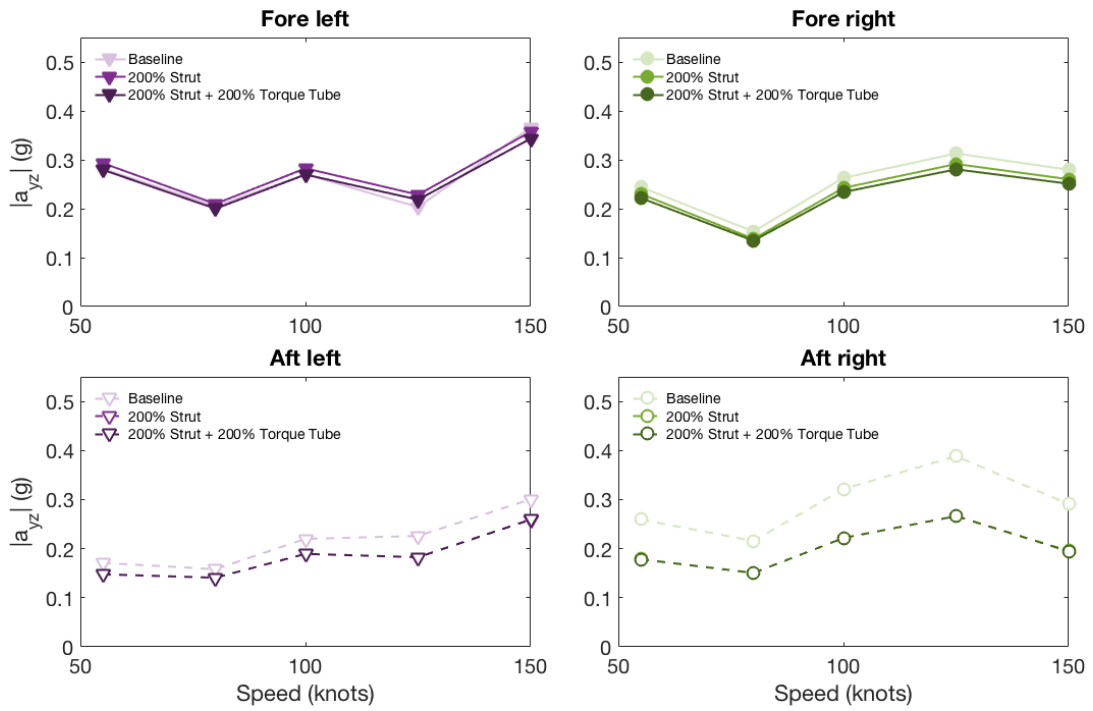


(b) Minimizing average 8P response

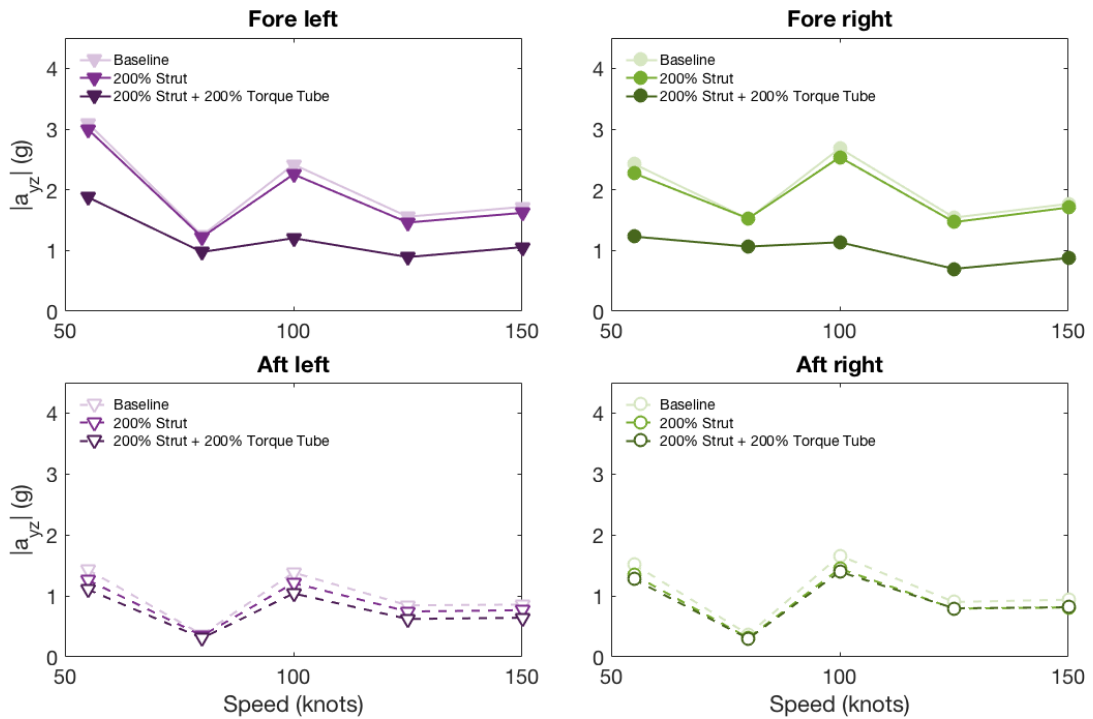


(c) Minimizing average combined 4P and 8P response

Figure 4.18: Effect of minimizing engine total engine response: change in amplitude with respect to vibration for baseline strut design



(a) 4P engine mount response: various airspeeds



(b) 8P engine mount response: various airspeeds

Figure 4.19: Effect of stiffer struts and stiffer torque tube on 4P and 8P engine mount response

Table 4.1: Amplitude of 4P engine mount point displacement response (in) to unit hub force (lb) or moment (ft-lb)

		Hub force component					
		F_x	F_y	F_z	M_x	M_y	M_z
fore left	x	1.37E-05	5.73E-06	4.52E-06	8.32E-08	3.63E-07	1.92E-07
	y	4.32E-06	3.92E-06	3.72E-06	8.17E-08	1.37E-07	3.72E-08
	z	3.95E-06	1.38E-05	8.68E-06	5.88E-07	7.34E-08	1.66E-07
fore right	x	1.38E-05	2.61E-06	8.92E-06	7.60E-08	5.45E-07	2.98E-07
	y	5.17E-06	4.41E-06	7.55E-06	5.08E-08	1.99E-07	8.33E-08
	z	3.36E-06	1.20E-05	6.43E-06	4.57E-07	8.60E-08	6.50E-08
aft left	x	1.35E-05	6.16E-06	4.36E-06	1.00E-07	3.55E-07	1.89E-07
	y	6.50E-06	1.41E-06	7.74E-06	3.70E-07	1.63E-07	9.44E-08
	z	4.03E-06	2.78E-06	4.25E-06	5.40E-08	2.11E-07	5.12E-08
aft right	x	1.36E-05	2.22E-06	9.09E-06	6.19E-08	5.39E-07	2.99E-07
	y	8.30E-06	2.41E-06	1.75E-05	3.10E-07	3.82E-07	2.11E-07
	z	3.89E-06	1.74E-06	2.57E-06	3.43E-08	1.24E-07	1.39E-08

Table 4.2: Amplitude of 8P engine mount point displacement response (in) to unit hub force (lb) or moment (ft-lb)

		Hub Force Component					
		F_x	F_y	F_z	M_x	M_y	M_z
fore left	x	3.43E-08	3.75E-07	8.15E-08	4.88E-08	9.08E-09	1.72E-08
	y	5.79E-07	2.67E-06	1.73E-06	3.62E-07	6.72E-08	3.15E-08
	z	3.74E-06	1.36E-06	6.81E-07	1.00E-07	3.73E-07	4.24E-08
fore right	x	6.43E-08	3.91E-07	6.42E-08	5.19E-08	1.08E-08	1.55E-08
	y	9.42E-07	2.90E-06	1.74E-06	3.96E-07	1.30E-07	2.76E-08
	z	3.66E-06	1.25E-06	4.66E-07	8.45E-08	3.63E-07	4.47E-08
aft left	x	1.51E-07	2.90E-07	1.76E-07	4.06E-08	2.01E-08	1.72E-08
	y	3.75E-07	3.67E-07	4.51E-07	5.82E-08	3.64E-08	7.73E-09
	z	1.96E-07	1.68E-06	3.71E-06	2.19E-07	2.36E-08	4.50E-08
aft right	x	1.57E-07	3.09E-07	2.05E-07	4.36E-08	1.78E-08	1.63E-08
	y	4.42E-07	3.88E-07	5.46E-07	6.43E-08	4.41E-08	4.22E-09
	z	2.22E-07	1.74E-06	4.80E-06	2.34E-07	2.56E-08	3.27E-08

Table 4.3: Baseline vibration levels at engine mount points at 100 knots

	4P	8P
Fore left	0.26g	2.31g
Fore right	0.29g	2.57g
Aft left	0.23g	1.59g
Aft right	0.40g	1.31g

Table 4.4: Strut stiffness factors required to achieve minimum 4P or 8P response at each engine mount

			Inner		Middle		Outer	
			Left	Right	Left	Right	Left	Right
4P	Aft left	Asymmetric	25%	200%	25%		400%	
		Symmetric	25%					
	Fore left	Asymmetric	200%	50%	25%	50%	25%	25%
		Symmetric	400%		25%		200%	
	Aft right	Asymmetric	100%	25%	50%	25%	25%	400%
		Symmetric	25%		25%		400%	
	Fore right	Asymmetric	200%	50%	25%		25%	
		Symmetric	42%					
8P	Aft left	Asymmetric	400%	25%	25%		400%	25%
		Symmetric	400%				400%	
	Fore left	Asymmetric	25%		400%	25%	400%	25%
		Symmetric			400%		400%	
	Aft right	Asymmetric	25%	400%	25%		25%	400%
		Symmetric	400%				400%	
	Fore right	Asymmetric	25%		25%	400%	25%	400%
		Symmetric			400%		400%	

Table 4.5: Largest possible reduction from baseline in 4P and 8P transverse for each mount point for symmetric and asymmetric strut stiffness values

		Asymmetric		Symmetric	
4P	Aft left	-0.10g	-44.90%	-0.06g	-24.34%
	Fore left	-0.23g	-85.66%	-0.16g	-60.26%
	Aft right	-0.20g	-50.24%	-0.17g	-42.93%
	Fore right	-0.11g	-36.55%	-0.09g	-29.31%
8P	Aft left	-0.50g	-36.70%	-0.27g	-19.44%
	Fore left	-0.46g	-19.24%	-0.36g	-14.89%
	Aft right	-0.64g	-38.75%	-0.32g	-19.50%
	Fore right	-0.48g	-17.75%	-0.44g	-16.44%

Table 4.6: Strut stiffness factors that produce minimum response for different targets

		Inner		Middle		Outer	
		Left	Right	Left	Right	Left	Right
4P total	Symmetric	25%		25%		400%	
	Asymmetric	400%	25%	400%	25%		
8P total	Symmetric	25%		400%		400%	
	Asymmetric	25%	400%	400%	25%		
4P + 8P	Symmetric	400%		400%		400%	
	Asymmetric	50%	400%				

Table 4.7: Summary of parametric studies performed

Parameter	Range	Summary
strut stiffness	25-400% baseline	4P response unaffected by stiffness of outboard struts; 8P response unaffected stiffness of inboard struts
strut damping	2%, 5%, 10%	Response unaffected by damping at high stiffness
torque tube stiffness	25-400% baseline	8P response of fore mount most affected; increasing stiffness decreases response

Table 4.8: Strut stiffness factors that produce minimum response for different targets

		Inner		Middle		Outer	
		Left	Right	Left	Right	Left	Right
4P total	Symmetric	25%		25%		400%	
	Asymmetric	400%	25%	400%	25%		
8P total	Symmetric	25%		400%		400%	
	Asymmetric	25%	400%	400%	25%		
4P + 8P	Symmetric	400%		400%		400%	
	Asymmetric	50%	400%				

5 Coupled Rotor-Airframe-Drivetrain Analysis

A coupled analysis was undertaken to examine the effects of the various fixed frame components on the rotor loads and hub loads. The effects of coupling on the vibratory loads experienced by the engines were also investigated. Prescribed airloads were used to compare results with existing test data as well as work performed by other researchers. Free-flight analysis was performed on an expanded flight envelope to examine the importance of these effects at different flight conditions. Results were obtained for $C_W/\sigma = 0.084$ and steady level flight conditions with forward speeds of 50-175 knots (advance ratios $\mu = 0.12 - 0.41$).

5.1 Baseline Coupling Results (Prescribed Airloads)

The results in this section utilize measured airload and lag damper data from the NASA/Army UH-60A Airloads Flight Test Program [88] for a high speed flight condition (C8534). A baseline, uncoupled analysis (fixed hub condition) is performed

and compared with results of coupling with the RSRA drivetrain model and the airframe model described in Chapter 3. The coupled and uncoupled results are compared to existing flight test data.

Figure 5.1 shows the waveform for the blade flap bending moments at 30%, 50%, and 70% radial stations. These plots show little discernible effect of drivetrain coupling on the flap bending moments, while the airframe coupling has a more noticeable, though still small effect. These effects can be better demonstrated when the waveform is broken down by harmonic content, as shown in Figs. 5.2 and 5.3. In particular, the drivetrain coupling has only a small effect on the 4/rev flap bending moment. On the other hand, the airframe coupling has the most noticeable effect on the 4/rev and 5/rev flap bending moments. Further, although the effects of airframe coupling are noticeable, there is not a marked improvement in the correlation between the prediction and test data.

The chordwise bending moments are shown in Fig. 5.4, with the harmonic content shown in Figs. 5.5 and 5.6. The drivetrain coupling has a more noticeable effect on the chordwise bending than observed for the flap bending moments. In particular, there is a slight increase in the 1/2 peak-to-peak amplitude and 4/rev component, resulting in an overall improvement of the correlation with flight test data. The airframe coupling also had a larger effect on the chordwise bending, particularly decreasing the 5/rev and increasing the 6/rev content, again leading to slightly improved correlation.

Overall, these results show that the flap bending moments are not much affected by either the drivetrain or airframe coupling, though the airframe coupling

has a noticeable small effect on the 4/rev and 5/rev components. On the other hand, the chordwise bending moments do show effects from both the drivetrain and airframe coupling. These results agree qualitatively with similar studies [51, 52].

5.2 Rotor-Airframe-Drivetrain Coupling

The results in this section are obtained for free flight from 50–175 knots using Maryland Free Wake. A baseline case was computed with a hub fixed rigidly to the aircraft, and coupled results were obtained for the rotor coupled separately with the drivetrain and airframe described in Sections 3.2 and 3.3, as well as for the rotor coupled with both the drivetrain and airframe. The flexible engine model was included in the airframe model for these results.

5.2.1 Hub motion

The 1/2 peak-to-peak amplitude of the hub motion relative to the airframe resulting from coupling with either the flexible airframe, drivetrain, or both is examined in this section. Figure 5.13 shows the three degrees of freedom of hub translation due to coupling with the airframe only as well as the airframe and drivetrain together. These results show that the coupling produces very small hub motions, generally less than 0.05 in. The in-plane hub motions remain relatively consistent for flight speeds from 50 to 125 knots. At 175 knots, the longitudinal hub motion increases by approximately three times compared to the lower speeds, while the lateral hub motion increases by four times the lower speeds. The vertical hub motion is

highest at 50 and 175 knots, with a minimum around 100 knots, while being overall lower than the in-plane motion by almost an order of magnitude. The pitch and roll rotation of the hub, shown in Fig. 5.14, average around 0.03 degrees and show similar trends to the in-plane hub translations, with substantial increases at 175 knots.

Figures 5.13 and 5.14 also reveal that the addition of the drivetrain coupling does not significantly change the hub translation or pitch/roll rotations beyond the effects of the airframe coupling. This is not surprising, given that the drivetrain is only coupled to the torsional degree of freedom of the rotor, and so should not significantly affect the other degrees of freedom. On the other hand, the airframe does have a significant effect on the torsional motion of the rotor hub beyond that of the drivetrain only, as shown in Fig. 5.15. Generally, the addition of the airframe to the rotor-drivetrain coupling serves to decrease the peak-to-peak torsional motion of the rotor by 25-35%.

5.2.2 Blade loads

Figure 5.16 shows the uncoupled and coupled mid-span flap and lag bending and torsion moment for the 75 knots flight condition. From the waveforms, it is evident that the effects of coupling are smallest for the flap bending moment, with the drivetrain coupling having the greatest effect. The torsion moment is largely unaffected by the drivetrain coupling alone, while noticeably affected by the presence of the airframe model. The lag bending moment appears significantly affected by

the presence of the airframe, while also affected to a lesser degree by the drivetrain coupling.

To better quantify the effects of the various couplings on the bladeloads, it is instructive to examine the peak-to-peak and vibratory components of the waveforms over the entire span of the blade. Figures 5.17 and 5.18 show the half peak-to-peak and vibratory flap bending components. These results show that the drivetrain has very little effect on the flap bending moment overall. There is a minor reduction in the peak-to-peak flap bending at the root and mid-span. There are also noticeable reductions in higher harmonics (7, 8, 9/rev), with the 8/rev reduction being particularly significant, though these components fairly small. The airframe coupling had a more noticeable, though still small, effect on the flap bending, with a significant impact on the 5/rev flap bending load, reducing the 5/rev component by 50% or more across the entire blade span.

Figures 5.19 and 5.20 show the half peak-to-peak and vibratory flap bending components, and confirm that the coupled analysis has a greater impact on these loads than the flap bending loads. The drivetrain has a large effect on the higher harmonics, particularly the 8/rev component, which is increased by as much as 200% at about 0.7R. On the other hand, the airframe coupling has very little effect on most on the lag bending components, except for the 5/rev component, which is reduced by about 50% at the mid-span.

Figures 5.21 and 5.22 show the half peak-to-peak and vibratory torsion moment components. The drivetrain significantly reduces the 8/rev torsion moment, while having very little effect on the other vibratory components. The airframe

coupling has the biggest impact on the 5/rev and 6/rev components, though all are somewhat affected.

5.2.3 Hubloads

Although the magnitude of the hub motion that results when the rotor is coupled to a flexible component is very small and the overall effect on the blade loads is generally small, as shown in the previous sections, the change in the vibratory hubloads that results from this motion can be significant. Figures 5.23 and 5.24 show the 4P and 8P hub forces and moments for the uncoupled rotor as well as the rotor coupled with either the drivetrain, airframe or both. The drivetrain alone has very little effect on the 4P in-plane force, and a more noticeable, though small effect on the 4P vertical force and in-plane moments, primarily at 150 knots. On the other hand, the 8P hubloads are more impacted by the presence of the drivetrain, particularly the vertical force at 50-125 knots and in-plane moment at 50 and 125 knots.

Coupling with the airframe alone decreases the 4P vertical force from the uncoupled baseline. This effect is small and increases with increasing flight speed, resulting in about a 10% reduction in 4P vertical force at 175 knots. On the other hand, the airframe coupling increases the 4P in-plane forces and moments, as well as all 8P hub loads across all flight speeds. The effect is most pronounced for the in-plane force. The 4P and 8P in-plane forces are increased by 60-100%

Finally, the addition of the drivetrain to the rotor-airframe coupling follows

similar trends as the addition of the drivetrain compared to the uncoupled case. For instance, the drivetrain increases the 4P vertical force by about 5% from the uncoupled case. Similarly, the airframe/drivetrain coupling increases the 4P vertical force by about 5% from the airframe coupling alone.

5.2.4 Airframe Vibrations

Although identifying the effects of various couplings on the structural loads in the blades and fixed frame hubloads is important to deepening our overall understanding of the physics at work, from a practical standpoint, it is the resulting vibrations experienced throughout the airframe, particularly at the pilot and copilot seat, that are of greatest interest to helicopter users. Figures 5.25 and 5.26 show the transverse and vertical 4P and 8P acceleration at grid points corresponding to the pilot and co-pilot seats of the airframe. Vibration levels for the uncoupled case were calculated by applying the calculated hub loads from the uncoupled analysis to the airframe finite element model. These results show that the coupled model generally predicts lower 4P vibration and higher 8P vibration at the pilot/co-pilot seats than the uncoupled analysis, though the difference between the uncoupled and coupled analysis is much more significant for the 4P vibrations. The addition of the drivetrain model to the airframe coupling has little impact on the 4P vertical vibration and no discernible impact on the 4P transverse acceleration. The 8P vibrations are much more impacted by the presence of the drivetrain in addition to the airframe.

5.3 Engine modeling

The fully coupled results shown in the previous section include a detailed flexible engine model coupled to the airframe. The turboshaft engines used in helicopters have heavy rotors spinning at very high speeds (20,000 RPM) which produce gyroscopic forces that are transmitted through the airframe. The detailed NASTRAN engine model provided for this work included gyroscopic elements that can be turned on and off within NASTRAN. For the analysis presented thus far, these gyroscopic effects were neglected. The following results will examine the impact of the complexity of the engine model on the analysis, including the effects of including gyroscopic forces. Four cases are considered:

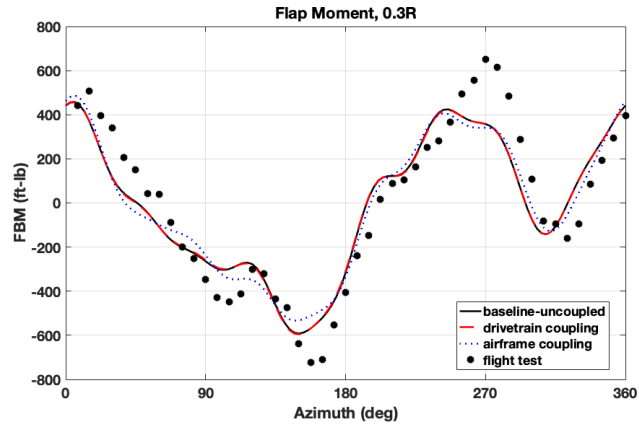
1. flexible airframe without any engine model
2. flexible airframe with rigid engine mass
3. flexible airframe with flexible engine
4. flexible airframe with flexible engine with gyroscopic forces.

Figures 5.27 and 5.28 show the 4P and 8P vertical hub forces and in-plane hub forces and moments for the uncoupled baseline and the four coupled cases. These results show that the presence of an engine model of any complexity has the greatest impact on the in-plane hub forces. There is very little difference between the rigid, flexible, and gyroscopic engine in the prediction of 4P hub loads. The 8P hub loads are more sensitive to engine modeling, particularly at high speeds,

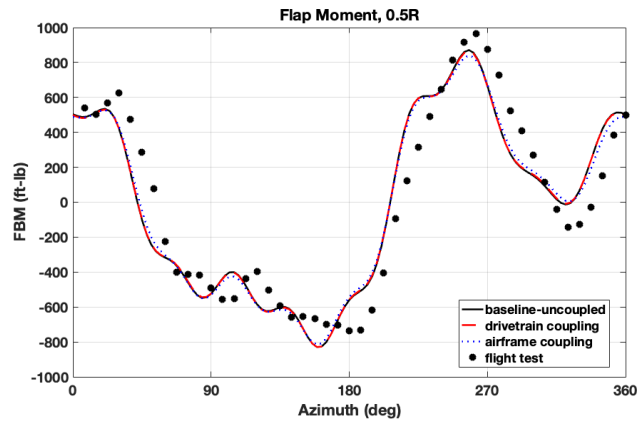
though the gyroscopic forces do not a discernible impact when compared to the flexible engine without gyroscopic forces.

Figures 5.29 and 5.30 compare the effects of the engine modeling on the 4P and 8P accelerations calculated at the pilot and co-pilot seats. Since the vibratory hub loads driving the vibrations throughout the airframe are not much influenced by the differences in engine modeling, the differences in vibrations at the pilot/co-pilot seats are due to differences in the models.

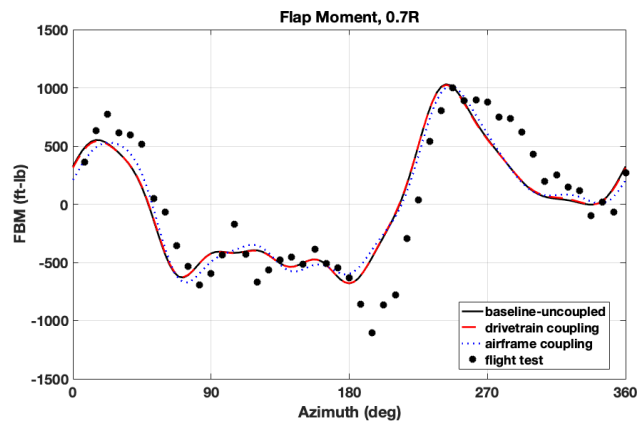
Figures 5.31 and 5.32 compare the effects of the engine modeling on the 4P and 8P accelerations calculated at the four engine mount points identified in Chapter 3. At 4P, the flexibility of the engine model increases the vibration predicted on the left engine and decreases the predicted vibration on the right engine when compared to the rigid engine model. Further, the gyroscopic forces have no noticeable effect on the 4P vibrations. On the other hand, the 8P engine vibrations are highly susceptible to differences in engine models. The gyroscopic engine modeling drastically increases the 8P vibrations on the left engine compared to to the flexible engine, while decreasing the 8P vibrations on the right engine.



(a) 30%R

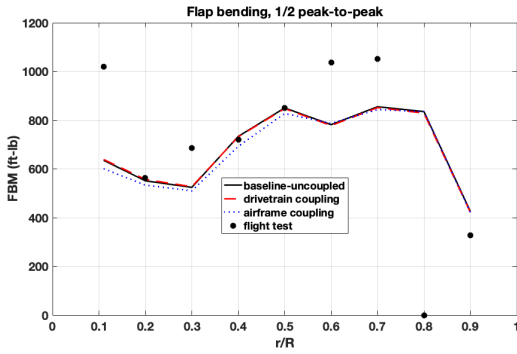


(b) 50%R

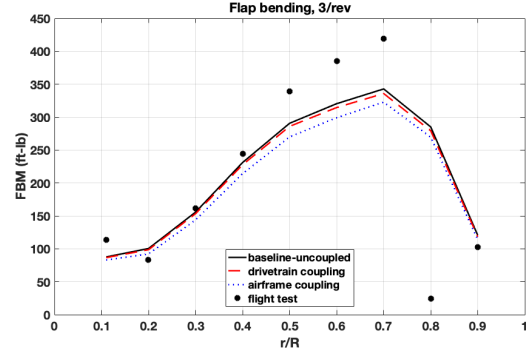


(c) 70%R

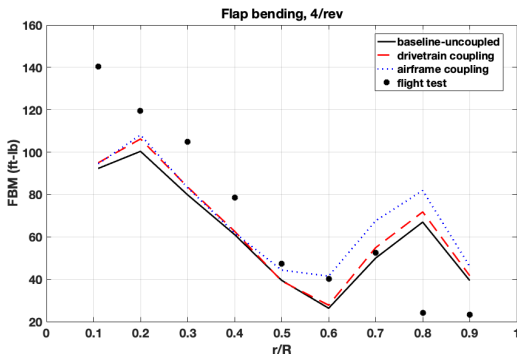
Figure 5.1: Effects of coupling on flap bending moments for UH-60A using measured airloads (C8534)



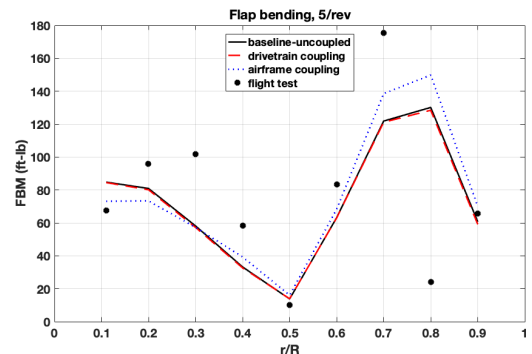
(a) 1/2 peak-to-peak



(b) 3/rev



(c) 4/rev



(d) 5/rev

Figure 5.2: Effects of coupling on flap bending moment peak-to-peak amplitude and harmonics for UH-60A using measured airloads (C8534)

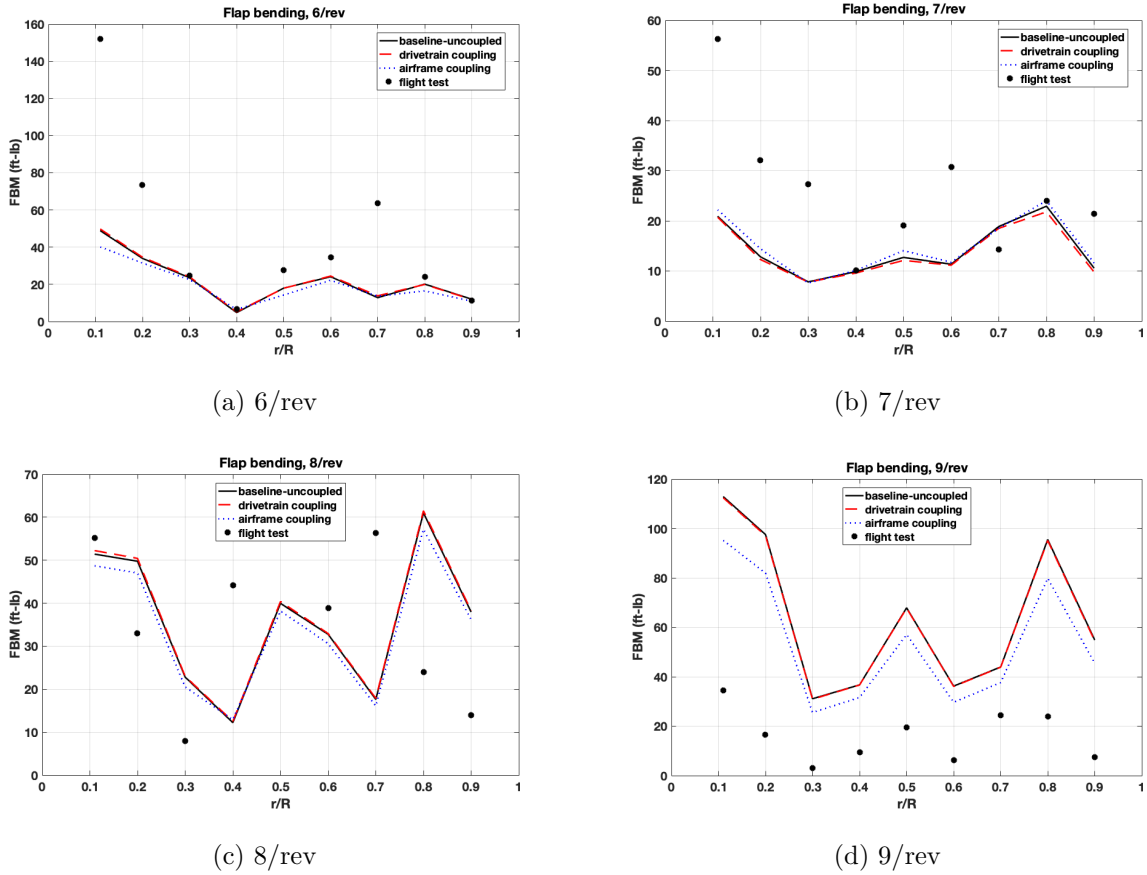
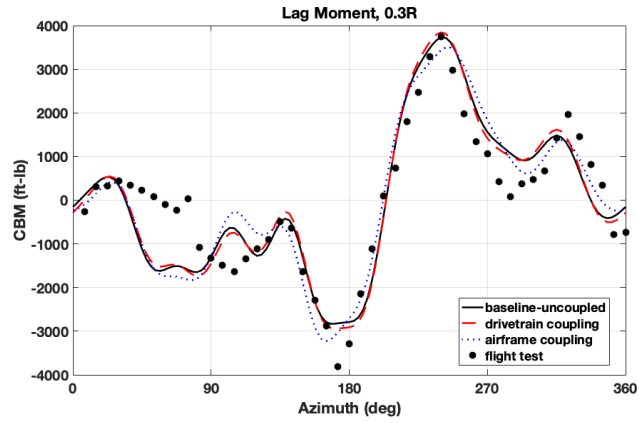
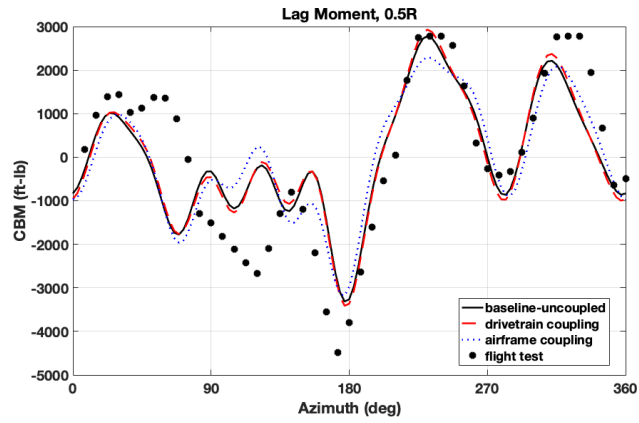


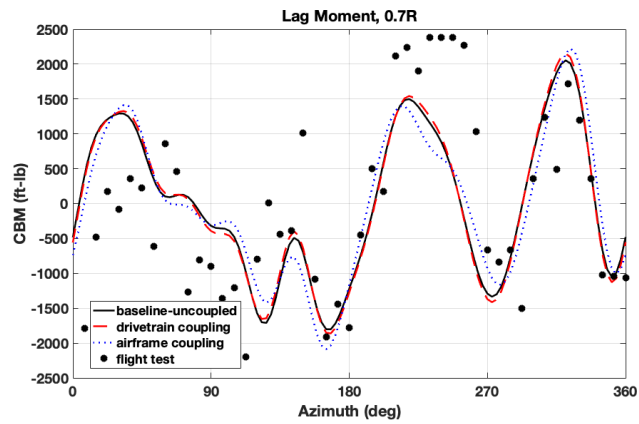
Figure 5.3: Effects of coupling on flap bending moment higher harmonics for UH-60A using measured airloads (C8534)



(a) 30%R

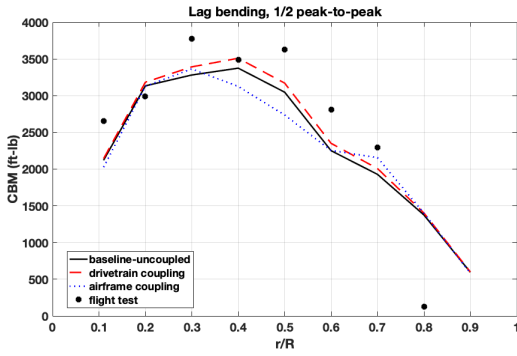


(b) 50%R

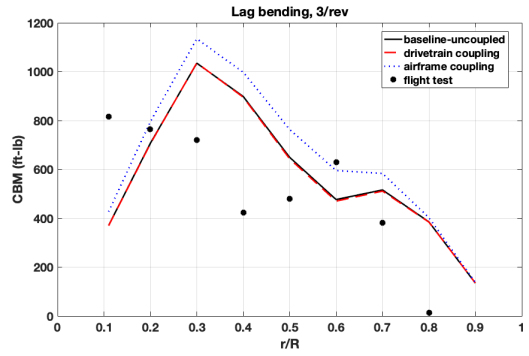


(c) 70%R

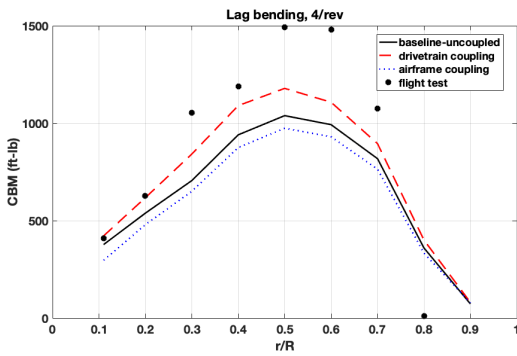
Figure 5.4: Effects of coupling on chordwise bending moments for UH-60A using measured airloads (C8534)



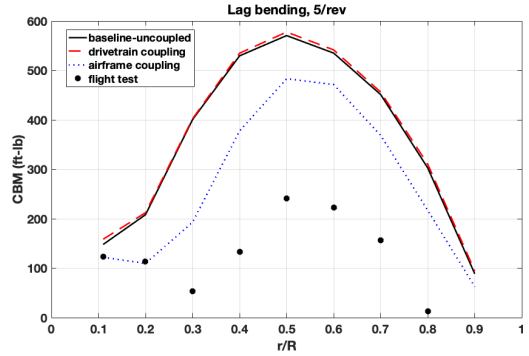
(a) 1/2 peak-to-peak



(b) 3/rev

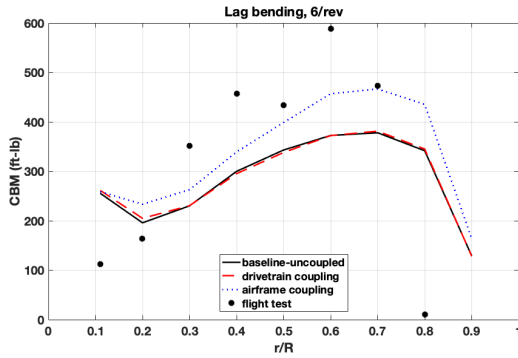


(c) 4/rev

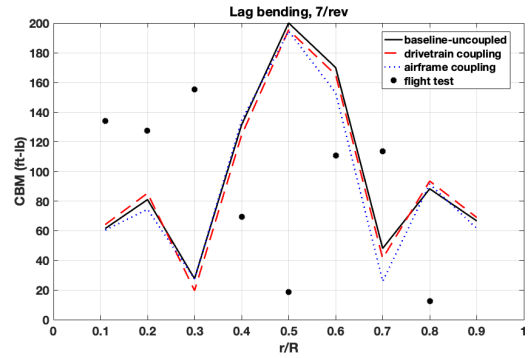


(d) 5/rev

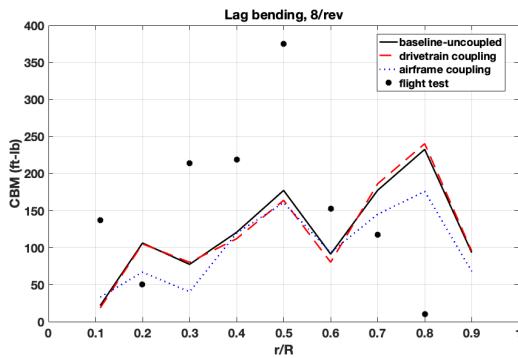
Figure 5.5: Effects of coupling on chordwise bending moment peak-to-peak amplitude and harmonics for UH-60A using measured airloads (C8534)



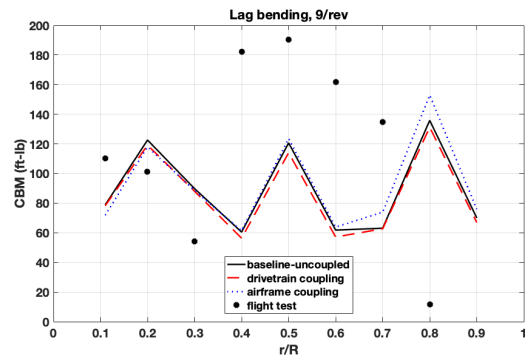
(a) 6/rev



(b) 7/rev

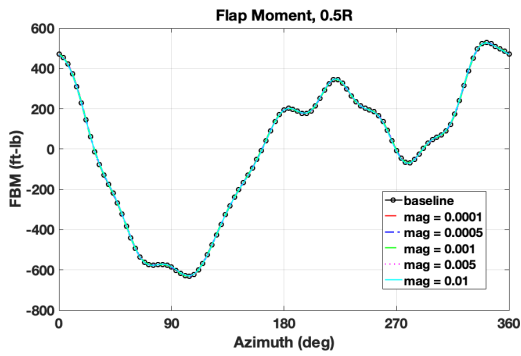


(c) 8/rev

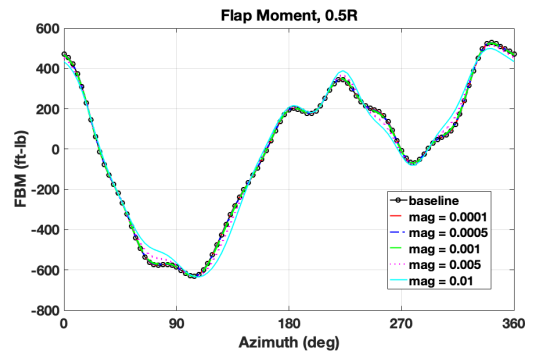


(d) 9/rev

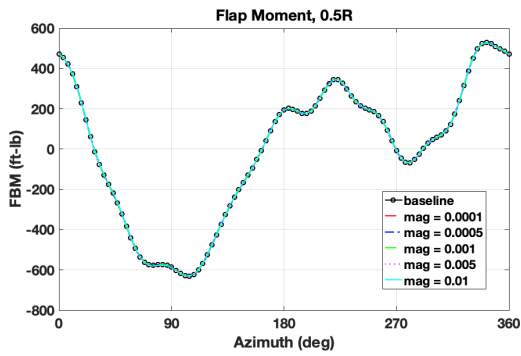
Figure 5.6: Effects of coupling on chordwise bending moment higher harmonics for UH-60A using measured airloads (C8534)



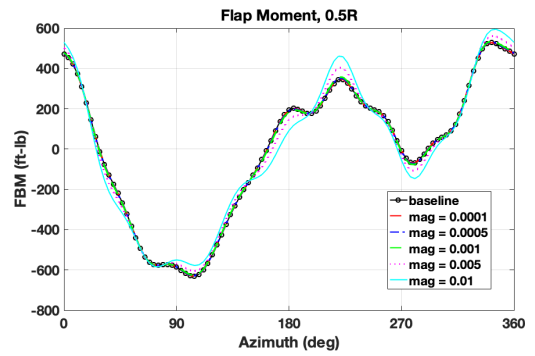
(a) x motion



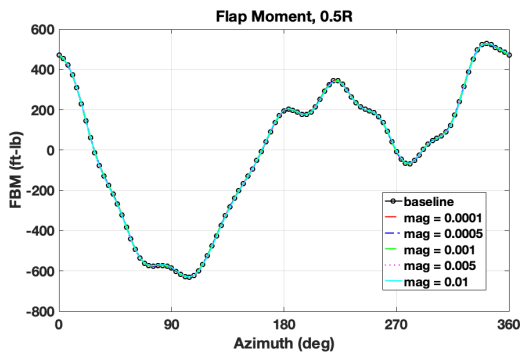
(b) θ_x motion



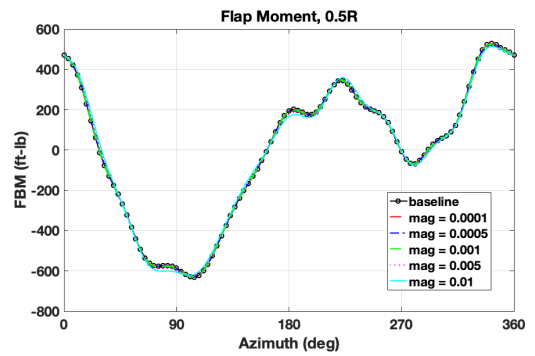
(c) y motion



(d) θ_y motion

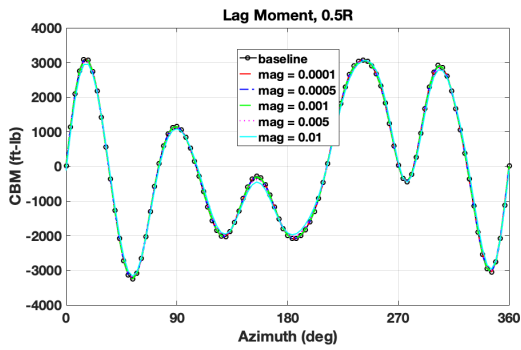


(e) z motion

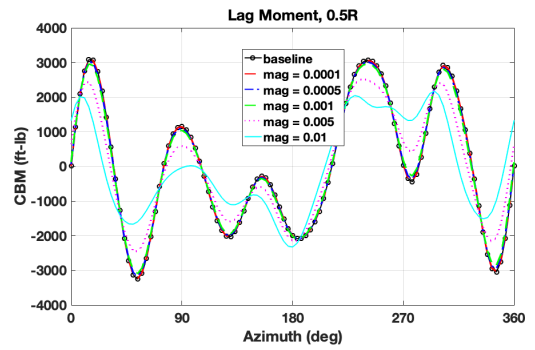


(f) θ_z motion

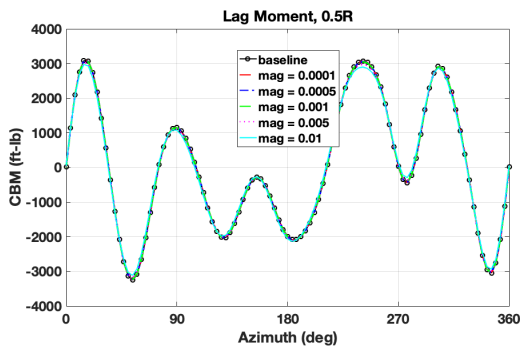
Figure 5.7: Effects of single degree of freedom 4P hub motion on mid-span flap bending moment



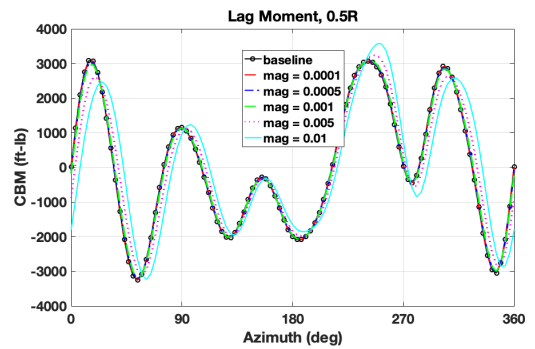
(a) x motion



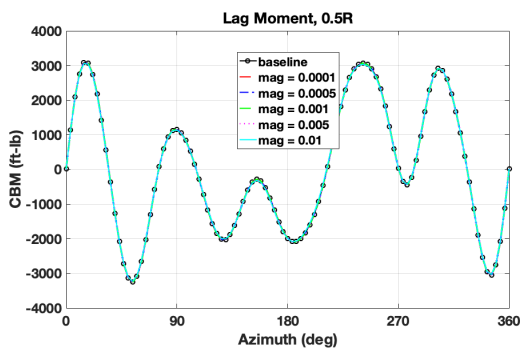
(b) θ_x motion



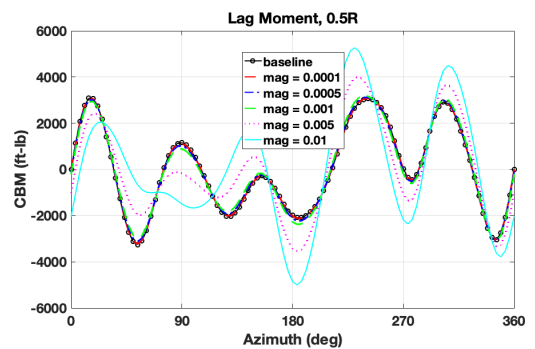
(c) y motion



(d) θ_y motion

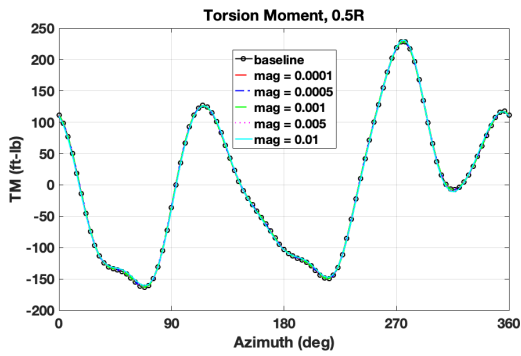


(e) z motion

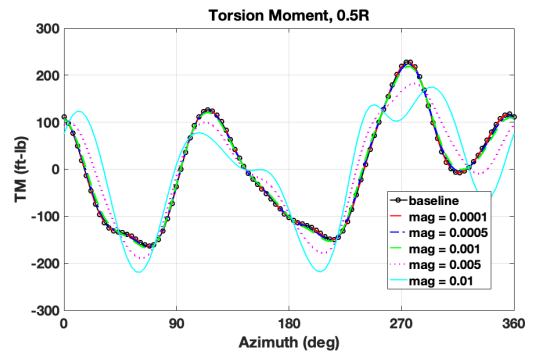


(f) θ_z motion

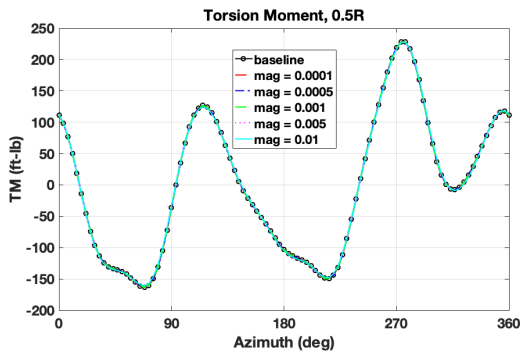
Figure 5.8: Effects of single degree of freedom 4P hub motion on mid-span chordwise bending moment



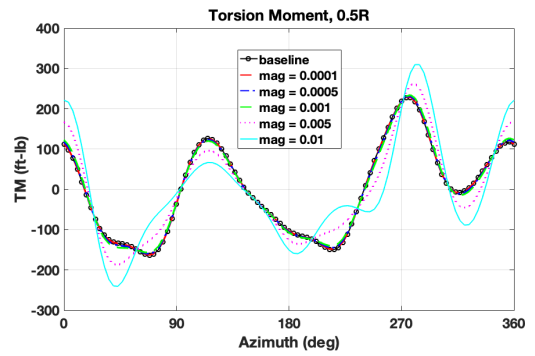
(a) x motion



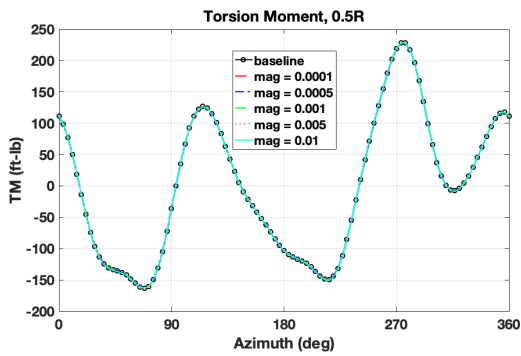
(b) θ_x motion



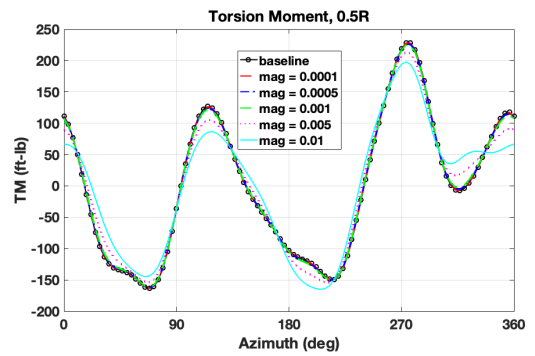
(c) y motion



(d) θ_y motion

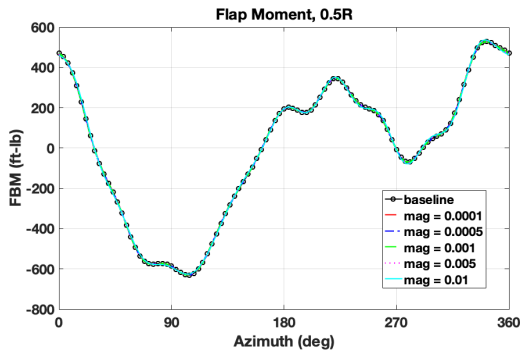


(e) z motion

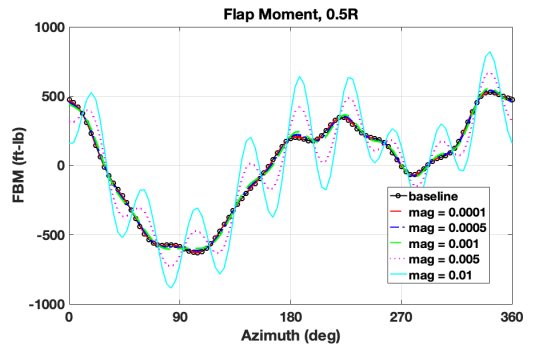


(f) θ_z motion

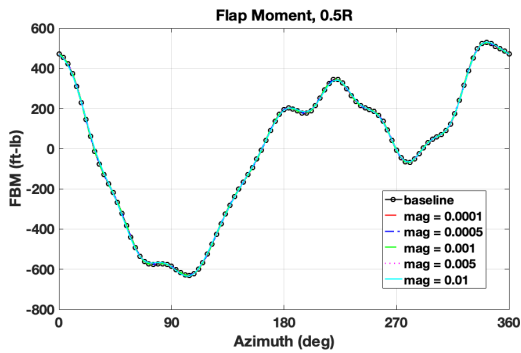
Figure 5.9: Effects of single degree of freedom 4P hub motion on mid-span torsion moment



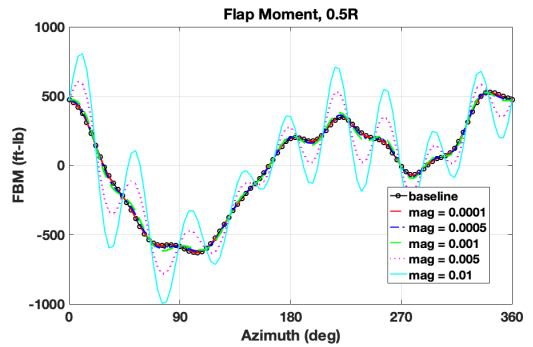
(a) x motion



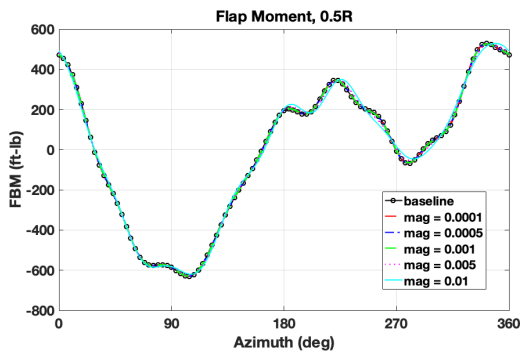
(b) θ_x motion



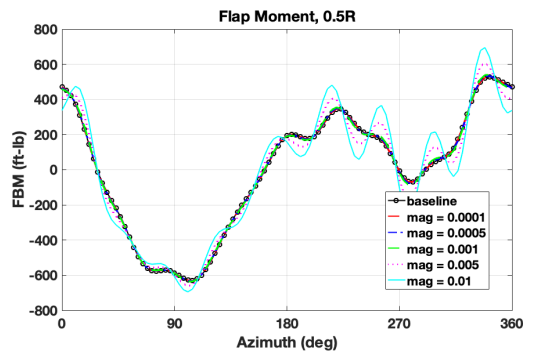
(c) y motion



(d) θ_y motion

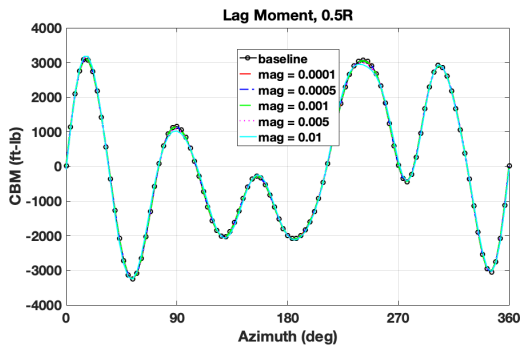


(e) z motion

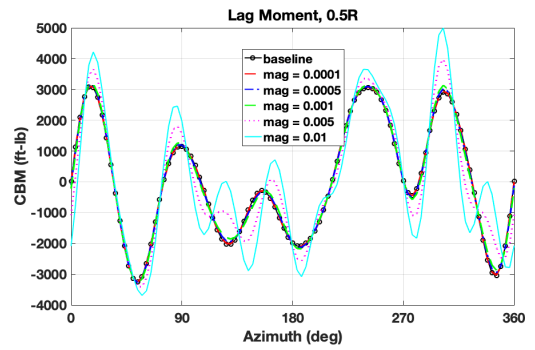


(f) θ_z motion

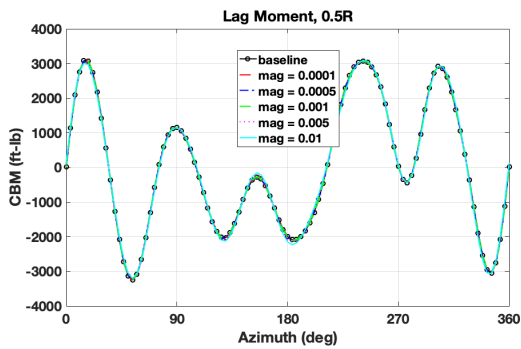
Figure 5.10: Effects of single degree of freedom 8P hub motion on mid-span flap bending moment



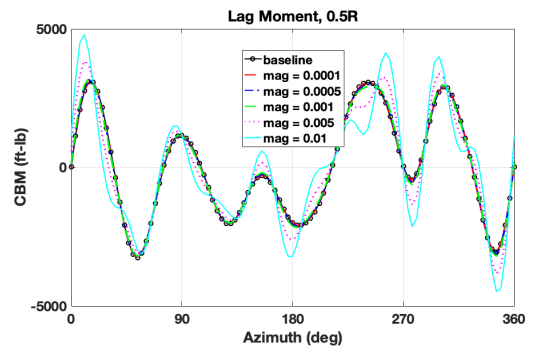
(a) x motion



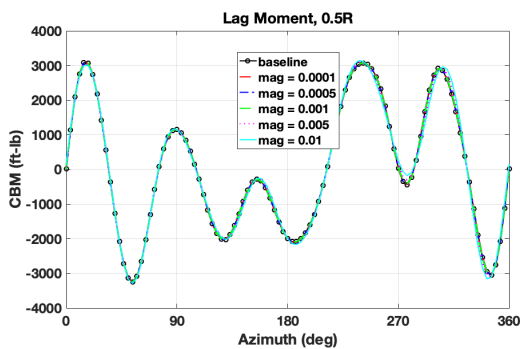
(b) θ_x motion



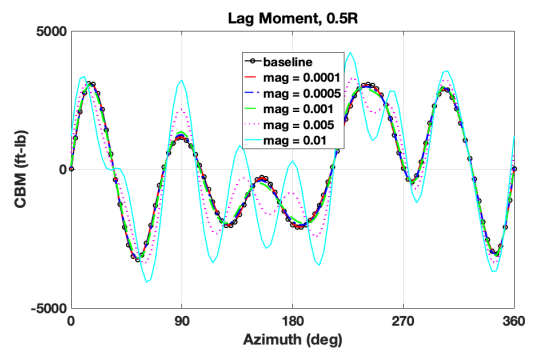
(c) y motion



(d) θ_y motion

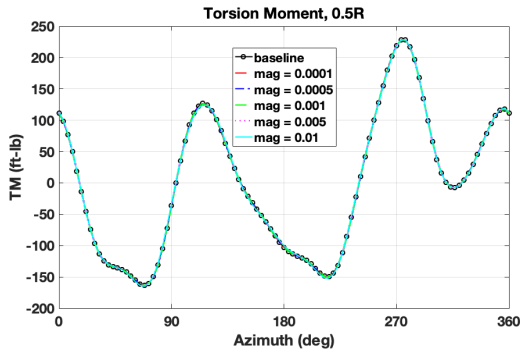


(e) z motion

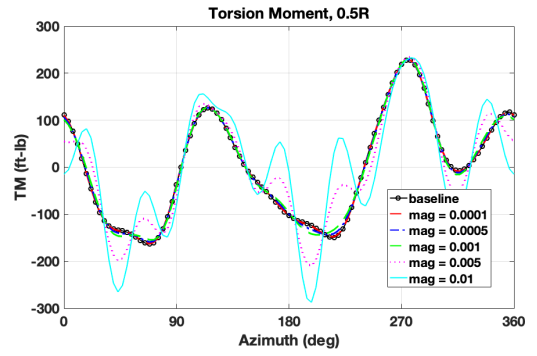


(f) θ_z motion

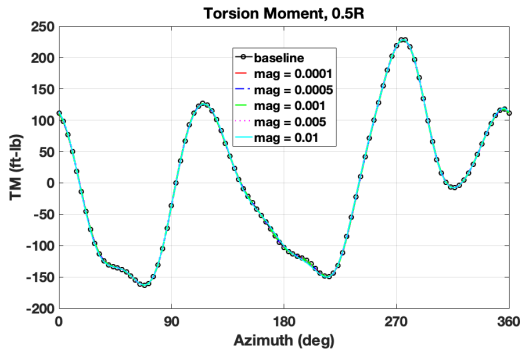
Figure 5.11: Effects of single degree of freedom 8P hub motion on mid-span chord-wise bending moment



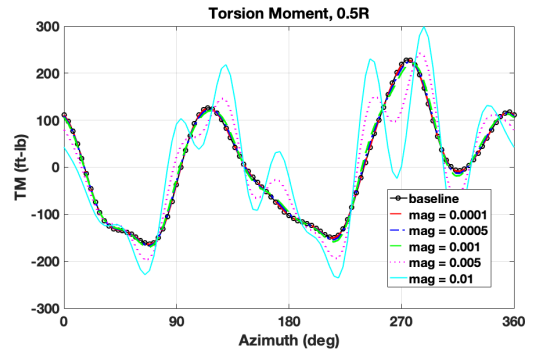
(a) x motion



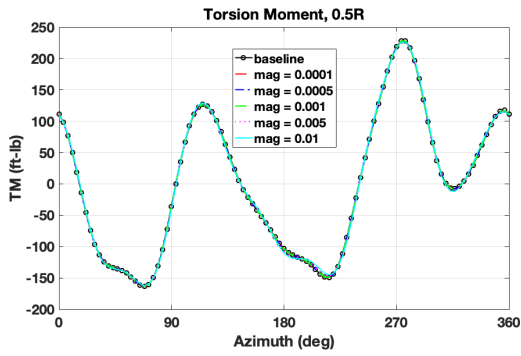
(b) θ_x motion



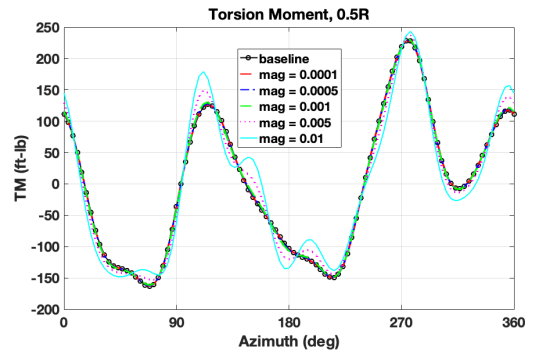
(c) y motion



(d) θ_y motion

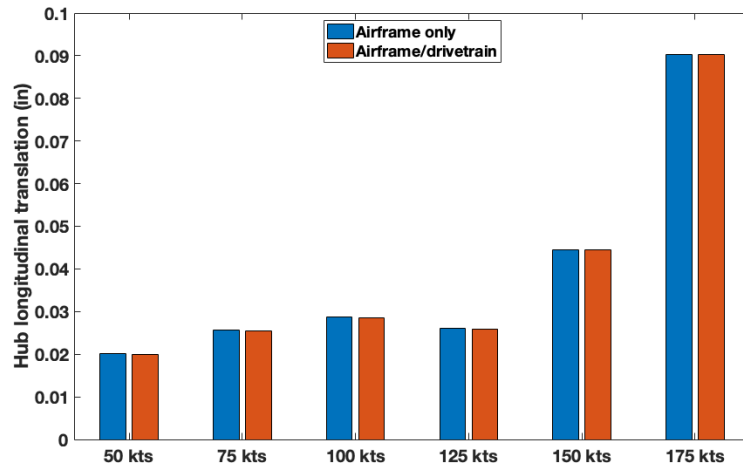


(e) z motion

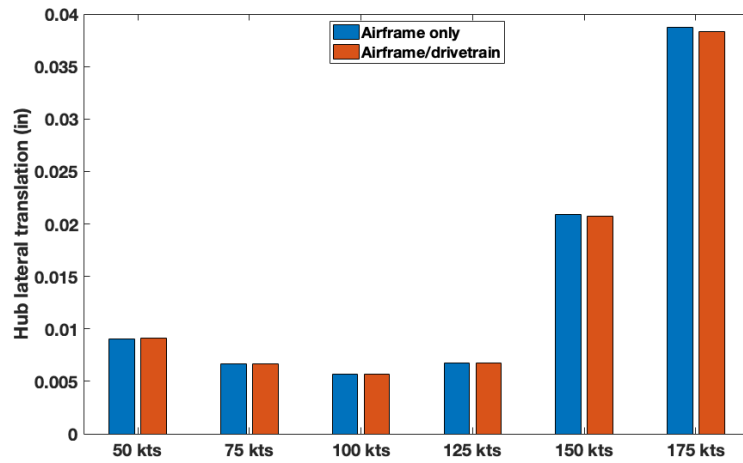


(f) θ_z motion

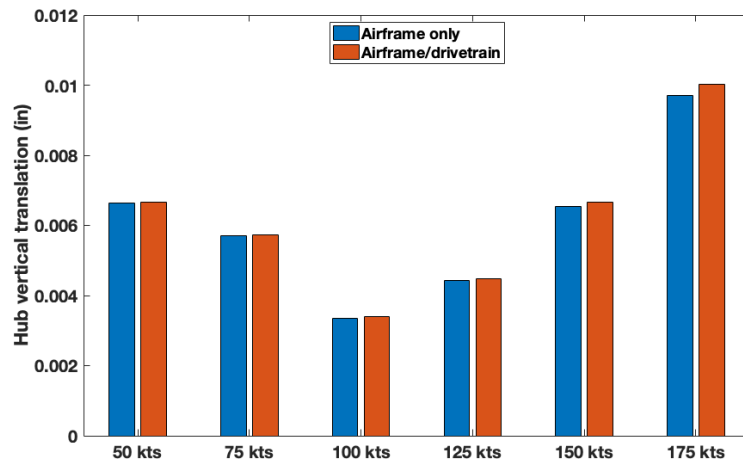
Figure 5.12: Effects of single degree of freedom 4P hub motion on mid-span torsion moment



(a) Longitudinal hub motion

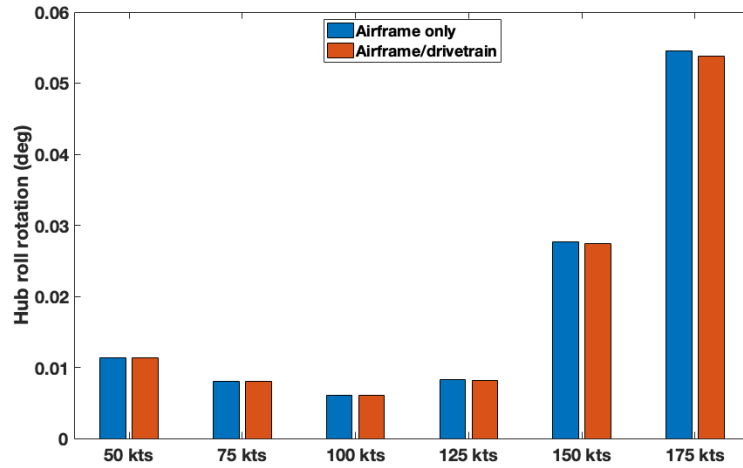


(b) Lateral hub motion

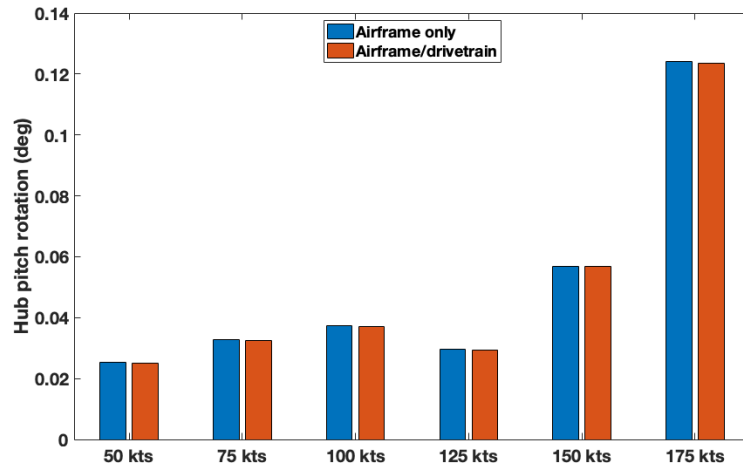


(c) Vertical hub motion

Figure 5.13: 1/2 Peak-to-peak hub translation resulting from coupling with airframe and drivetrain

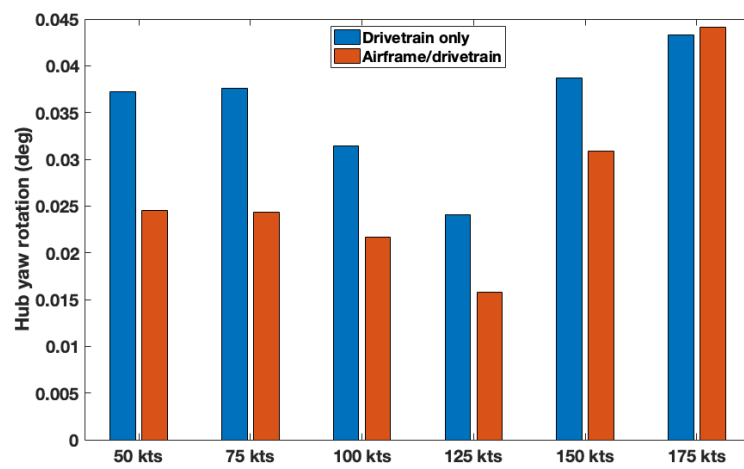


(a) Roll hub motion



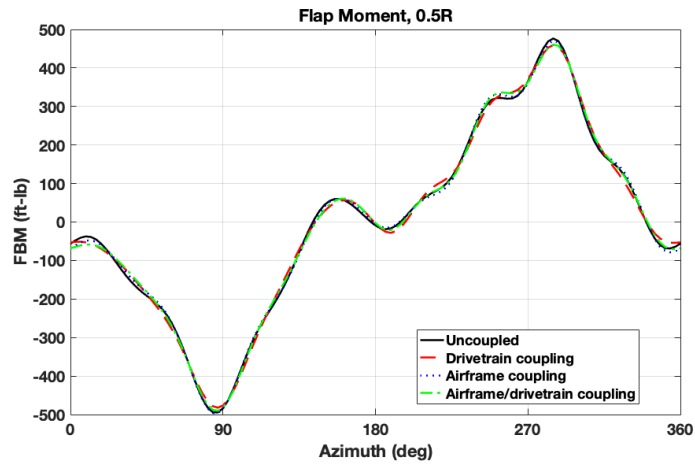
(b) Pitch hub motion

Figure 5.14: 1/2 Peak-to-peak hub roll and pitch rotation resulting from coupling with airframe and drivetrain

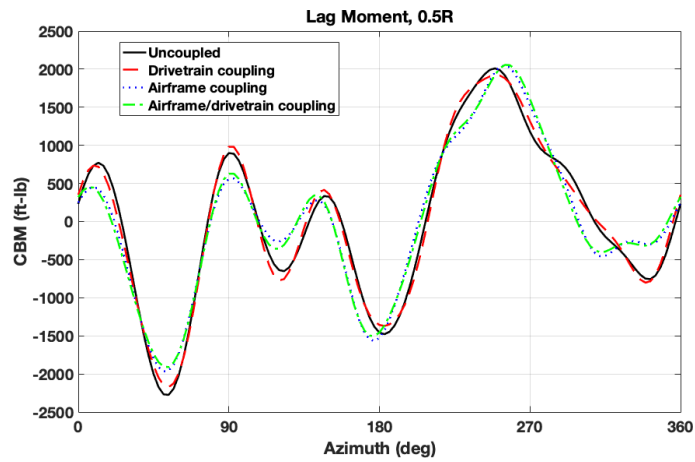


(a) Roll hub motion

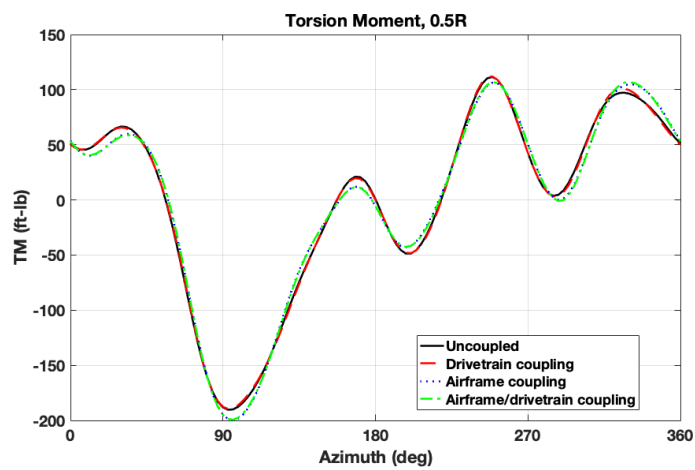
Figure 5.15: 1/2 Peak-to-peak hub yaw rotation resulting from coupling with airframe and drivetrain



(a) Flap bending moment

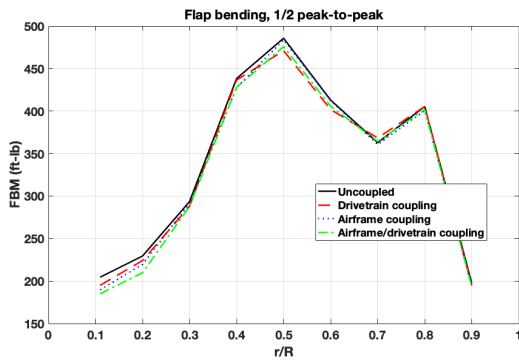


(b) Lag bending moment

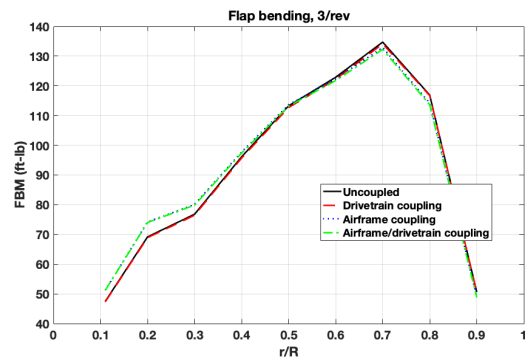


(c) Torsion moment

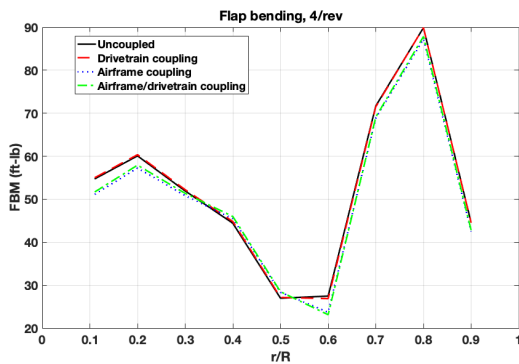
Figure 5.16: Effects of coupling on mid-span blade loads



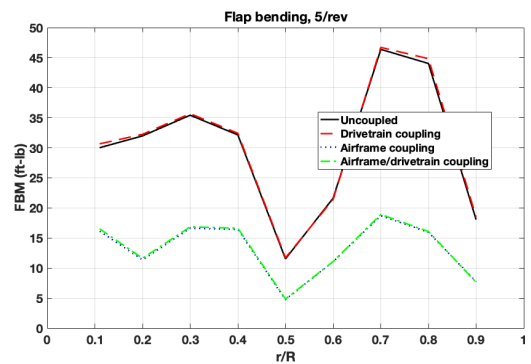
(a) 1/2 peak-to-peak



(b) 3/rev

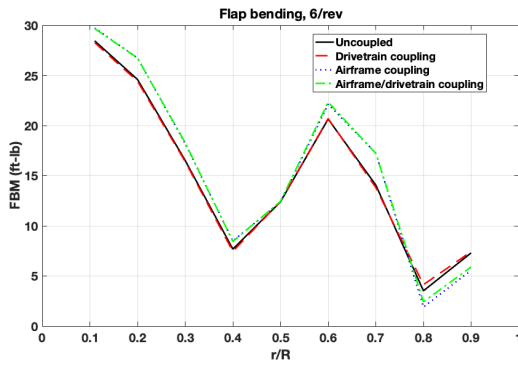


(c) 4/rev

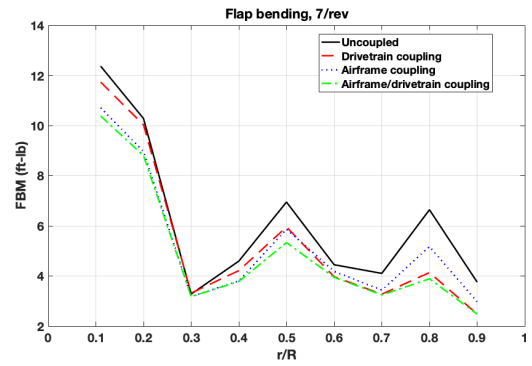


(d) 5/rev

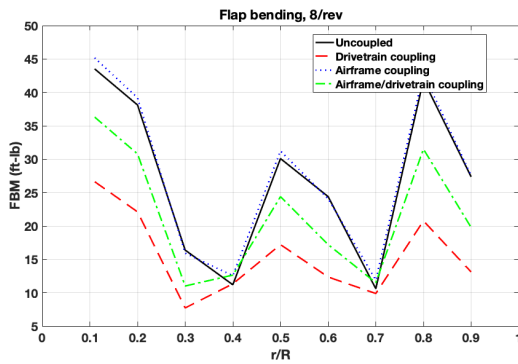
Figure 5.17: Effects of coupling on vibratory flap bending



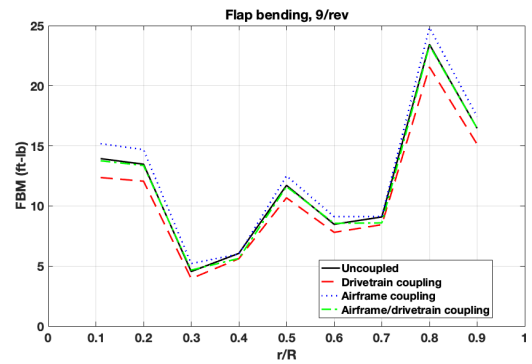
(a) 6/rev



(b) 7/rev

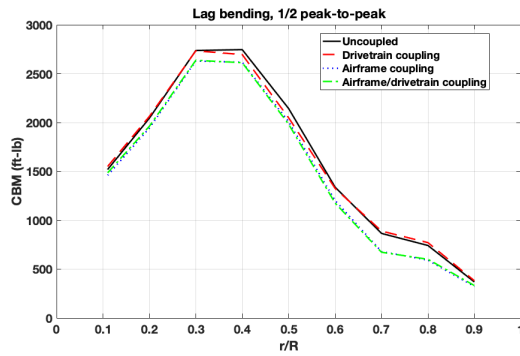


(c) 8/rev

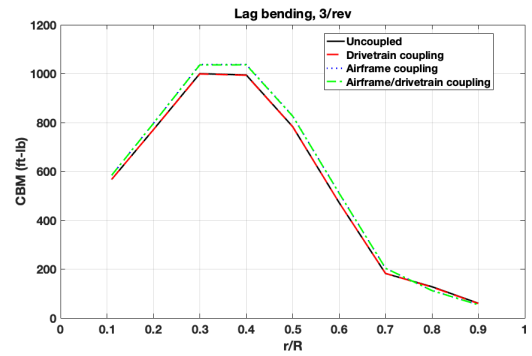


(d) 9/rev

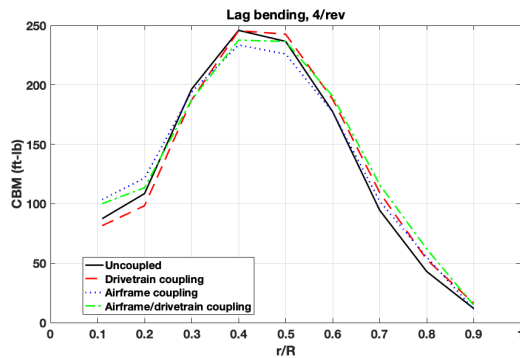
Figure 5.18: Effects of coupling on vibratory flap bending higher harmonics



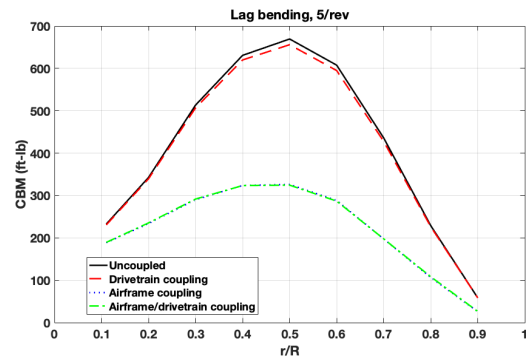
(a) 1/2 peak-to-peak



(b) 3/rev

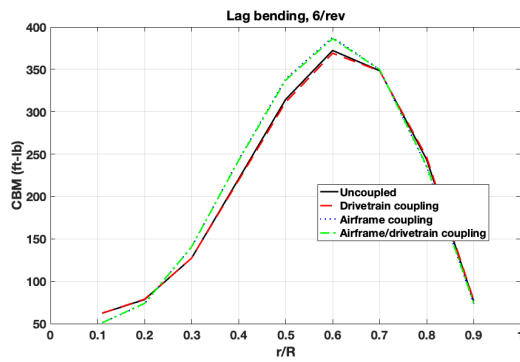


(c) 4/rev

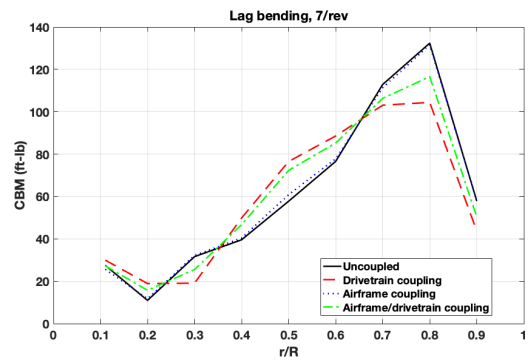


(d) 5/rev

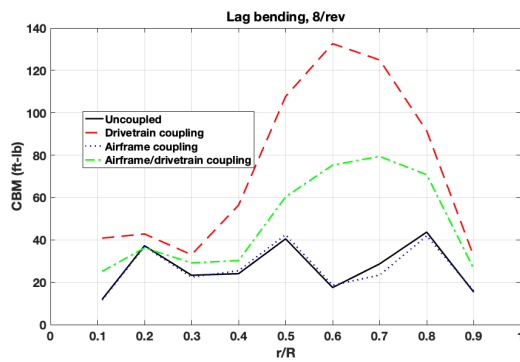
Figure 5.19: Effects of coupling on vibratory lag bending



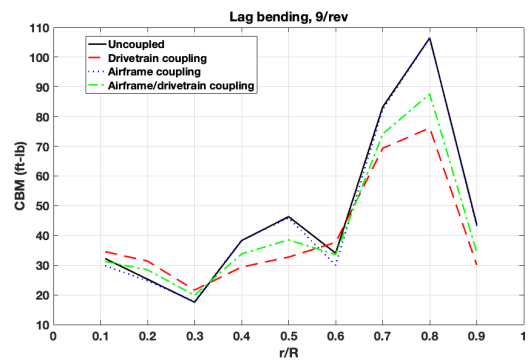
(a) 6/rev



(b) 7/rev

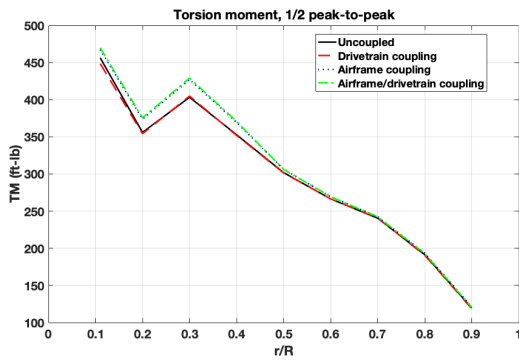


(c) 8/rev

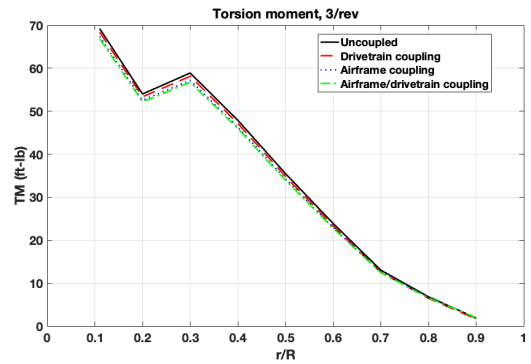


(d) 9/rev

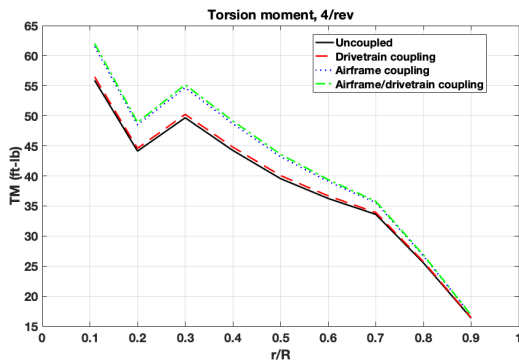
Figure 5.20: Effects of coupling on vibratory lag bending higher harmonics



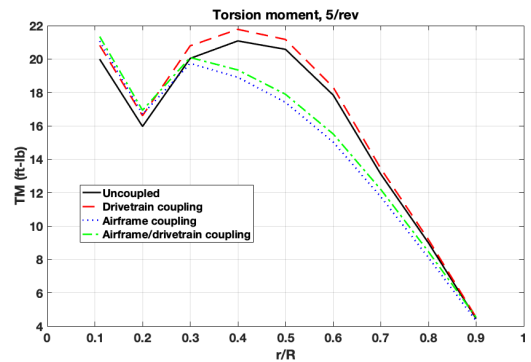
(a) 1/2 peak-to-peak



(b) 3/rev



(c) 4/rev



(d) 5/rev

Figure 5.21: Effects of coupling on vibratory torsion moment

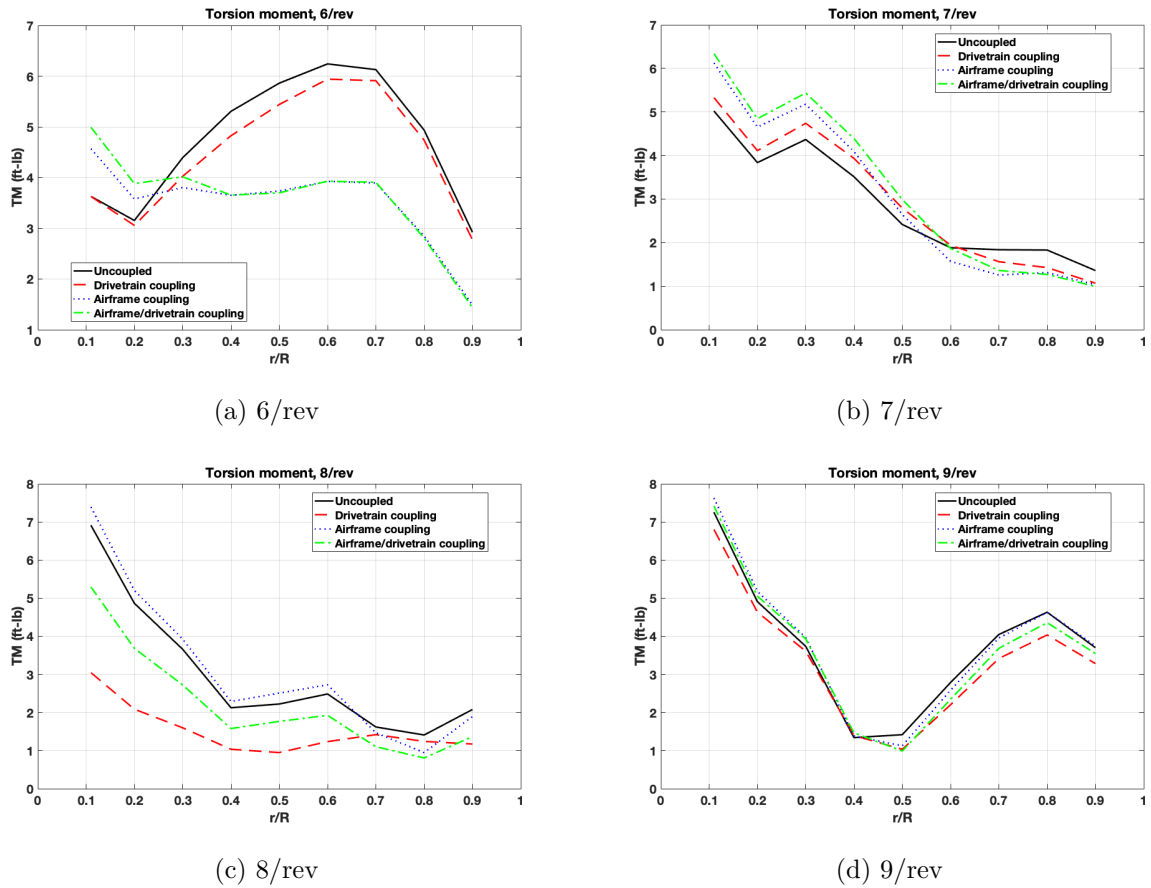
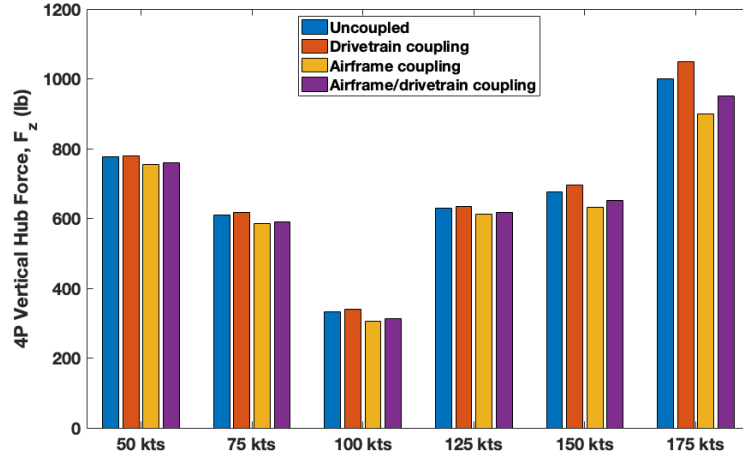
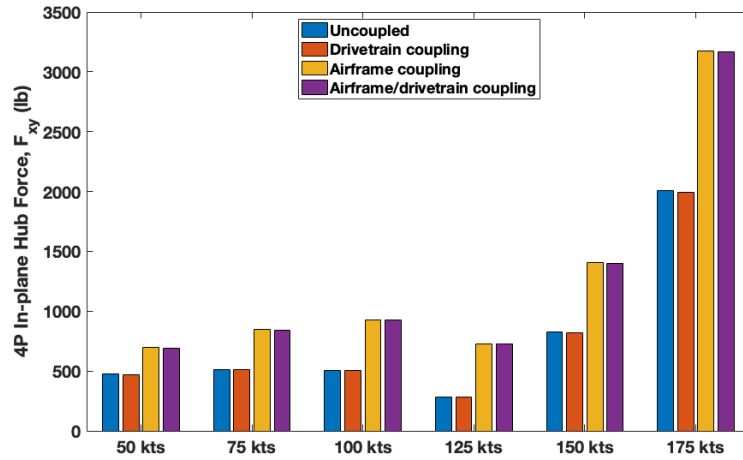


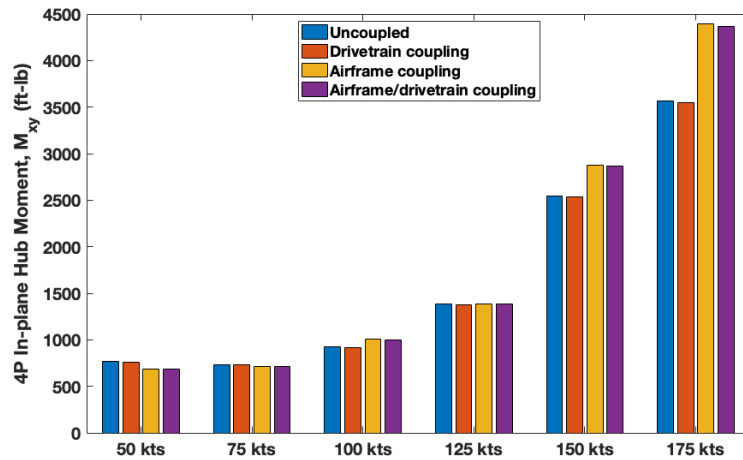
Figure 5.22: Effects of coupling on vibratory torsion moment higher harmonics



(a) Vertical hub force

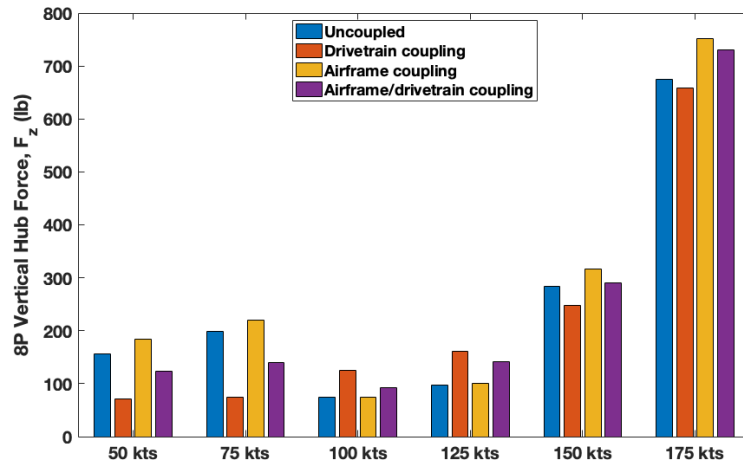


(b) In-plane hub force

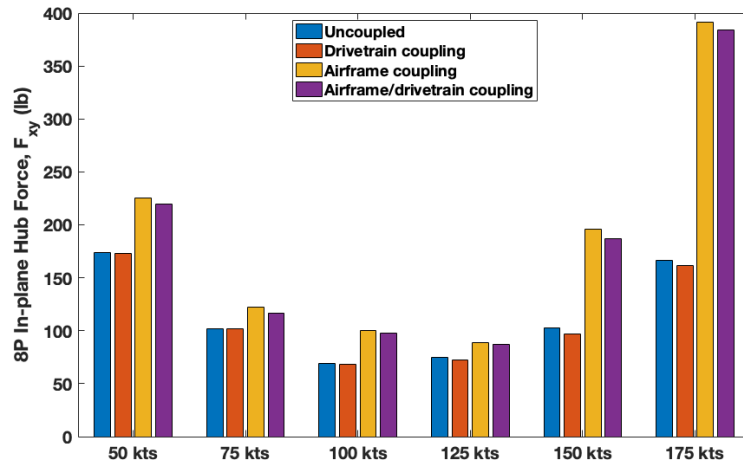


(c) In-plane hub moment

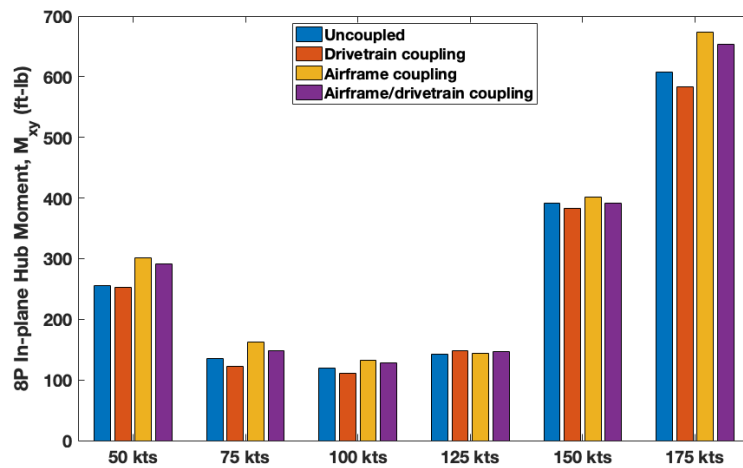
Figure 5.23: Effects of coupling on 4P hub loads



(a) Vertical hub force

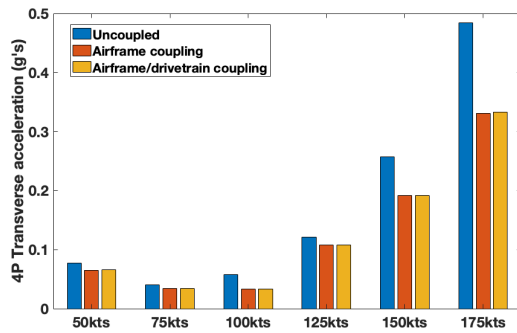


(b) In-plane hub force

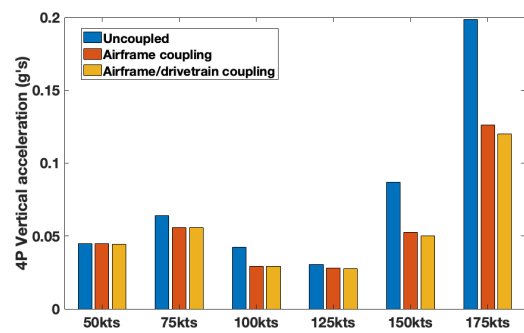


(c) In-plane hub moment

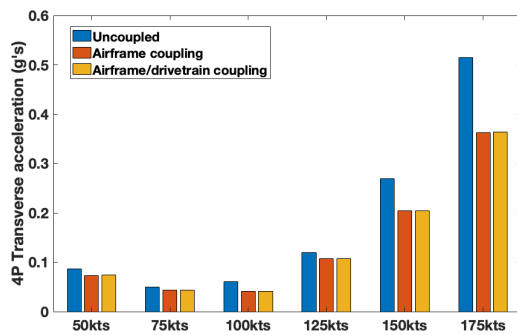
Figure 5.24: Effects of coupling on 8P hub loads



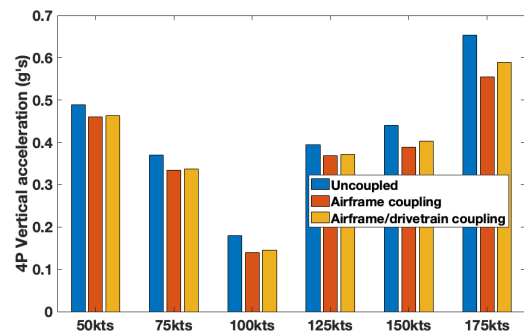
(a) Pilot transverse acceleration



(b) Pilot vertical acceleration

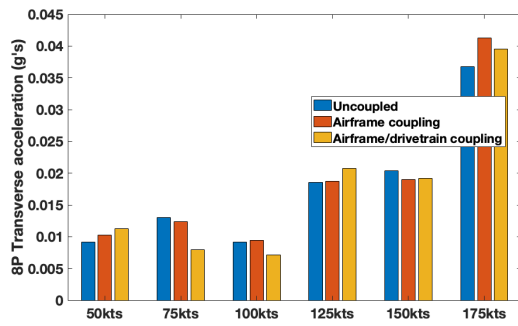


(c) Co-pilot transverse acceleration

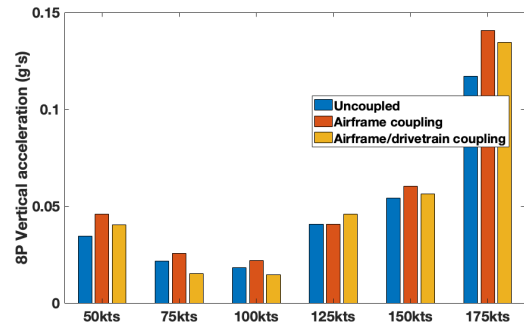


(d) Co-pilot vertical acceleration

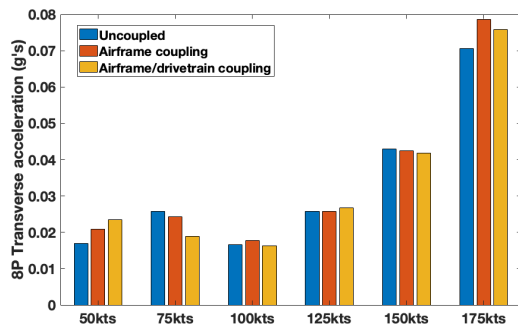
Figure 5.25: Effects of coupling on 4P pilot/co-pilot seat vibrations



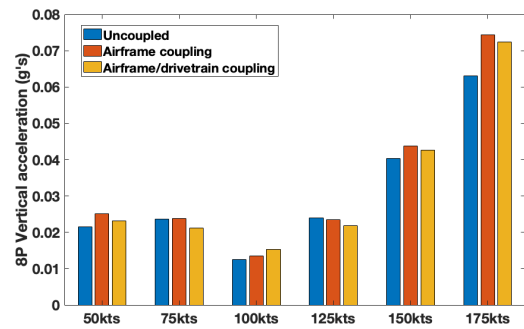
(a) Pilot transverse acceleration



(b) Pilot vertical acceleration

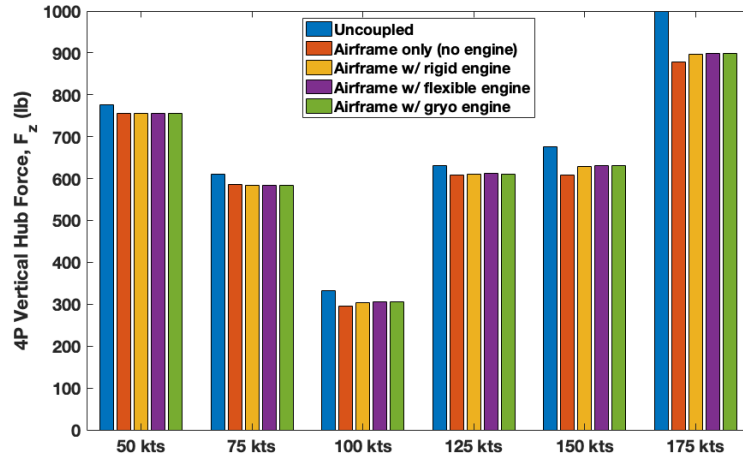


(c) Co-pilot transverse acceleration

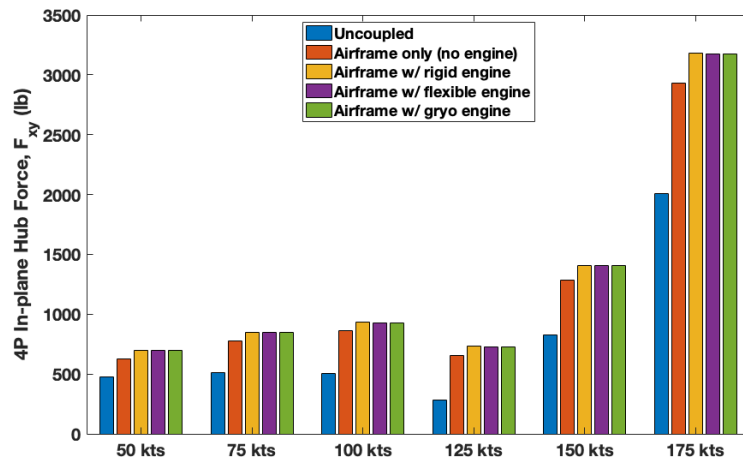


(d) Co-pilot vertical acceleration

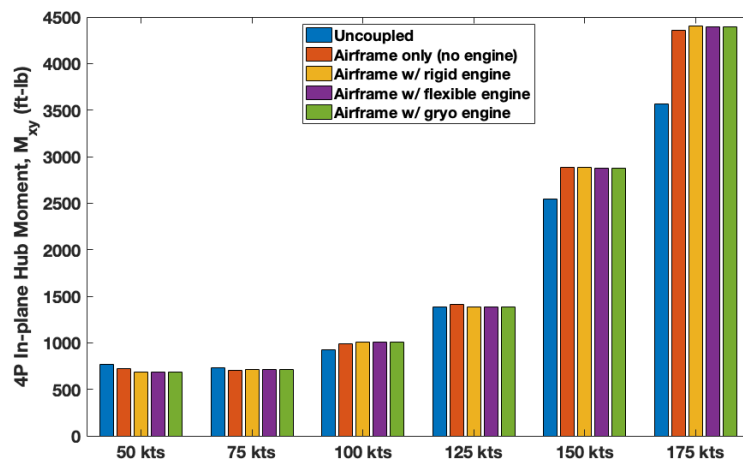
Figure 5.26: Effects of coupling on 8P pilot/co-pilot seat vibrations



(a) Vertical hub force

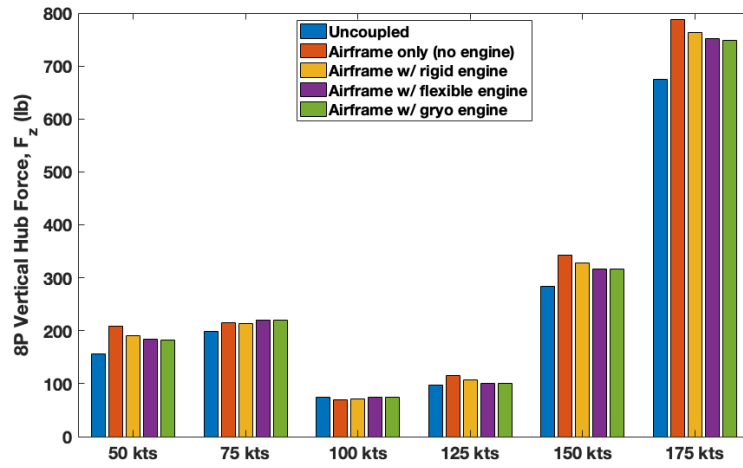


(b) In-plane hub force

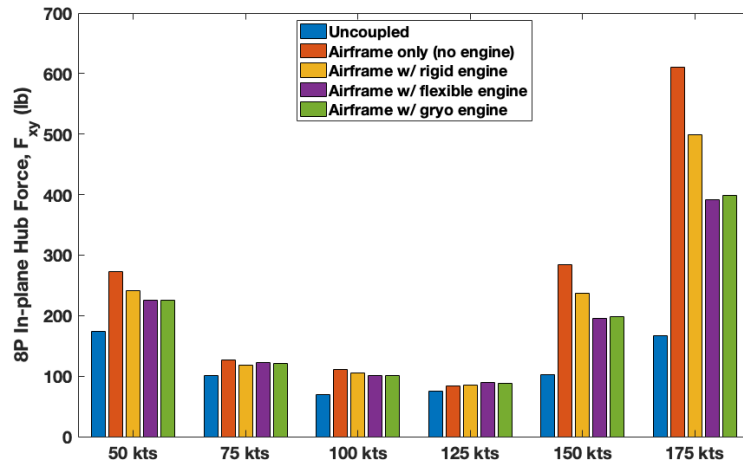


(c) In-plane hub moment

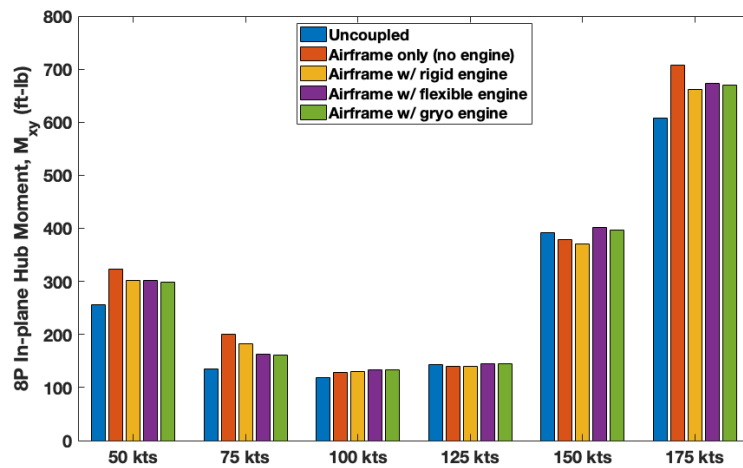
Figure 5.27: Effects of engine modeling on 4P hub loads



(a) Vertical hub force

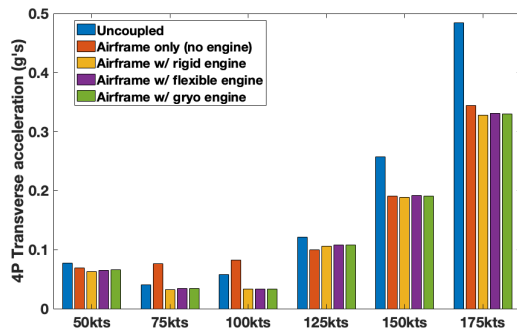


(b) In-plane hub force

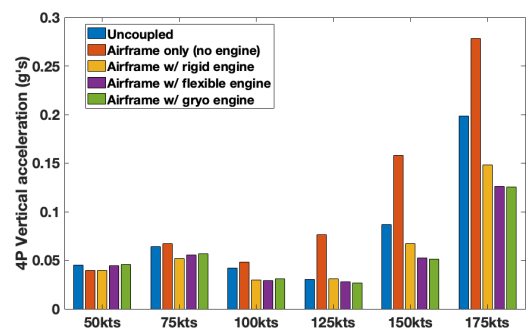


(c) In-plane hub moment

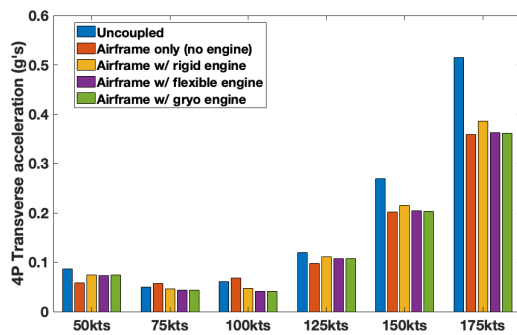
Figure 5.28: Effects of engine modeling on 8P hub loads



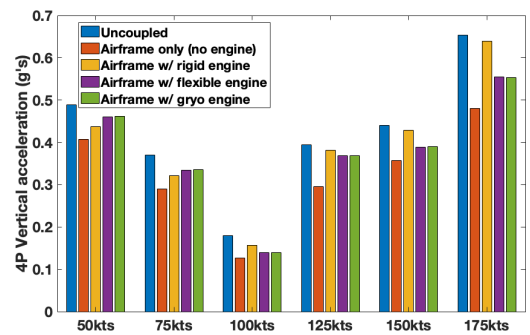
(a) Pilot transverse acceleration



(b) Pilot vertical acceleration

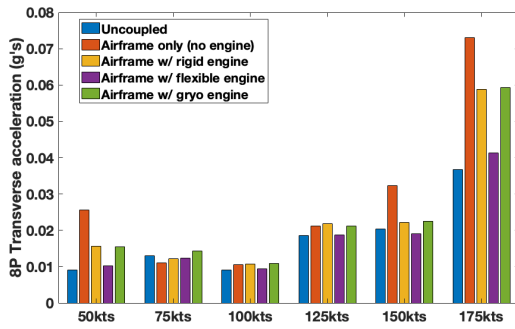


(c) Co-pilot transverse acceleration

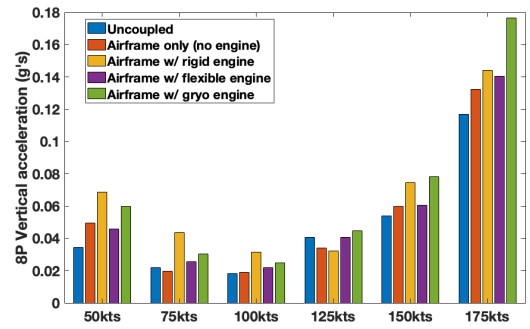


(d) Co-pilot vertical acceleration

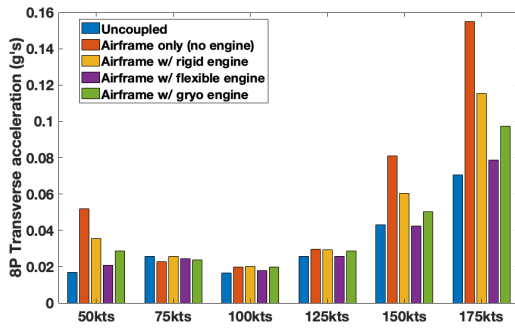
Figure 5.29: Effects of engine modeling on 4P pilot/co-pilot seat vibrations



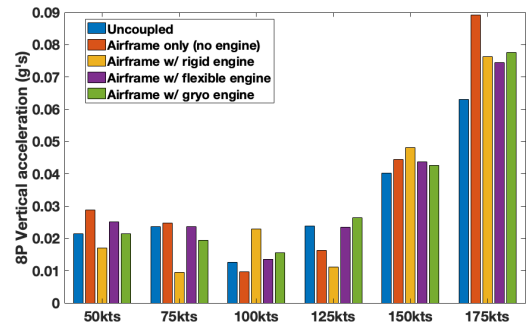
(a) Pilot transverse acceleration



(b) Pilot vertical acceleration

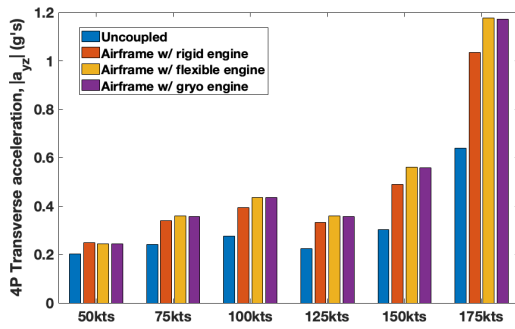


(c) Co-pilot transverse acceleration

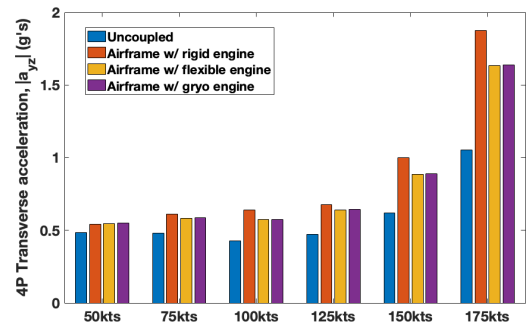


(d) Co-pilot vertical acceleration

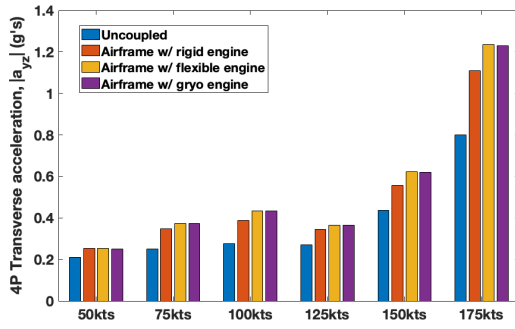
Figure 5.30: Effects of engine modeling on 8P pilot/co-pilot seat vibrations



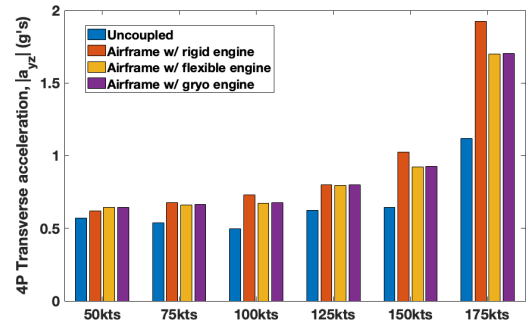
(a) Left fore engine mount



(b) Right fore engine mount

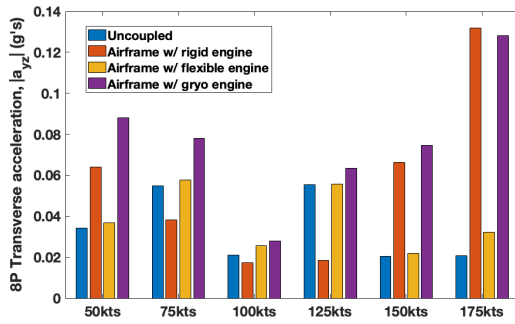


(c) Left aft engine mount

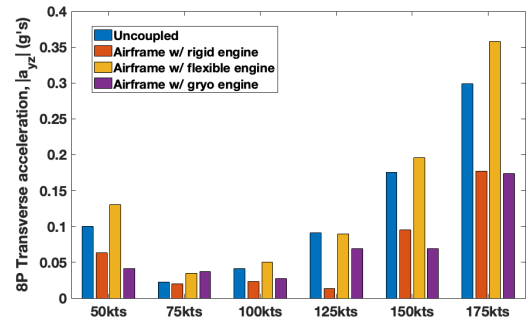


(d) Right aft engine mount

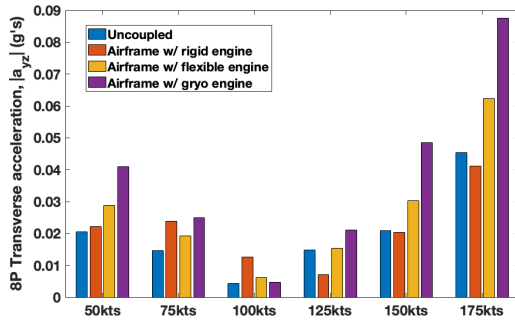
Figure 5.31: Effects of engine modeling on 4P engine vibrations



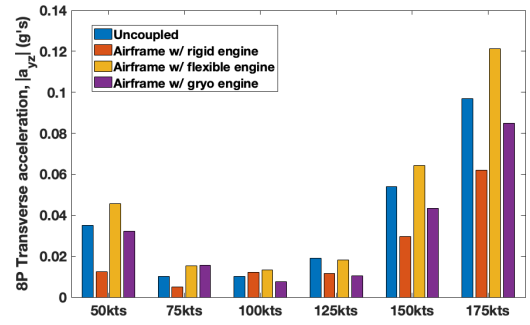
(a) Left fore engine mount



(b) Right fore engine mount



(c) Left aft engine mount



(d) Right aft engine mount

Figure 5.32: Effects of engine modeling on 8P engine vibrations

6 Summary and Conclusions

This chapter summarizes the primary results of this dissertation, identifies the key conclusions of the work and provides suggestions for future work in this area.

6.1 Summary

The work presented in this thesis consists of two main parts: the coupling between the finite element models of an engine and a helicopter airframe and the coupling of the aeromechanical model of a helicopter rotor to models representing a flexible drivetrain and airframe.

A fixed-frame frequency domain sub-structuring approach was developed to couple engine and airframe models in order to analyze vibration levels at engine supports of a helicopter. This methodology has several key advantages over conventional full finite element models:

1. Transfer functions can be generated from full finite element models without the necessity of modal approximation or truncation. The various types of damping (combination of complex stiffness, viscous damping and modal damping) can also be included in the analysis without any loss of accuracy.

2. Millions of finite element DOF can be reduced to only the set of interface nodes, external forcing nodes, and any additional nodes where one is interested in the response. Because only the small subset of nodes are involved in the solution, the solution process is computationally efficient and up to 1000 times faster than full finite element models.
3. The method may be extended to nonlinear interface stiffness and/or damping as well as experimentally acquired transfer functions for individual components.

The computational efficiency of the developed substructuring methodology allowed for parametric studies on the engine mount structures for a S-92 helicopter airframe coupled with the associated GE turboshaft engines. The conclusions from those studies are summarized in the following section.

Existing comprehensive analysis methodology was expanded to account for a flexible hub condition, allowing the rotor to be coupled to components in the fixed frame, namely a flexible airframe and drivetrain. This coupling leverages the previous frequency domain substructuring methodology, using frequency domain models of the fixed frame components and coupling them with the rotor analysis, and the impact of these couplings on the blade structural loads, fixed frame hubloads, and vibrations at the pilot seat and engines were examined. Further, the effects of the complexity of the engine modeling within the airframe were also examined. The primary conclusions of this work are detailed in the next section.

6.2 Key Conclusions

6.2.1 Engine-Airframe Coupling

1. The transverse 4P engine response is sensitive to changes in either or both inboard strut stiffness, but is unaffected by changes in the outboard struts. Conversely, the transverse 8P engine response is sensitive to changes in the outboard strut stiffness while being generally unaffected by changes in either or both pairs of inboard struts.
2. Doubling the stiffness of the torque tube reduced the 8P transverse response of the fore mount points of the engine by 50%, while having little effect on the aft mount point response or the 4P response at any mount point.
3. The 4P response at the aft mount of the right engine may be high if not specifically targeted for vibration reduction. If ignored, the vibration may increase by 100% or more of the baseline value.
4. In most cases, strut structural damping does not offer significant reduction in vibratory response at the engine mounts.
5. Changing the stiffness of the torque tube does not affect the 4P response and reduces the fore mount response for both engines by 20%.
6. The 8P response is most affected by asymmetry in the mount struts stiffness.
7. When the stiffness of the aft mount struts is varied, the 4P response of the left

engine fore mount increases when the response of the other three mounts decrease. This represents a fundamental compromise in overall engine vibration minimization.

8. Stiffening the torque tube and each of the aft mount struts to 200% of their baseline values results in significant reductions of 4P and 8P response at all engine mounts for most flight conditions considered. On average, the 4P response was reduced by 14% and the 8P response was reduced by 37%.
9. The high level of asymmetry present in the system as well as the lack of a consistent solution to minimize vibrations at each mount point simultaneously indicate that the problem of engine vibrations is likely best addressed through an active vibration control strategy.

6.2.2 Rotor-Drivetrain-Airframe-Engine Coupling

A baseline UH-60 rotor model was individually coupled with representative drivetrain and airframe models. The following trends were observed:

1. The addition of a flexible drivetrain has very little impact on the blade structural loads. When examining the vibratory components, the higher harmonics, particularly 8P, are the most affected, with the lag bending increased, while the flap bending and torsion are decreased. On the other hand, the airframe coupling are seen most noticeably in the 5P blade loads.
2. Despite small impacts on the blade loads, the fixed frame hub loads can be

significantly changed by the airframe and drivetrain coupling, which has implications for the prediction of vibrations throughout the airframe. The 4P in-plane forces and moments are significantly increased by the airframe coupling, but not by the drivetrain coupling. The 4P vertical force is decreased with airframe coupling, and increased with drivetrain coupling, while the opposite is true for all the 8P hub forces and moments. As a result, when compared to the uncoupled case, 4P vibrations computed at the pilot/co-pilot seats are lower for the coupled cases, while 8P vibrations are higher.

3. The presence of an engine mass within the airframe model is important in predicting the hub loads, particularly the in-plane forces. However, the complexity of the engine model does not have much influence. In particular, the 4P hub loads are largely unchanged by a rigid engine mass versus a flexible engine with or without gyroscopic effects. The 8P are generally decreased by a flexible versus rigid engine, and although this effect is small, it is significant for the 8P in-plane forces at higher vibration conditions. The engine gyroscopic forces have negligible influence on the hub loads.
4. The vertical 4P vibration at the pilot/co-pilot seat is significantly impacted by the engine flexibility, though asymmetrically. That is, the flexible engine results in a decrease of the predicted vibration at the pilot seat and an increase at the co-pilot seat. The 8P vibration prediction is generally decreased by the flexible engine and increased with the addition of gyroscopic effects.
5. The predicted 4P engine vibration is asymmetrically affected by the flexible

engine model in that vibrations on the left engine are increased while vibrations on the right are decreased by the flexible model when compared with the rigid model. The gyroscopic forces have negligible impact on the 4P engine vibrations. The 8P engine vibration predictions are significantly by both engine flexibility and gyroscopic forces. The flexible engine generally results in an increase in the predicted 8P vibration over the rigid engine Gyroscopic forces increase the predicted vibration on the left engine while decreasing them on the right.

6.3 Recommendations for Future Work

The research presented in this dissertation have illustrated the impact that coupling of rotor analysis with airframe and drivetrain models can have on the prediction of vibrations at the main rotor hub and throughout the airframe. However, much work is still required before analysis tools can be used reliably for vibration prediction during design. To that end, the overall effectiveness of the analysis in this work needs to be benchmarked against flight test data. This level of validation requires compatibility between the rotor, airframe, engine, and drivetrain models with respect to the actual components used in testing. It is also important to have access to a wide range of test data, including accurate measurements of blade loads, hub loads, and vibrations throughout the airframe, specifically at the pilot seat and on the engines. The ability of this type of validation to be conducted at the university level will require a very high level of cooperation with the industry and government

entities who produce the components and models and perform the flight tests.

In addition to further validating the analysis against available data, there are additions to the analysis that are likely to have great impact on the vibration predictions presented here. The first of these is the incorporation of CFD aerodynamics into the comprehensive analysis. The accuracy of aerodynamic loads and blade structural loads have been shown to be significantly improved by the use of CFD over free wake modeling. Previously, coupled CFD/CSD analysis has been done with the PRASADUM code used in this analysis, and access to high performance computing resources should make this type of analysis relatively simple to incorporate.

In addition, sources of vibratory loading on the airframe beyond the main rotor need to be accounted for. The first and simplest of these to account for is the tail rotor. As described in section 2.1, a dynamic inflow model was used to calculate the thrust and torque at the tail rotor, however, a structural model of the tail rotor blades should be incorporated to gain understanding of the vibratory loads that are produced at the tail rotor and their impact on vibrations throughout the airframe.

The interactional aerodynamics between the rotor and airframe can also be examined. Though the primary source of the 4P and 8P loading on the airframe come through the main rotor hub, the rotor wake impinges on the airframe, particularly at low speeds, thus provides another source of vibratory loading that has not been accounted for. Addressing the interactional aerodynamics can include incorporation of panel methods as well as full CFD modeling including the airframe.

Finally, a major component of this work was focused on reduction of engine

vibrations by tuning engine mount structural properties. For the purposes of this work, those properties were assumed to be linearly elastic. The analysis can easily be adapted to allow for non-linear properties, as those found in elastomers, allowing for the possibility of further reduction of engine vibrations.

Bibliography

- [1] Loewy, R. G., "Helicopter Vibrations: A Technological Perspective," *Journal of the American Helicopter Society*, Vol. 29, (4), October 1984, pp. 4–30.
- [2] Taylor, R. B. and Teare, P. A., "Helicopter Vibration Reduction With Pendulum Absorbers," *Journal of the American Helicopter Society*, Vol. 20, (3), July 1975, pp. 9–17.
- [3] Paul, W., "Development and Evaluation of the Main Rotor Bifilar Absorber," American Helicopter Society 25th Annual Forum, May 14–16, 1969.
- [4] Hammond, C., "Wind Tunnel Results Showing Rotor Vibratory Loads Reduction Using Higher Harmonic Blade Pitch," *Journal of the American Helicopter Society*, Vol. 28, (1), January 1983, pp. 10–15.
- [5] Ham, N., "Helicopter Individual-Blade-Control Research at MIT 1977–1985," *Vertica*, Vol. 11, (1/2), 1987, pp. 109–122.
- [6] Milgram, J., Chopra, I., and Straub, F., "Rotors with trailing edge flaps: Analysis and comparison with experimental data," *Journal of the American Helicopter Society*, Vol. 43, (4), 1998, pp. 319–332.
- [7] Rita, A. D., McGarvey, J. H., and Jones, R., "Helicopter Rotor Isolation Evaluation Utilizing the Dynamic Antiresonant Vibration Isolator," *Journal of the American Helicopter Society*, Vol. 23, (1), January 1978, pp. 22–29.
- [8] Reichert, G., "Helicopter Vibration Control - A Survey," *Vertica*, Vol. 5, (1), 1981, pp. 1–20.
- [9] Friedmann, P. P. and Millott, T. A., "Vibration reduction in rotorcraft using active control - A comparison of various approaches," *Journal of Guidance, Control, and Dynamics*, Vol. 18, (4), 1995, pp. 664–673.
- [10] Kessler, C., "Active Rotor Control for Helicopters: Individual Blade Control and Swashplateless Rotor Designs," *CEAS Aeronautical Journal*, Vol. 1, (1-4), 2011, pp. 23–54.

- [11] Kvaternik, R., Bartlett, F. D., and Cline, J. H., “A Summary of Recent NASA/Army Contributions to Rotorcraft Vibration and Structural Dynamics Technology,” Technical Report NASA CP-2495, February 1988.
- [12] Datta, A. and Johnson, W., “An Assessment of the State-of-the-art in Multidisciplinary Aeromechanical Analyses,” AHS Specialist’s Conference on Aeromechanics, 2008.
- [13] Ormiston, R. A., “Comparison of several methods for predicting loads on a hypothetical helicopter rotor,” *Journal of the American Helicopter Society*, Vol. 19, (4), 1974, pp. 2–13.
- [14] Hansford, R. E. and Vorvald, J., “Dynamics Workshop on Rotor Vibratory Loads Prediction,” *Journal of the American Helicopter Society*, Vol. 43, (1), 1998, pp. 76–87.
- [15] Kvaternik, R. G., “The NASA/Industry Design Analysis Methods for Vibrations (DAMVIBS) Program - A Government Overview,” Technical Report April, 1992.
- [16] Cronkhite, J. D., “The NASA/Industry Design Analysis Methods for Vibration (DAMVIBS) Program - Bell Helicopter Textron Accomplishments,” Technical report, Bell Helicopter Textron, 1992.
- [17] Gabel, R., Lang, P., and Reed, D., “The NASA/Industry Design Analysis Methods for Vibrations (DAMVIBS) Program - Boeing Helicopters Airframe Finite Element Modeling,” Technical Report 4, 1992.
- [18] Twomey, W. J., “The NASA/Industry Design Analysis Methods for Vibrations (DAMVIBS) Program - Sikorsky Aircraft - Advances toward interacting with the airframe design process,” *33rd Structures, Structural Dynamics and Materials Conference*, 1992.
- [19] Toossi, M., Weisenburger, R., and Hashemi-Kia, M., “The NASA/Industry Design Analysis Methods for Vibrations (DAMVIBS) Program - McDonnell Douglas Helicopter Company Achievements,” Technical report, McDonnell Douglas Helicopter Company.
- [20] Christ, R., Ferg, D., Kilroy, K., Toossi, M., and Weisenburger, R., “Plan, Formulate and Discuss a NASTRAN Finite Element Model of the AH-64A Helicopter Airframe,” Technical report, NASA CR-187446, 1990.
- [21] Dinyovszky, P. and Twomey, W. J., “Plan, Formulate and Discuss a NASTRAN Finite Element Model of the UH-60A Helicopter Airframe,” Technical Report NASA CR-181975, 1990.
- [22] Gabel, R., Lang, P. F., Smith, L., and Reed, D., “Plan, Formulate, Discuss and Correlate a NASTRAN Finite Element Vibrations Model of the Boeing Model 360 Helicopter Airframe,” Technical report, NASA CR-181787, 1989.

- [23] Dompka, R., Sciascia, M., Lindsay, D., and Chung, Y., “Plan, Formulate and Discuss a NASTRAN Finite Element Vibrations Model of the Bell ACAP Helicopter Airframe,” Technical report, NASA CR-181774, 1989.
- [24] Stebbins, R. and Twomey, W. J., “Plan, Formulate and Discuss a NASTRAN Finite Element Model of the Sikorsky ACAP Helicopter Airframe,” Technical Report NASA CR-182059, 1990.
- [25] Dompka, R., “Investigation of Difficult Component Effects on Finite Element Model Vibration Prediction for the Bell AH-1G Helicopter,” Technical Report NASA CR-181916, 1989.
- [26] Dompka, R., “Investigation of Difficult Component Effects on Finite Element Model Vibration Prediction ofr the Bell ACAP Helicopter,” Technical Report NASA CR-187493, 1991.
- [27] Gerstenberger, W. and Wood, E. R., “Analysis of Helicopter Aeroelastic Characteristics in High-Speed Flight,” *AIAA Journal*, Vol. 1, (10), 1963, pp. 2366–2381.
- [28] Staley, J. A. and Sciarra, J. J., “Coupled Rotor/Airframe Vibration Prediction Methods,” AHS/NASA-Ames Specialists’ Meeting on Rotorcraft Dynamics, 1971.
- [29] Hohenemser, K. H. and Yin, S. K., “The Role of Rotor Impedance in the Vibration Analysis of Rotorcraft,” *Vertica*, Vol. 3, 1979.
- [30] Hsu, T.-K. and Peters, D., “Coupled Rotor/Airframe Vibration Analysis by a Combined Harmonic-Balance, Impedance-Matching Method,” *Journal of the American Helicopter Society*, Vol. 27, (1), January 1982, pp. 25–34.
- [31] Gabel, R. and Sankewitsch, V., “Rotor-Fuselage Coupling by Impedance,” American Helicopter Society 42nd Annual Forum, June 2–5, 1986.
- [32] Kunz, D. L., “Effects of Rotor-Body Coupling in a Linear Rotorcraft Vibration Model,” American Helicopter Society 36th Annual Forum, May 1980.
- [33] Rutkowski, M. J., “The Vibration Characteristics of a Coupled Helicopter Rotor-Fuselage by a Finite Element Analysis,” Technical Report NASA TP-2118, 1983.
- [34] Stephens, W. B. and Peters, D. A., “Rotor-Body Coupling Revisited,” *Journal of the American Helicopter Society*, Vol. 32, (1), January 1987, pp. 68–72.
- [35] Warmbrodt, W. and Friedmann, P. P., “Formulation of Coupled Rotor/Fuselage Equations of Motion,” *Vertica*, Vol. 3, (3/4), 1979.
- [36] Bir, G. and Chopra, I., “Prediction of Blade Stresses Due to Gust Loading,” 11th European Rotorcraft Forum, 1985.

- [37] Fledel, S., Rand, O., and Chopra, I., “Coupled Rotor/Airframe Vibration Analysis,” Fifteenth European Rotorcraft Forum, 1989.
- [38] Juggins, P. T. W., “A Comprehensive Approach to Couple Rotor-Fuselage Dynamics,” Paper 48, 14th European Rotorcraft Forum, September 20–23, 1988.
- [39] Hansford, R. E., “Considerations in the Development of the Coupled Rotor Fuselage Model,” *Journal of the American Helicopter Society*, Vol. 39, (4), October 1994.
- [40] Vellaichamy, S. and Chopra, I., “Aeroelastic Response of Helicopters with Flexible Fuselage Modeling,” 33rd Structures, Structural Dynamics and Materials Conference, 1992.
- [41] Vellaichamy, S. and Chopra, I., “Effect of Modeling Techniques in the Coupled Rotor-Body Vibration Analysis,” Proceedings of the 34th Structures, Structural Dynamics and Materials Conference and Adaptive Structures Forum, 1993.
- [42] Chiu, T. and Friedmann, P., “A Coupled Helicopter Rotor/Fuselage Aeroelastic Response Model for ACSR,” Proceedings of the 36th Structures, Structural Dynamics and Materials Conference and Adaptive Structures Forum, 1995.
- [43] Yeo, H. and Chopra, I., “Modeling Issues Related to Vibration Prediction of a Coupled Rotor/Fuselage System,” 38th Structures, Structural Dynamics and Materials Conference and Adaptive Structures Forum, 1997.
- [44] Yeo, H. and Chopra, I., “Effects of Modeling Refinements on Coupled Rotor/Fuselage Vibration Analysis,” American Helicopter Society 54th Annual Forum, May 1998.
- [45] Yeo, H., *A Comprehensive Vibration Analysis of a Coupled Rotor/Fuselage System*, Ph.D. thesis, University of Maryland, 1999.
- [46] Yeo, H. and Chopra, I., “Coupled Rotor/Fuselage Vibration Analysis for Teetering Rotor and Test Data Comparison,” *Journal of Aircraft*, Vol. 38, (1), 2001.
- [47] Yeo, H. and Chopra, I., “Coupled Rotor/Fuselage Vibration Analysis Using Detailed 3-D Airframe Models,” *Mathematical and Computer Modelling*, Vol. 33, (10-11), 2001, pp. 1035–1054.
- [48] Yang, M., Chopra, I., and Haas, D., “Vibration Prediction for Rotor System with Faults Using Coupled Rotor-Fuselage Model,” *Journal of Aircraft*, Vol. 41, (2), 2004, pp. 348–358.
- [49] Yang, M., Chopra, I., and Haas, D. J., “Sensitivity of Rotor-Fault-Induced Vibrations to Operational and Design Parameters,” *Journal of the American Helicopter Society*, Vol. 49, (3), 2004, pp. 328.

- [50] Yeo, H. and Potsdam, M., “Rotor Structural Loads Analysis Using Coupled Computational Fluid Dynamics / Computational Structural Dynamics,” American Helicopter Society 70th Annual Forum, May 2014.
- [51] Yeo, H., “UH-60A Rotor Structural Loads Analysis with Fixed-System Structural Dynamics Modeling,” American Helicopter Society 74th Annual Forum, May 14–17, 2018.
- [52] Min, B. Y., Smith, M. J., Worth, F., Wong, J., and Wake, B. E., “Toward Improved UA-60A Blade Structural Loads Correlation,” American Helicopter Society 74th Annual Forum, May 14–17, 2018.
- [53] Balke, R. W., “A Review of Turbine Engine Vibration Criteria for VTOL Aircraft,” Symposium on Environmental Effects on VTOL Designs, 1970.
- [54] Twomey, W. J. and Ham, E. H., “Review of Engine/Airframe/Drive Train Dynamic Interface Development Problems,” Technical report, USARTL-TR-78-13, 1978.
- [55] Hanson, H., Balke, R. W., Edwards, B. D., Riley, W. W., and Downs, B. D., “Engine/Airframe/Drive Train Dynamic Interface Documentation,” Technical report, USARTL-TR-78-15, 1978.
- [56] Needham, J. F. and Banerjee, D., “Engine/Airframe/Drive Train Dynamic Interface Documentation,” Technical Report USARTL-TR-78-12, 1978.
- [57] Bowes, M. A., “Engine/Airframe/Drive Train Dynamic Interface Documentation,” Technical Report USARTL-TR-78-14, 1978.
- [58] Cho, H., Ryu, H., Shin, S. J., Cho, I. J., and Jang, J. S., “Development of a coupled analysis regarding the rotor/dynamic components of a rotorcraft,” *Journal of Mechanical Science and Technology*, Vol. 28, (12), 2014, pp. 4841–4856.
- [59] de Klerk, D., Rixen, D. J., and Voormeeren, S. N., “General Framework for Dynamic Substructuring: History, Review and Classification of Techniques,” *AIAA Journal*, Vol. 46, (5), 2008, pp. 1169–1181.
- [60] Craig, R. R. and Kurdila, A., *Fundamentals of Structural Dynamics*, John Wiley & Sons, Hoboken, NJ, second edition, 2006.
- [61] Hurty, W. C., “Vibrations of Structural Systems by Component Mode Synthesis,” *Journal of the Engineering Mechanics Division*, Vol. 86, (4), 1960, pp. 51–70.
- [62] Hurty, W. C., “Dynamic Analysis of Structural Systems Using Component Modes,” *AIAA Journal*, Vol. 3, (4), 1965, pp. 678–685.

- [63] Craig, R. and Bampton, M., “Coupling of Substructure for Dynamic Analyses,” *AIAA Journal*, Vol. 6, (7), 1968, pp. 1313–1319.
- [64] Goldman, R. L., “Vibration Analysis by Dynamic Partitioning,” Vol. 7, (6), 1969, pp. 1152–1154.
- [65] Hou, S. N., “Review of Modal Synthesis Techniques and a New Approach,” Technical Report Bellcomm TM-69-2031-5, 1969.
- [66] Benfield, W. A. and Hrudá, R. F., “Vibration Analysis of Structures by Component Mode Substitution,” *AIAA Journal*, Vol. 9, (7), 1971, pp. 1255–1261.
- [67] Guyan, R., “Reduction of Stiffness and Mass Matrices,” *AIAA Journal*, Vol. 3, (2), 1965, pp. 380.
- [68] MacNeal, R. H., “A Hybrid Method of Component Mode Synthesis,” *Journal of Computers & Structures*, Vol. 1, (4), 1971, pp. 581–601.
- [69] Rubin, S., “Improved Component-Mode Representation for Structural Dynamic Analysis,” *AIAA Journal*, Vol. 13, (8), 1975.
- [70] Craig, R. R. and Chang, C. J., “Free-interface methods of substructure coupling for dynamic analysis,” *AIAA Journal*, Vol. 14, (11), 1976, pp. 1633–1635.
- [71] Chang, C.-J., *A General Procedure for Substructure Coupling in Dynamic Analysis*, Ph.D. thesis, University of Texas, 1977.
- [72] Jetmundsen, B., Bielawa, R. L., and Flannelly, W. G., “Generalized Frequency Domain Substructure Synthesis,” *Journal of the American Helicopter Society*, 1988, pp. 55–64.
- [73] Jetmundsen, B., *On Frequency Domain Methodologies for Prescribed Structural Modification and Subsystem Synthesis*, Ph.D. thesis, Rensselaer Polytechnic Institute, 1986.
- [74] Gordis, J., Bielawa, R., and Flannelly, W., “A General Theory for Frequency Domain Structural Synthesis,” *Journal of Sound and Vibration*, Vol. 150, 1991, pp. 139–158.
- [75] Ren, Y. and Beards, C. F., “On Substructure Synthesis with FRF Data,” *Journal of Sound and Vibration*, Vol. 185, (5), 1995, pp. 845–866.
- [76] de Klerk, D., Rixen, D. J., and de Jong, J., “The frequency based substructuring (FBS) method reformulated according to the dual domain decomposition method,” Proceedings of the XXIV International Modal Analysis Conference, 2006.
- [77] Department of Defense, “Environmental Engineering Considerations and Laboratory Tests,” Technical Report Test Method Standard MIL-STD-810F, 2000.

- [78] Johnson, W., *Rotorcraft Aeromechanics*, Cambridge University Press, New York, NY, 2013.
- [79] Sridharan, A., *Simulation Modeling of Flight Dynamics, Control and Trajectory Optimization of Rotorcraft Towing Submerged Loads*, Ph.D. thesis, University of Maryland, 2014.
- [80] He, C. and Peters, D. A., “Comparison of Measured Induced Velocities with Results from a Closed-Form Finite State Wake Model in Forward Flight,” American Helicopter Society 45th Annual Forum, May 1989.
- [81] Bhagwat, M. and Leishman, J., “Rotor Aerodynamics During Maneuvering Flight Using a Time-Accurate Free-Vortex Wake,” *Journal of the American Helicopter Society*, Vol. 48, (3), July 2003, pp. 143–158.
- [82] Howlett, J. J., “UH-60A Black Hawk Engineering Simulation Program: Volume I - Mathematical Model,” Technical Report NASA CR-166309, December 1981.
- [83] Pitt, D. and Peters, D., “Rotor Dynamic Inflow Derivatives and Time Constants from Various Inflow Models,” 9th European Rotorcraft Forum, 1983.
- [84] Bailey, F., “A Simplified Theoretical Method of Determining the Characteristics of a Lifting Rotor in Forward Flight,” Technical Report NACA 716, 1941.
- [85] Davis, S. J., “Predesign Study for a Modern 4-Bladed Rotor for the RSRA,” Technical Report NASA-CR-166155, 1981.
- [86] Friswell, M. I., Penny, J. E. T., Garvey, D., Seamus, and Lees, A. W., *Dynamics of Rotating Machines*, Cambridge University Press, 2010.
- [87] MSC Software Corporation, “MSC Nastran 2013 Superelements User’s Guide,” Technical report, 2013.
- [88] Bousman, W. G., Kufeld, R. M., Balough, D., Cross, J., Studebaker, K., and Jennison, C., “Flight Testing the UH-60A Airloads Aircraft,” American Helicopter Society 50th Annual Forum Proceedings, 1994.